

An Invertible Open-Loop Nonlinear Dynamic Temperature Dependent MR Damper Model

Sajit Satish Jumani

Thesis submitted to the faculty of the Virginia Polytechnic Institute and State University in
partial fulfillment of the requirements for the degree of

Master of Science
In
Mechanical Engineering

Steve Southward Chair

Mehdi Ahmadian
Saied Taheri

April 30, 2010
Blacksburg, VA

Keywords: Magnetorheological Damper, Skyhook, Open Loop Control, Inverse MR Damper
Model, Separable

Copyright 2010 Sajit Satish Jumani

An Invertible Open-Loop Nonlinear Dynamic Temperature Dependent MR Damper Model

Sajit Satish Jumani

Abstract

A Magnetorheological damper is a commonly used component in semi-active suspensions that achieves a high force capacity and better performance than a passive system, without the added expense and power draw of a fully active system, all while maintaining failsafe performance. To fully exploit the capabilities of an MR Damper, a high fidelity controller is required that is simple and easy to implement, yet does not compromise the accuracy or precision needed in many high-performance applications. There is a growing need for this level of operation, and this proposed work addresses these requirements by creating an empirically derived invertible model that enables the development of more accurate command signals by capturing the effect of temperature on a MR Damper's performance capabilities. Furthermore, this solution is specifically tailored for real-time application and does not require force feedback. Thus it requires low computation power and minimizes end-user cost by eliminating the need for additional high cost sensors such as load cells. A notable observation that resulted from the development of this proposed model was the difference in behavior between on and off states. Additionally a unique behavior was recognized with respect to the transition between high speed and low speed damping. For validation, the proposed model was compared against experimental data as well as an industry standard Spencer model; it produced excellent results in both cases with minimal error.

Acknowledgements

I would like to thank my advisor Dr. Steve Southward for his direction, support, and patience throughout this research process as well as his overall academic guidance and wisdom throughout graduate school.

I would also like to thank my committee members Dr. Ahmadian and Dr. Taheri for their help and support throughout the past two years in my research and academics.

Lastly, I would like to thank NASA and Virginia Tech for giving me the opportunity pursue my graduate degree with all of the necessary facilities and support that I could have ever asked for.

Table of Contents

Abstract.....	ii
Acknowledgements.....	iii
Table of Contents.....	iv
List of Figures	v
1) Introduction.....	1
2) Literature Review	2
2.1) Overview.....	2
2.2) Analysis	3
3) Modeling objectives	5
3.1) Overview	5
3.2) Reader’s Model	6
3.3) Proposed Temperature Dependent Model	8
4) Experimental Testing.....	9
5) Characterization of the Separable Model	10
5.1) Data Extraction.....	10
5.2) Backbone ID	12
5.3) Velocity Dependent Component: $g(v_{rel})$	16
5.4) Temperature Correction Function: $h(i,T)$	21
5.5) Current Dependent Function: $f(i)$	28
5.6) Complete Separable Function.....	29
6) Characterization of the Hysteresis Model.....	31
6.1) Process Structure	31
6.2) Adaptation Process	32
7) Forward Model Validation.....	38
8) Inversion of the Forward Model.....	41
8.1) Generation of the Inverse Hysteresis Model: HystIIR Universal – 1	44
9) Verification Study through Simulation	46
9.1) Validation Overview.....	46
9.2) MagneRide Verification	46
9.3) Spencer Validation	51
10) Conclusion.....	59
References	61

List of Figures

Figure 3.1. The $f(i)$ function represents the current dependent behavior of the MR Damper. It has an offset at zero current and deviates from linearity near the saturation limit	6
Figure 3.2. The $g(vrel)$ function captures the velocity dependent nonlinearity of the MR Damper; it is sigmoidal in nature.....	7
Figure 3.3. Visualization of Reader's inverse model	8
Figure 4.1. Experimental setup on Roehrig EMA	9
Figure 5.1. Experimental Force vs. Time response measured at 2A and 151 ^o F	11
Figure 5.2. Experimental Velocity vs. Time response measured at 2A and 151 ^o F.....	11
Figure 5.3. Experimental Force vs. Velocity measured at 2A and 151 ^o F.....	12
Figure 5.4. Dynamic Experimental Data and Estimated Backbone Data measured at 2A and 151 ^o F	14
Figure 5.5. Backbone force curves for all temperatures at 0, 1, 2, and 3 Amps.....	15
Figure 5.6. Close up of backbone force curves for 2 Amps	16
Figure 5.7. Collapsed backbone force curves for each respective current.....	17
Figure 5.8. Averaged collapsed backbone force curves that are independent of temperature.....	18
Figure 5.9. Normalized $gvrel$ at all four currents; they are independent of temperature	19
Figure 5.10. Four $gvrel$'s: one per current, as well as one universal $gvrel$	20
Figure 5.11. Standard deviation across "on" state $gvrel$ and "all" state $gvrel$	21
Figure 5.12. Progression of $h(T)$ across all temperatures and currents	22
Figure 5.13. 3-D surface plot of the progression of $h(T)$	23
Figure 5.14. Average $h(i, T)$ across "on" state only	24
Figure 5.15. Standard deviation for average $h(i, T)$ across "on" state	25
Figure 5.16. validation $h(i, T)$ for all temperatures and all currents	26
Figure 5.17. RMSE for $h(i, T)$ validation backbone curves.....	27
Figure 5.18. RMSE of $h(i, T)$ validation curves as a percentage of total damper force	28
Figure 5.19. Current Dependent Function $f(i)$ is a scale factor with units of Newtons	29
Figure 5.20. Estimated backbone force error in Newtons and as a percentage of total force.....	30
Figure 6.1. Block diagram of the gradient-descent adaptation process which was used to estimate the coefficients of the FIR filter.....	32
Figure 6.2. Convergence of the adaptive process to a final FIR filter for all 40 test files	34
Figure 6.3. Frequency response for all forty FRF's grouped with their respective current.....	35
Figure 6.4. Frequency response of all forty Frequency Response Functions of the FIR filters ...	36
Figure 6.5. Frequency Response Functions of three universal filters: FIR, IIR, LPF	37
Figure 7.1. Forward Model: nonlinear backbone model elements multiplied on the left are fed through the universal hysteretic filter to generate a complete MR damper force.....	38
Figure 7.2. RMSE of universal IIR filter vs. the unique FIR filters	39
Figure 7.3. Error as a percentage of total force: universal IIR model vs. unique FIR model.....	40
Figure 8.1. Example suspension control system employing an Inverse MR Damper model	41

Figure 8.2. Inverse MR Damper model cascaded with forward model	42
Figure 8.3. Inverse $f(i)$	43
Figure 8.4. Forward, Inverse, and Combined hysteresis filter frequency responses	45
Figure 9.1. Simulation study for verifying the MagneRide inverse MR damper model	46
Figure 9.2. Force versus time signals for $FMR1$ and $FMR2$	47
Figure 9.3. Force versus velocity for $FMR1$ and $FMR2$	47
Figure 9.4. Inverse mirror image validation error for 3A 132 ^o F.....	48
Figure 9.5. RMSE for inverse model cascaded with forward model validation simulation.....	49
Figure 9.6. Current tracking for 2 Amps at 141 degrees F	50
Figure 9.7. Tracking the current generated by the inverse model for all forty files	51
Figure 9.8. Simulink Illustration of Spencer Model	53
Figure 9.9. Force vs. Time for Spencer and Proposed Model	54
Figure 9.10. Error vs. time between Spencer force and model force.....	55
Figure 9.11. Error between the Spencer and proposed model as a percentage of total force	56
Figure 9.12. Force vs. Velocity characterization of damper in Spencer model: Spencer vs. proposed model force.....	57
Figure 9.13. MSE and Convergence of FIR filter in Proposed model for Spencer validation	58
Figure 9.14. FIR and IIR filter approximation for Spencer validation	58

1) **Introduction**

Semi-active (SA) suspension systems provide excellent vibration control for many applications in the automotive, aviation, and civil industries without the potentially decreased reliability and added expense of a fully active system. Magneto-Rheological (MR) dampers are a specific class of semi-active suspension components that use an electric current to generate a magnetic field surrounding the piston of a damper which in turn changes the local viscosity of the magnetic fluid in the shock, altering the damping characteristics. MR Dampers also have the additional benefits of very low power consumption while maintaining the ability to generate large forces, minimal complexity, and the inherent ability to function as a passive damper during a failure mode (complete loss of power).

In the racing industry and other high performance applications there is a growing need for an improved method of real-time MR Damper implementation that achieves more accurate force generation. A solution that meets this need can be used for either semi-active suspension control or model reference control. A vital component to this solution is a quantitative relationship that accurately captures the influence of temperature on the MR Damper's performance. To generate accurate control forces requires the development of a Nonlinear Dynamic Inverse Model (NLDIM) that outputs appropriate command signals to the MR Damper to enhance system performance [1, 2]. At the core of this NLDIM is an invertible high fidelity model that linearizes the highly nonlinear behavior of the MR Damper. Additionally, the solution required for linearization enables the ability to make an MR Damper behave like a reference passive damper.

The majority of previously developed damper models only captured behavior at a nominal operating temperature. The work presented in this document details the development of a new model that captures the MR Damper performance over a broad range of temperatures. This improved temperature dependent model enables a more accurate command signal to be calculated and sent to the MR Damper. Unique to this model is the development of "universal" parameters that are not dependent on system states such as current or temperature. This attribute gives these parameters the ability to be applied to a broad range of operating states, hence the name "universal".

The goal of the research presented in this document was to develop an empirical high fidelity temperature dependent model for a MR Damper that could be inverted and implemented in real-time without requiring any additional high-cost sensors than what is currently used for a traditional Skyhook control implementation. Furthermore, this model should directly compensate for the effect of temperature on the model component that is responsible for capturing the hysteretic behavior of the MR Damper. This goal explicitly defines the design criteria for the NLDIM and will be used as a barometer for all future discussion, development and analysis of potential controller designs. A review of the existing control strategies and

damper models are presented in the following section. It is shown that no single approach meets all of these design criteria.

2) **Literature Review**

2.1) **Overview**

There has been extensive effort put forth to model the highly nonlinear behavior of an MR Damper. Characteristic of several passive and non-passive dampers, many MR Dampers exhibit a bilinear behavior characteristic of high speed and low speed damping. However, it also has the additional nonlinearity associated with the semi-active nature originating from a control current input [1, 3]. The level of complexity involved in modeling this behavior can easily grow to large proportions. For example, a model of even the most basic passive damper can be made to include highly nonlinear equations spanning 23 parameters, 10 of which are tunable as they correspond to the shock valving, and require advanced solvers to converge upon a solution that is sensitive to step size and initial conditions [4]. The addition of the current-based nonlinearity in a MR Damper further complicates matters. Breese and Gordaninejad illustrate this fact with a lengthy parametric force equation based on a Bingham plastic model [5]. This model requires that a portion of its coefficients be determined by a 3-D FEA of the specific MR Damper used for the experiment. These coefficients are then fed into a differential energy balance equation that uses a 4th order Runge-Kutta solver. Although it does accurately model the temperature increase of an MR Damper over time and matches the experimental data well, it is a complicated and involved process which is not suitable for real-time implementation.

There are several models that describe the highly nonlinear behavior of Magnetorheological dampers and can be separated into two general categories, parametric and non-parametric. Parametric models are physics based models with parameters that have real physical meaning and carry engineering units. The parametric models include but are not limited to the Bouc-Wen model [6], Spencer model [7], thermo-mechanical models [5, 8-11], nonlinear Bingham plastic models [5, 10-13], modified Bingham models [2], nonlinear bi-viscous damper models with and without hysteresis [12, 14, 15], linear force generator models [16], lumped parameter models [17], models derived from thermodynamic energy balance and heat transfer equations [18, 19], nonlinear black-box models [20], LuGre and Dahl models [21], and nonlinear visco-elastic models [12]. The non-parametric models are mostly empirically derived and include, but again, are not limited to, Artificial Neural Networks (ANN) [22-24], a pruned inverse ANN of the Spencer model [25], linearized models [26], fuzzy logic models [17, 22, 27], and the non-parametric developments of Song [28, 29].

There are also various control strategies to take advantage of the controllable damping capabilities of an MR Damper. Examples include Nero Fuzzy Logic[17], adaptive semi-active control with and without an observer (Kalman filter) [28, 30], Skyhook control [31], no-jerk

Skyhook [32], temperature corrected Skyhook[33], Skyhook/groundhook hybrids[27], on/off, optimal control and clipped optimal control [34], and PID control using force feedback [14, 15]. This list gives a sampling of the many control strategies available today. The next section analyzes their capabilities and shows that none of them meet all of the design requirements set forth at the beginning of this section.

2.2) **Analysis**

All of the models and control strategies listed above are good and work well for their intended applications. However, for our specific design problem, the approaches listed above did not meet all of the design criteria. Many designs left room for improvement in the error between the actual force produced by an MR Damper and the desired force it was thought to have produced by the controller. A decrease in this force tracking error enhances the ability of any control system to satisfy performance goals for the end user, such as better vibration control of a sprung mass or greater ability to exploit a tire's contact patch.

The most common characteristic that prevented many damper models from meeting our design criteria was their highly nonlinear set of governing equations. In order to generate damper forces which closely match a given input command force using an open-loop approach, the MR Damper model must be invertible, and therefore the equations governing a damper's behavior need to be simple. Jalili also speaks to the necessity of a simple controller design by stating "For practical implementation, however, it is preferable to simplify these strategies thus leading to simpler software implementations" [34]. Although existing models listed in Section 2.1 can capture the nonlinear behavior of an MR Damper quite well, they cannot be easily manipulated to determine what current is required in order to produce a desired force output. This manipulation is necessary to create an inverted model that is integral to developing an improved MR Damper controller, especially the NLDIM. The defining attributes of these previously developed models, namely their complex nonlinearity, requirement for advanced numerical solvers, and high computational cost eliminates models such as the Bouc-Wen[6], Spencer[7, 20, 26, 35], thermo-mechanical[5, 8-11, 18, 19], and Bingham based variants [2, 5, 10-13] from our list of potential candidates.

An area where the proposed NLDIM can enhance current control strategies is the ability to eliminate additional sensors [1, 3, 25]. There are many robust control strategies that require force feedback or other feedback sensors to monitor additional states [2, 14, 15, 21-23]; however, this does come at a price. If one wanted to implement force feedback, a shock load cell manufactured by Penske can cost about \$1200 plus the cost of wiring and a Beru F1 in-line amplifier. This significantly increases hardware cost for the end user, thus justifying the desire to exclude additional sensors in the design criteria. Another area where the NLDIM can improve many control systems is through its use of a nonlinear inverse model. This nonlinear inverse model replaces the commonly assumed linear relationship between the command signal and the

force produced by the MR Damper. The necessity for a nonlinear relationship between the command signal and the actual damper force produced has been shown by Reader to maintain if not improve the existing levels of damper performance [1, 3]. Details of how to develop this improved correlation is reviewed in later sections.

Another area where current models did not meet the desired design requirements was the absence of real-time temperature correction within a high fidelity model. Extensive research has shown a correlation between damper performance and operating temperature. Batterbee and Simms reported that an increase in temperature results in a reduction in yield force and thus yield stress, a reduction in the slope of post yield stress correlating to a reduction in viscosity, and a reduction in the size of the hysteresis loop corresponding to a reduction in damper stiffness[14, 15]. Similar results were found by several other sources with the predominant conclusion that an increase in temperature reduces the force that a MR Damper will produce [5, 8-11, 13-15, 33, 36]. This was found to be true across different types of MR Dampers including a UNR mountain-bike damper, an automotive damper, and a HMMWV MR fluid damper[11]. This means that there is an error associated with the actual force produced by the MR Damper compared to the desired force from the control strategy. Note that the influence of temperature on MR Damper force is the second source of error within many controller designs. The first source of error was mentioned in the previous paragraph concerning the desire to replace the linear relationship between the current command signal and the desired MR Damper force with a nonlinear invertible model [1, 3]. Both of these sources of error will be addressed by the proposed NLDIM.

Another notable temperature-induced problem was associated with the use of force feedback systems. Although a relatively expensive solution, PID with force feedback is traditionally considered to be an accurate control strategy that can compensate for tracking errors. Interestingly, Batterbee and Sims discovered that the system response, stability and overall effectiveness of a PID controller was reduced as temperature varied. They concluded that there was a need to have carefully chosen gains which accounted for temperature change [15].

Wilson presented a temperature dependent controller for an MR seat suspension [13]. The equation to calculate current had three constants that were temperature dependent: C_{p1} , C_{p2} , and C_{p3} . Their values were determined from a graph that characterized post yield damping with respect to temperature. However, for the purpose of that particular study, only the values for an average temperature of 50°C were used. The model proposed in this research addresses this issue by creating a lookup table of temperature correction factors that can be used in real-time as the temperature varies. Furthermore, Wilson stated that a 20% reduction in the controllable yield force and 13% degradation in transmissibility over a temperature range spanning 10°C to 100°C experienced in his study did not warrant temperature compensated control [13]. This may be true for that particular application however; these numbers do show that there is room for

improvement – an improvement that can be delivered by the temperature correction built into the proposed NLDIM.

Among the numerous approaches to modeling an MR Damper and implementing a control strategy, there were a few notable systems that almost met the design requirements which included the work of Wilson, Boada, Lui and others [13, 15, 24, 27, 30, 32, 33]. Lui developed a temperature dependent Skyhook control that allowed real-time implementability, low cost, and temperature correction. The Skyhook equations were modified to insure that if the desired force was less than the viscous force, then the MR Damper would not be activated.

$$F_d = \begin{cases} c_s \dot{y}_2 & \dot{y}_2(\dot{y}_2 - \dot{y}_1) > 0 \text{ \& } c_s |\dot{y}_2| > c_v |\dot{y}_2 - \dot{y}_1| \\ c_v (\dot{y}_2 - \dot{y}_1) & \textit{otherwise} \end{cases} \quad (2.1)$$

Also, a corresponding current calculation reflected this change and included temperature dependence seen in the equations below. The plastic viscosity $\mu(T)$ was a function of temperature.

$$i = \begin{cases} \left[\frac{c_s |\dot{y}_2| - k\mu |\dot{y}_2 - \dot{y}_1|}{\alpha} \right]^{\frac{1}{\beta}} & \dot{y}_2(\dot{y}_2 - \dot{y}_1) > 0 \text{ \& } c_s |\dot{y}_2| > k\mu |\dot{y}_2 - \dot{y}_1| \\ 0 & \textit{otherwise} \end{cases} \quad (2.2)$$

$$\mu(T) = \begin{cases} 0.245e^{-0.0332T} & T < 0 \\ 0.245e^{-0.0079T} & T \geq 0 \end{cases} \quad (2.3)$$

This resulted in a decrease (improvement) of the ride displacement and velocity PSD by 10% to 45% over the temperature range of -40°C to 150°C when compared to an uncompensated system. Additionally, the RMS displacement and acceleration of the sprung mass were reduced by 18% and 7% respectively [33]. Unfortunately, due to the potential performance improvement of a high fidelity inverse model as proposed by Reader[1], this model did not meet all of our requirements.

3) Modeling objectives

3.1) Overview

The modeling objective for this work was to create an improved open-loop strategy for controlling a MR Damper. This required the development of an invertible high fidelity MR Damper model, which we call a Nonlinear Dynamic Inverse Model (NLDIM). This model was comprised of two sub-systems. Following the research of Reader [3] the first sub-system was an invertible and separable function that characterized the static nonlinear behavior of the damper.

Building upon the research of Reader [3], the second sub-system was a linear filter that captured the dynamics, which modeled the hysteretic behavior of an MR Damper.

The origins of the NLDIM stem from the previous work of Reader [3] where he demonstrated that a separable inverse model of a MagneRide Damper in conjunction with Skyhook control produced a corrected command signal (current) that resulted in a damper force that more accurately matched the desired Skyhook force.

3.2) Reader's Model

The forward version of Reader's model is comprised of two cascaded elements. The first is a separable model capturing the nonlinear non-hysteretic behavior and the second is a linear filter capturing the hysteretic dynamics. The separable model is shown below[3].

$$F_{back}(v_{rel}, i) = f(i) \times g(v_{rel}) \quad (3.1)$$

There are two components to this separable model, a current dependent component $f(i)$ and a velocity dependent component $g(v_{rel})$. The current dependent function has an offset at zero current, representing the fact that a MR Damper behaves like a passive damper during the off state. The curve then deviates from a linear curve at some higher current representing the saturation limit of a MR Damper. Lastly, $f(i)$ is monotonic in nature which satisfies a critical requirement for the invertibility of the entire model[3].

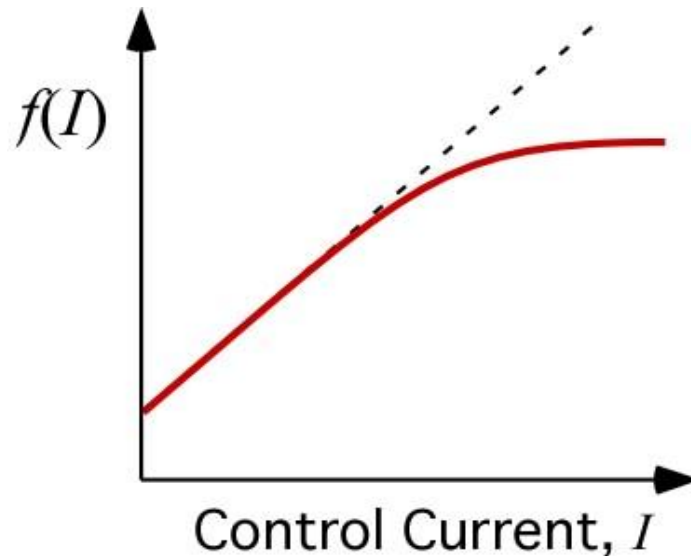


Figure 3.1. The $f(i)$ function represents the current dependent behavior of the MR Damper. It has an offset at zero current and deviates from linearity near the saturation limit

The velocity component $g(v_{rel})$ is sigmoidal in nature and captures the velocity dependent nonlinearity of the MR Damper in a simple non-parametric description. This function can also

be represented by the derivative of the hyperbolic tangent function[3], although that would require a relatively expensive real-time implementation.

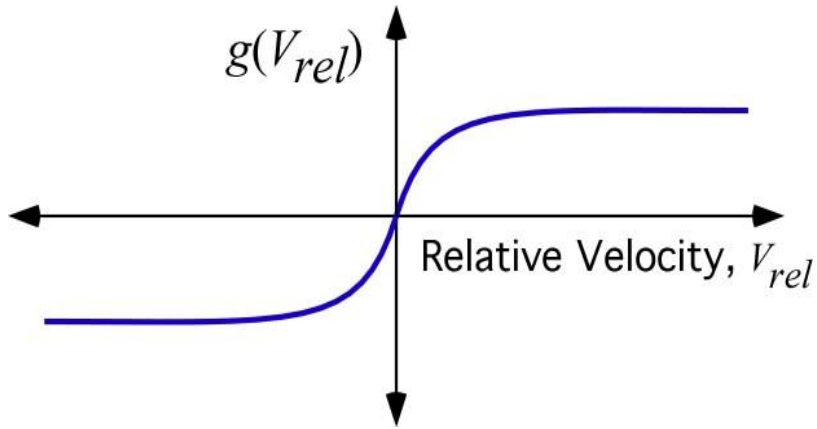


Figure 3.2. The $g(v_{rel})$ function captures the velocity dependent nonlinearity of the MR Damper; it is sigmoidal in nature

The hysteretic component of Reader's forward model was approximated by a tuned first order lag filter, whose transfer function is shown below[3].

$$H(s) = \frac{F_{MR}}{F_{back}} = \frac{a}{s + a} \quad (3.2)$$

The inverse of the separable function was

$$i = \begin{cases} i_{max} & |F_{back}| > \max |F_{back}(i, v_{rel})| \\ f^{-1} \frac{F_{back}}{g(v_{rel})} & \frac{F_{back}}{g(v_{rel})} > 0 \\ 0 & \frac{F_{back}}{g(v_{rel})} \leq 0 \end{cases} \quad (3.3)$$

And the inverse of the hysteretic filter was a first order lead filter as shown below[3].

$$H^{-1}(s) = \frac{F_{back}}{\hat{F}_{MR}} = \frac{b s + a}{a s + b} \quad (3.4)$$

Here \hat{F}_{MR} is the desired force sent from a control algorithm such as Skyhook. A complete inverse model representation from Reader's work is shown in Figure 3.3 below.

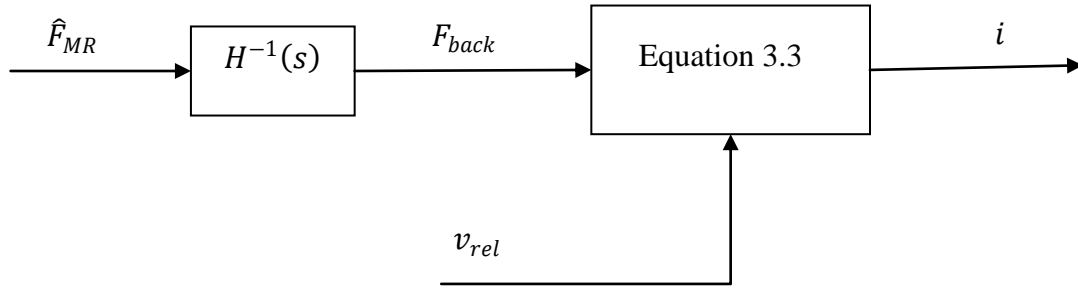


Figure 3.3. Visualization of Reader's inverse model

3.3) Proposed Temperature Dependent Model

One goal of this research is to build upon the approach proposed by Reader by including temperature dependence. Reader's model was only developed at a nominal temperature.

Prior to this investigation, it was unknown as to which components of the model were temperature dependent. Initially, each component was assumed to be temperature dependent until analyzed and proven otherwise. The investigation began with the backbone and dynamic models below.

$$F_{back}(v_{rel}, i, T) = f(i, T) \times g(v_{rel}, T) \quad (3.5)$$

$$H(z, T) = \frac{\hat{F}_{MR}}{F_{back}} \quad (3.6)$$

It can be seen that temperature dependence T has been added to every component. Further investigation into each of these components separately will determine if the temperature dependent term T should be removed, remain, or developed further.

As with the model proposed by Reader and in compliance with the design requirements previously set forth, this temperature dependent model must be simple, contribute to the linearization of the MR Damper system, and accurately capture the nonlinear characteristics of the MR Damper. Furthermore, the current dependent component $f(i, T)$ must be monotonic in order to satisfy invertibility requirements.

It must be emphasized that Equation 3.5 above represents the starting point of the model, not the final version. After each model component is individually developed in subsequent sections, the final version of the proposed model will be given.

4) Experimental Testing

A series of experiments were conducted at the VIPER Service Facility to record the dynamic behavior of a MR Damper under a range of operating conditions of current, velocity, and temperature. The test specimen was a MagneRide MR Damper manufactured by Delphi Corporation and measurements were made using a Roehrig Electro Magnetic Actuated (EMA) Shock Dynamometer. Other equipment included a GW Instek GPS-2303 current source, an infrared temperature gun, a K-type thermocouple, a Fluke 87V True RMS Digital Multimeter, and a Dell Precision T3400 desktop computer.

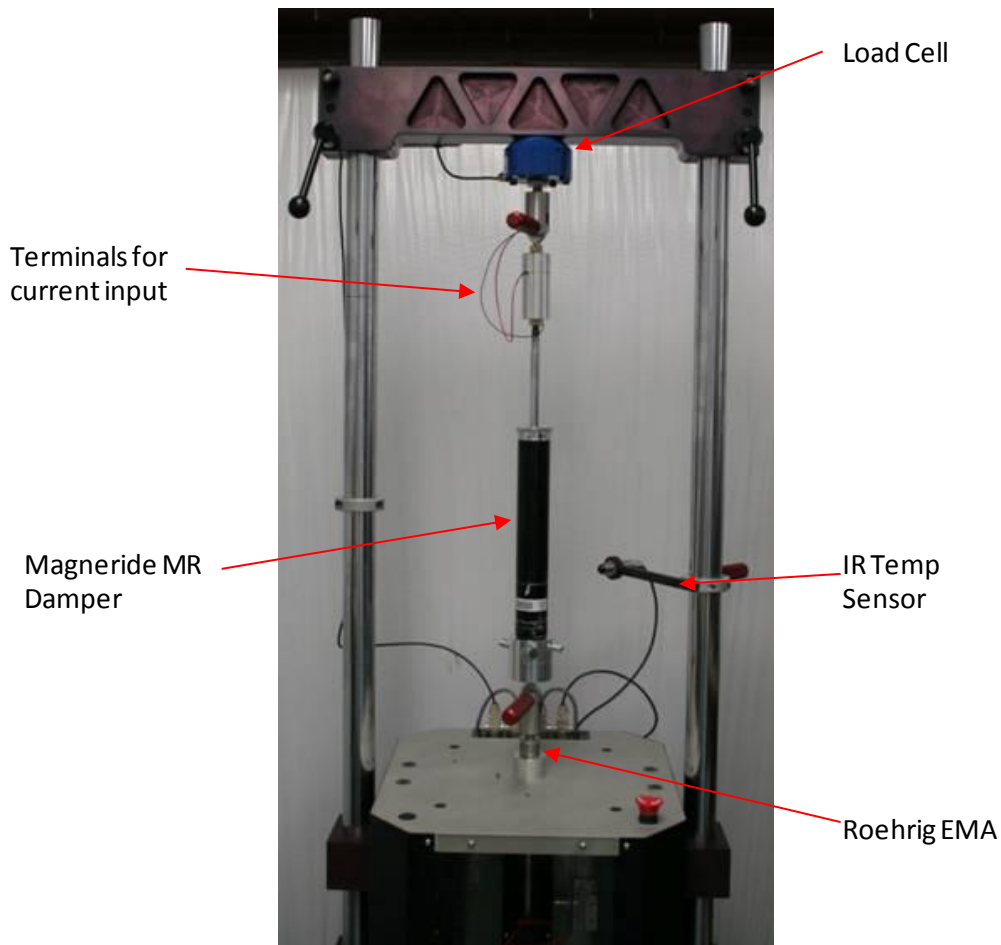


Figure 4.1. Experimental setup on Roehrig EMA

There were two input or “drive” signals in the experimental setup, and four output signals that were recorded. The two inputs were the excitatory displacement that was input via the lower shock mount on the Roehrig EMA, and the current input to the MR Damper from the current source. The displacement input was a sinusoidal wave of 2.387 Hz, with one inch amplitude, nine cycles in length. The DC current signal to the MagneRide MR Damper was adjusted to the

desired level by a knob on the current source. The current directly affected the effective damping coefficient - the greater the current, the greater the achievable damping force. The measured outputs were the force produced by the MR Damper, the relative velocity across the damper, the damper case temperature read by the IR temperature sensor, and the temperature of a thermocouple mounted to the damper casing. The thermocouple measurements were only monitored to validate the accuracy of the IR temperature sensor. For post-processing and analysis, the values of the IR sensor were used.

The experiment consisted of forty tests, broken into ten groups. The MR Damper was excited by the sinusoidal displacement signal at the four specific currents of 0, 1, 2, and 3 Amps, at the ten different temperatures of 84, 97, 111, 122, 132, 141, 151, 162, 171, and 181^o Fahrenheit. To ensure consistency, for each test, the temperature was allowed to fall below the desired test temperature. Then the Roehrig EMA warmed up the damper until the IR sensor read the target temperature, at which time, the EMA automatically ran the predefined nine period sinusoidal test signal. This was repeated for every current at every temperature specified above, for a total of forty unique runs.

5) **Characterization of the Separable Model**

5.1) **Data Extraction**

The raw signal recorded from the EMA contained both noise and inconsistencies within the data pertaining to the ramp-up in force upon start-up of the experimental runs. As a result a second order low pass butterworth filter with a 20 Hz cutoff frequency was used. This break frequency allowed the first eight harmonics to remain in the signal, insuring minimal distortion to the waveform of interest. Additionally, the beginning and tail end of the original 9 period signal was eliminated to remove startup and finish inconsistencies. To accompany the trimmed force signal, the time and velocity vectors were adjusted accordingly. Figure 5.1 and Figure 5.2 below shows the force versus time and velocity versus time for a sample run.

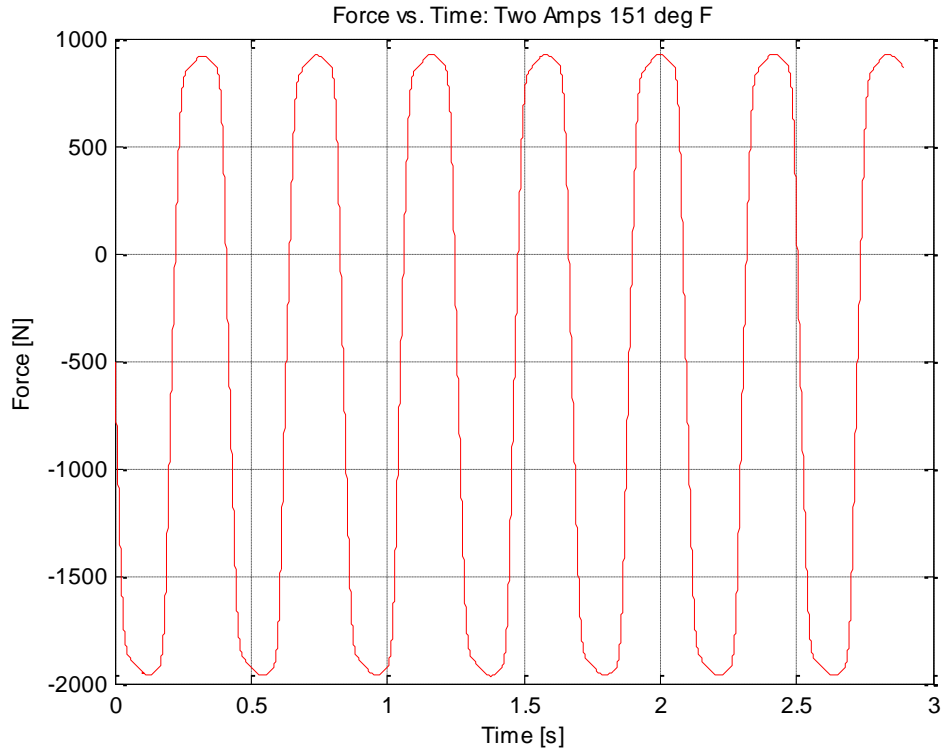


Figure 5.1. Experimental Force vs. Time response measured at 2A and 151^oF

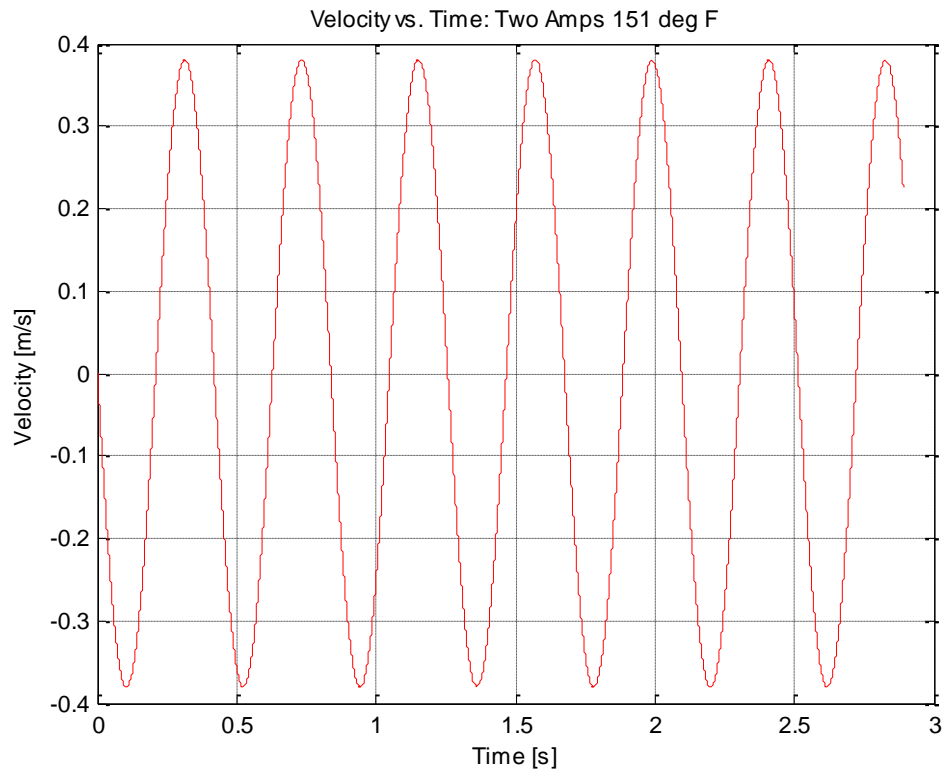


Figure 5.2. Experimental Velocity vs. Time response measured at 2A and 151^oF

The Force was then graphed versus velocity to visualize the dynamic hysteretic behavior of the damper.

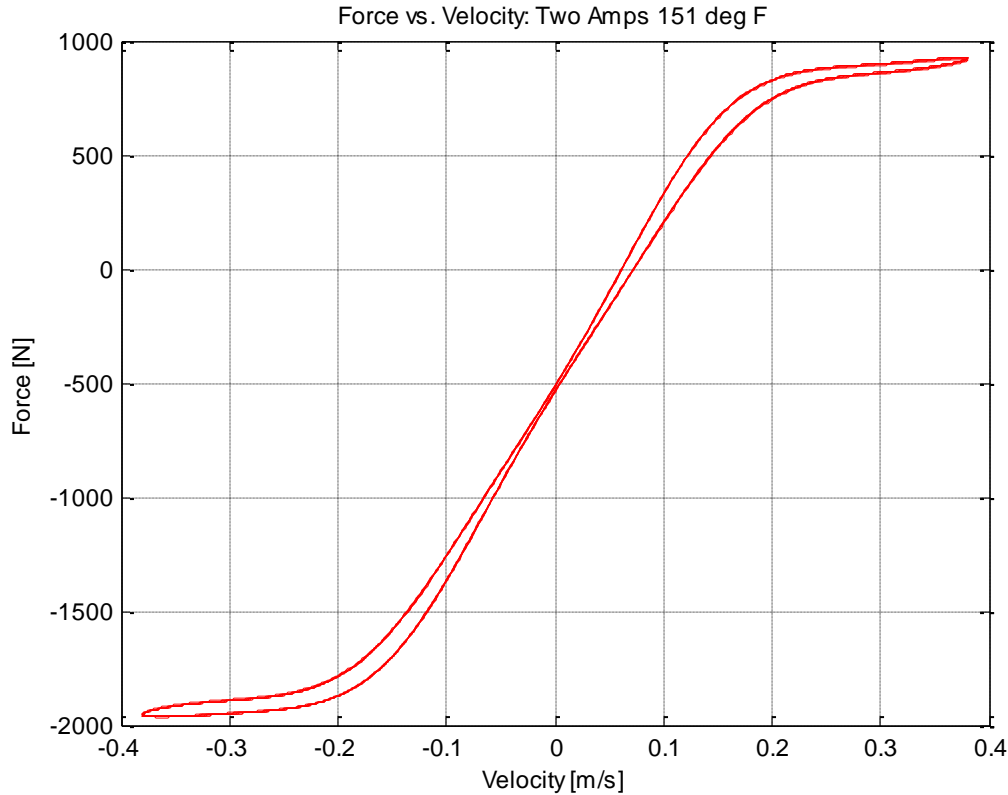


Figure 5.3. Experimental Force vs. Velocity measured at 2A and 151^oF

Figure 5.3 above shows the bi-linear response of the force-velocity curve which corresponds to the high and low speed damping respectively. As the velocity increases, so does the force. However, the increase in force becomes negligible after a certain velocity. This result is specific to each damper, although the same general bi-linear trend applies to a wide range of MR Dampers. Also, the hysteretic nature of the damper is evident in the fact that the experimental response shows different force values at the same velocity. This is because the damper produces a different force when in compression versus rebound.

5.2) **Backbone ID**

Once the time-series data was pre-processed at each of the forty operating conditions, the forward separable model was ready to be developed. The first component of the model that needs to be estimated is called the backbone curve. This curve captures the nonlinear static behavior of the damper as developed in Reader's work [1, 3]. Equation 5.1 below shows that the

dynamic damper force that is measured from the Roehrig EMA Shock dyno, is comprised of a hysteretic and non-hysteretic component.

$$F_{MR}(v_{rel}, i, T) = F_{back}(i, v_{rel}, T) \times H(z, T) \quad (5.1)$$

This non-hysteretic component $F_{back}(i, v_{rel}, T)$, called the backbone force, contains the nonlinear relationship between the damper force and the relative velocity, temperature, and current. This backbone force represents the sub-system from which the separable equation is developed. The creation of the separable model is the focus of Chapter 5. The hysteretic component $H(z, T)$ is the focus of Chapter 6; it contains the dynamic behavior of the MR Damper.

The backbone force curve was extracted from the experimental data by dividing the velocity array into fifty bins. Then the corresponding hysteretic force was averaged with respect to those bins. This created a backbone force curve from the dynamic test data, both of which are shown in Figure 5.4. To avoid confusion in this document, the backbone force will be defined as the force versus velocity curve that characterizes the non-hysteretic force from the experimental data. The backbone force is represented by the term $F_{back}(i, v_{rel}, T)$ and corresponds to the non-hysteretic force that is generated by a model, especially the separable forward model. Technically, the backbone force function $F_{back}(i, v_{rel}, T)$ does create a “backbone shaped” non hysteretic force curve. However, the word “backbone” refers to the shape of the curve and the fact that it was derived from experimental data, while $F_{back}(i, v_{rel}, T)$ will correspond to the non-hysteretic force output from a model.

To ensure that the method of calculating the backbone did indeed produce a correct result, an optimization was run after the entire damper model was developed. Assume momentarily that the entire forward separable model and the hysteretic model have been developed. Hold everything constant except for the backbone curve. The *fmincon* optimization function in Matlab was allowed to change the shape of this backbone curve so that the force output of complete damper model could better match the original experimental MR Damper data. Interestingly, for any given current and temperature sample, *fmincon* could not produce an improved backbone curve. This was quantified by either an increase or no improvement in the error between the damper model output and the target experimental data. This served as a restricted validation that the calculation of the backbone curve was robust.

In Figure 5.4 below, two curves are shown that detail the difference between the hysteretic force and the backbone force.

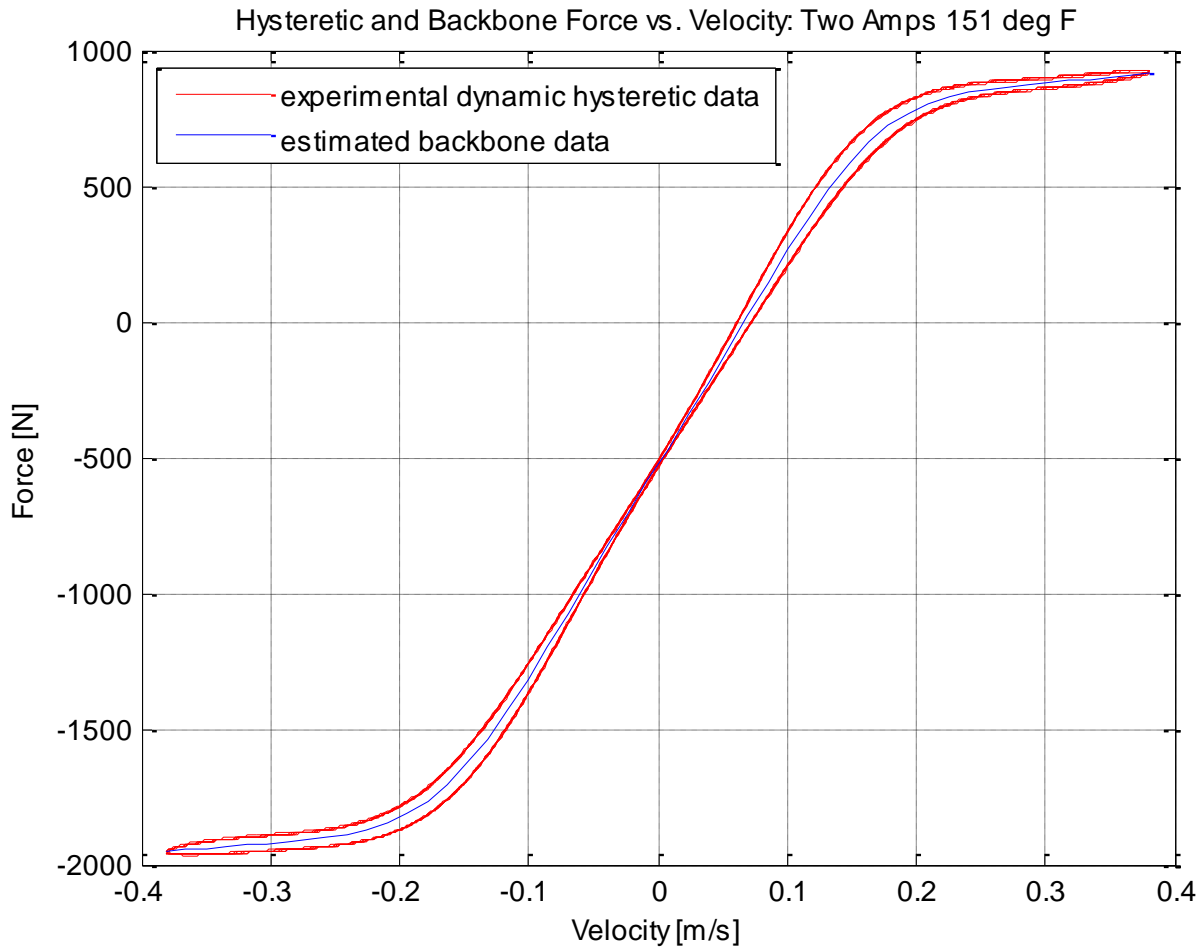


Figure 5.4. Dynamic Experimental Data and Estimated Backbone Data measured at 2A and 151^oF

The red curve is the experimental dynamic force versus velocity for six periods. As mentioned previously, the hysteretic nature of the damper is evident in the fact that the red curve shows different force values for the same velocity. Conversely, the blue backbone curve, which lies between the upper and lower bounds of the red curve, is estimated from the experimental data and represents the non-hysteretic force versus velocity. The backbone curves were calculated for all forty runs and grouped with their respective current. This is shown in Figure 5.5 below.

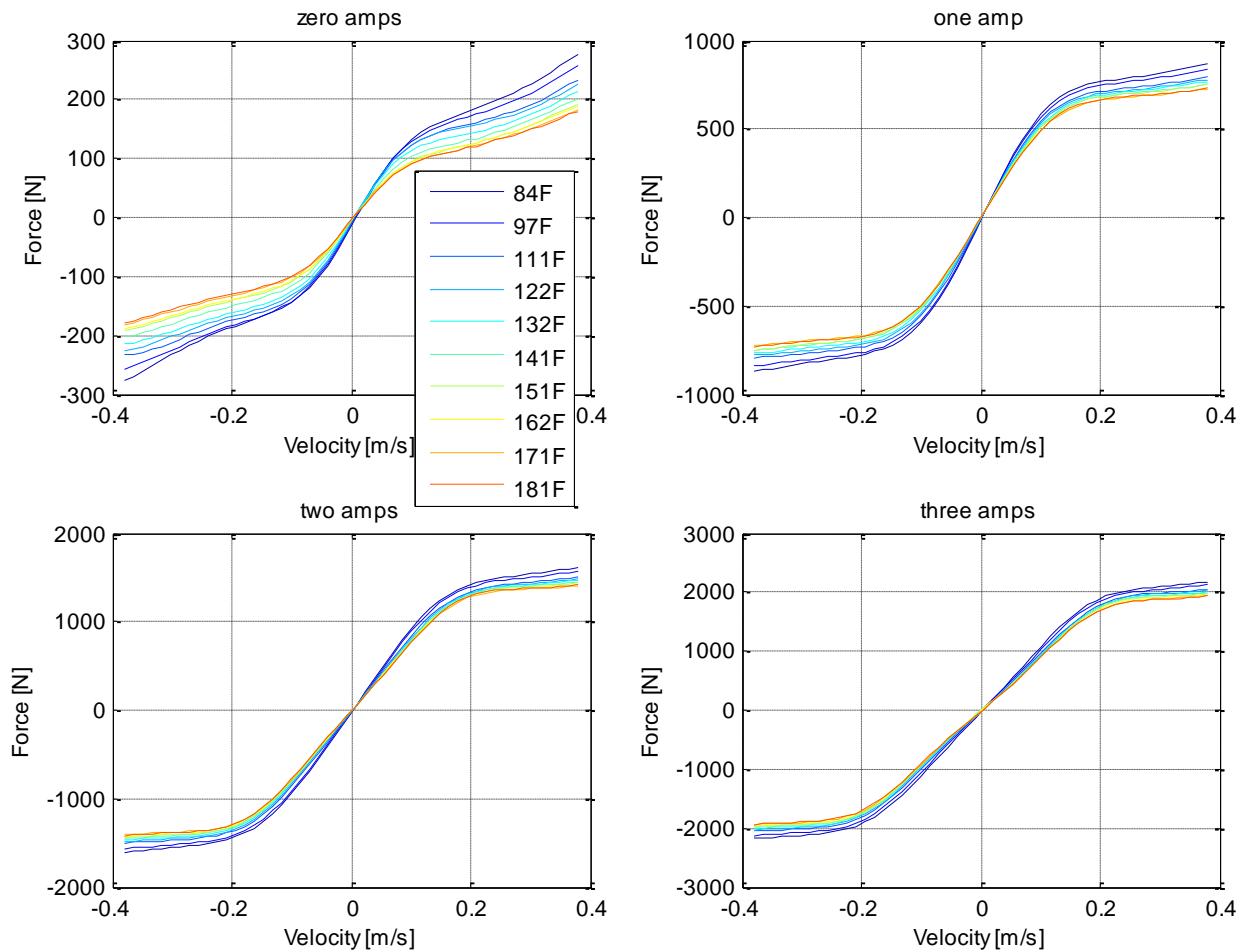


Figure 5.5. Backbone force curves for all temperatures at 0, 1, 2, and 3 Amps

The figure above as well as Figure 5.6 shown below, illustrate that the backbone curves are not only current dependent, but also exhibit a velocity and temperature dependence. As the current increases, the absolute maximum force produced by the damper increases. Furthermore, the range of peak forces produced across the 10 temperatures is larger at the higher currents. The spread of the force range is about 100N at zero amps, 150N at one amp, 200N at two amps, and 250N at three amps. This shows that for this particular damper the temperature affects both the electromagnetic properties and rheological properties of the shock. The effect of temperature on the rheological attributes (ability for the MR fluid to flow through an orifice in the piston) is greater at zero amps because there is no current to create an electromagnetic field and alter the MR fluid. However as the current to the MR Damper is increased, the temperature has a greater effect on the electromagnetic characteristics. This is demonstrated by the 250N spread in peak force at 3 amps, which is more than double the force spread at zero amps.

Looking more closely at Figure 5.6 below, the effect of temperature can be seen in more detail; as the temperature rises, the force produced decreases. This is largely due to the decrease in effective viscosity of the fluid [5, 8-11, 13-15, 33, 36].

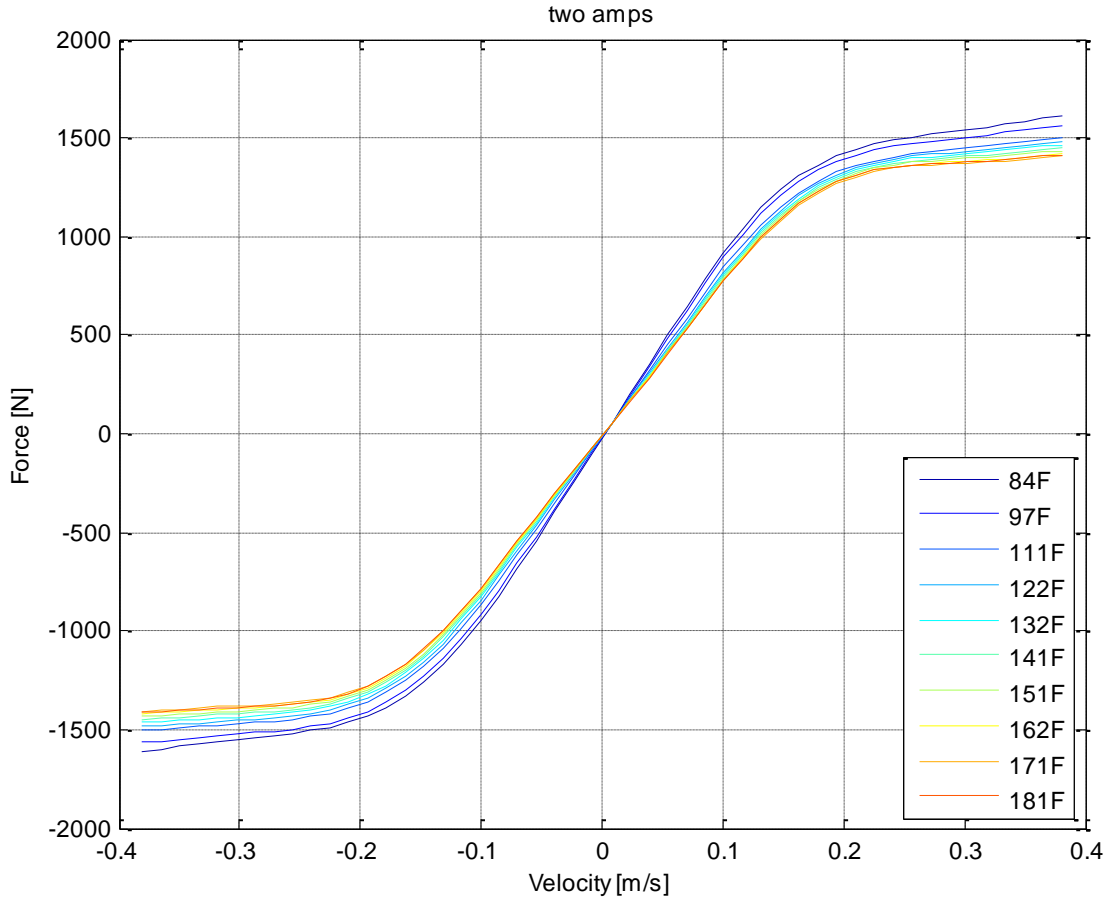


Figure 5.6. Close up of backbone force curves for 2 Amps

To capture the influence of the velocity, current and temperature, the backbone curve was further separated into three components: $g(v_{rel}, T)$ which served as the universal and non-dimensional backbone shape capturing the high speed and low speed behavior of the damper; $f(i, T)$ served as the current dependent term that would scale the backbone to its respective force region; and finally $h(T)$ would account for temperature correction. Also, despite there being a temperature correction component $h(T)$, the temperature T has not been removed from the velocity or current dependent components because it has not yet been determined that these components are temperature independent. Once this independence is demonstrated in subsequent sections, the temperature term will be dropped. Furthermore, $h(T)$ was originally thought to have only been temperature dependent, however, as will be shown in later sections, $h(T)$ is more complex than previously envisioned.

5.3) Velocity Dependent Component: $g(v_{rel})$

The function $g(v_{rel}, T)$ is responsible for capturing the fundamental nonlinear shape of the backbone curve. Given that $g(v_{rel}, T)$ represents the velocity dependence for the separable model, it is desired that it be universal across all other states. This statement reflects the belief

that $g(v_{rel}, T)$ is only a function of velocity. It is also a desire for this function to be non-dimensional hence, all of the backbone curves were normalized to a range of -1 to +1 through a three step process. First in the three steps was that all forty of the backbone curves were scaled down to the room temperature curve for each respective current. Figure 5.7 plots this scaling below.

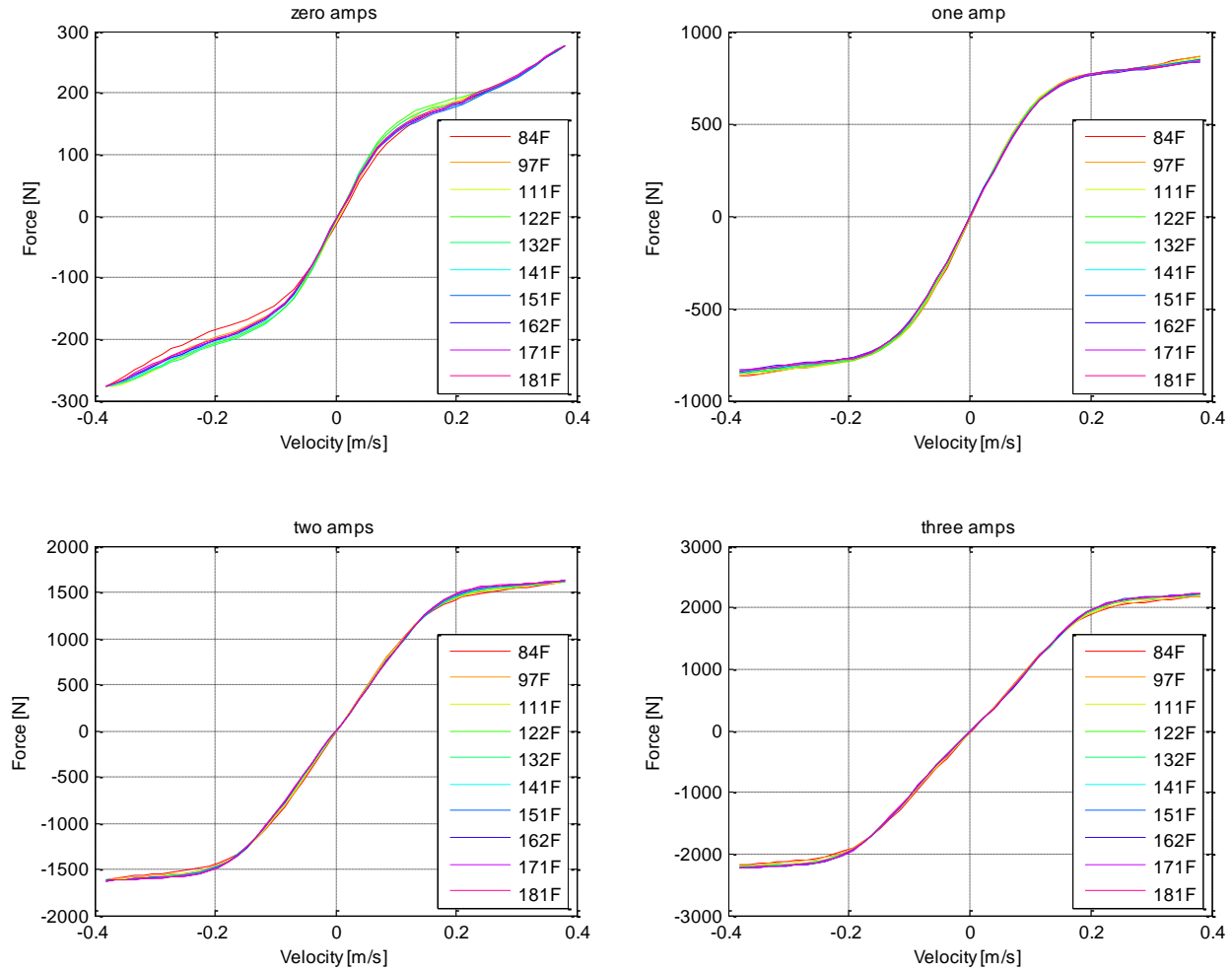


Figure 5.7. Collapsed backbone force curves for each respective current

With a few exceptions at zero current, the variation in each of the scaled curves at a given current is remarkably small. This lends a great deal of credibility to the assumption that a temperature-dependent correction factor can be isolated. Next, the ten collapsed backbone curves for each current were averaged as a group. This left four backbone curves, one for each current, shown in Figure 5.8 below.

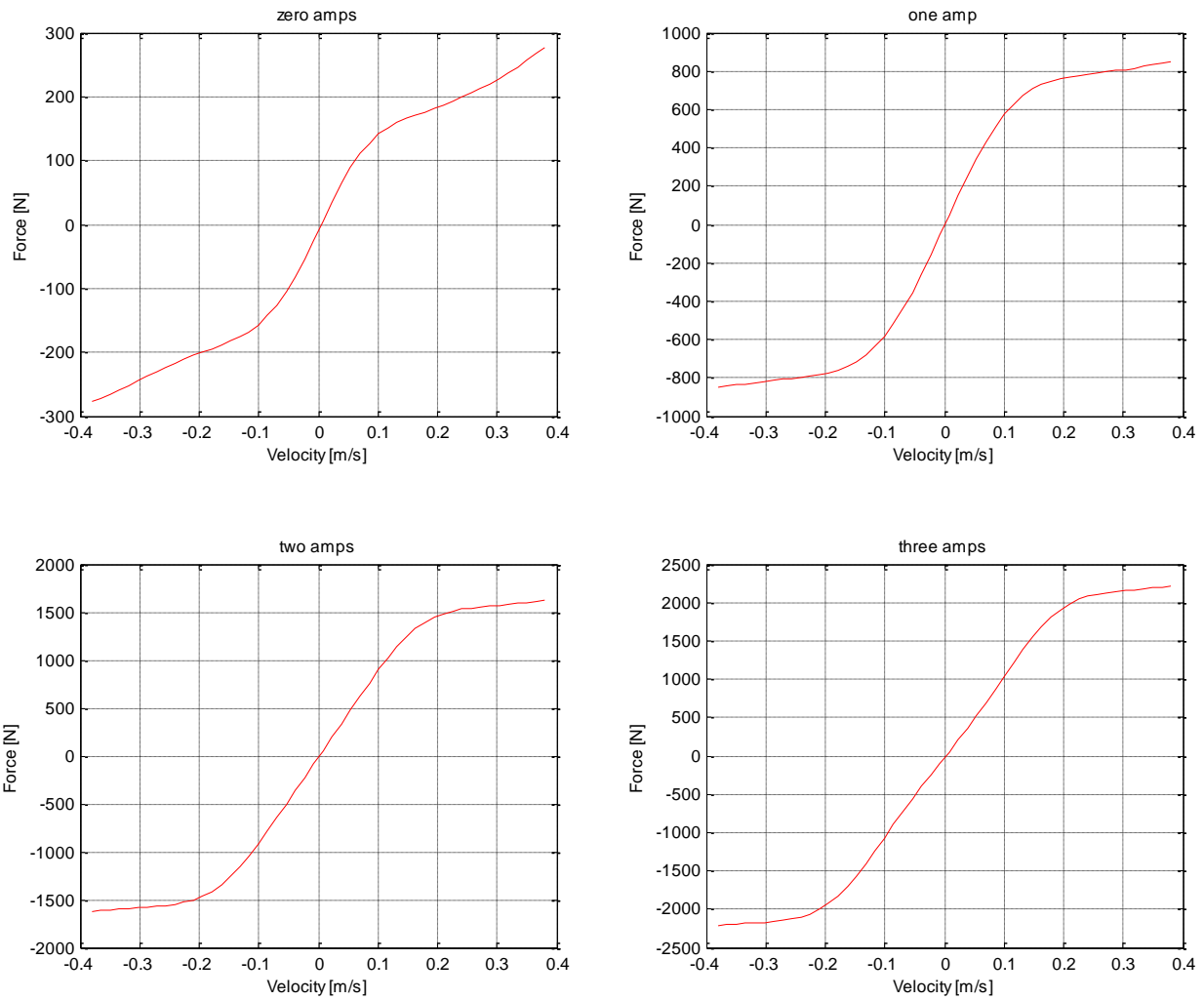


Figure 5.8. Averaged collapsed backbone force curves that are independent of temperature

The averaging performed up to this point removed the influence of temperature on $g(v_{rel})$. Lastly, each curve was normalized by its own maximum value, resulting in Figure 5.9 below.

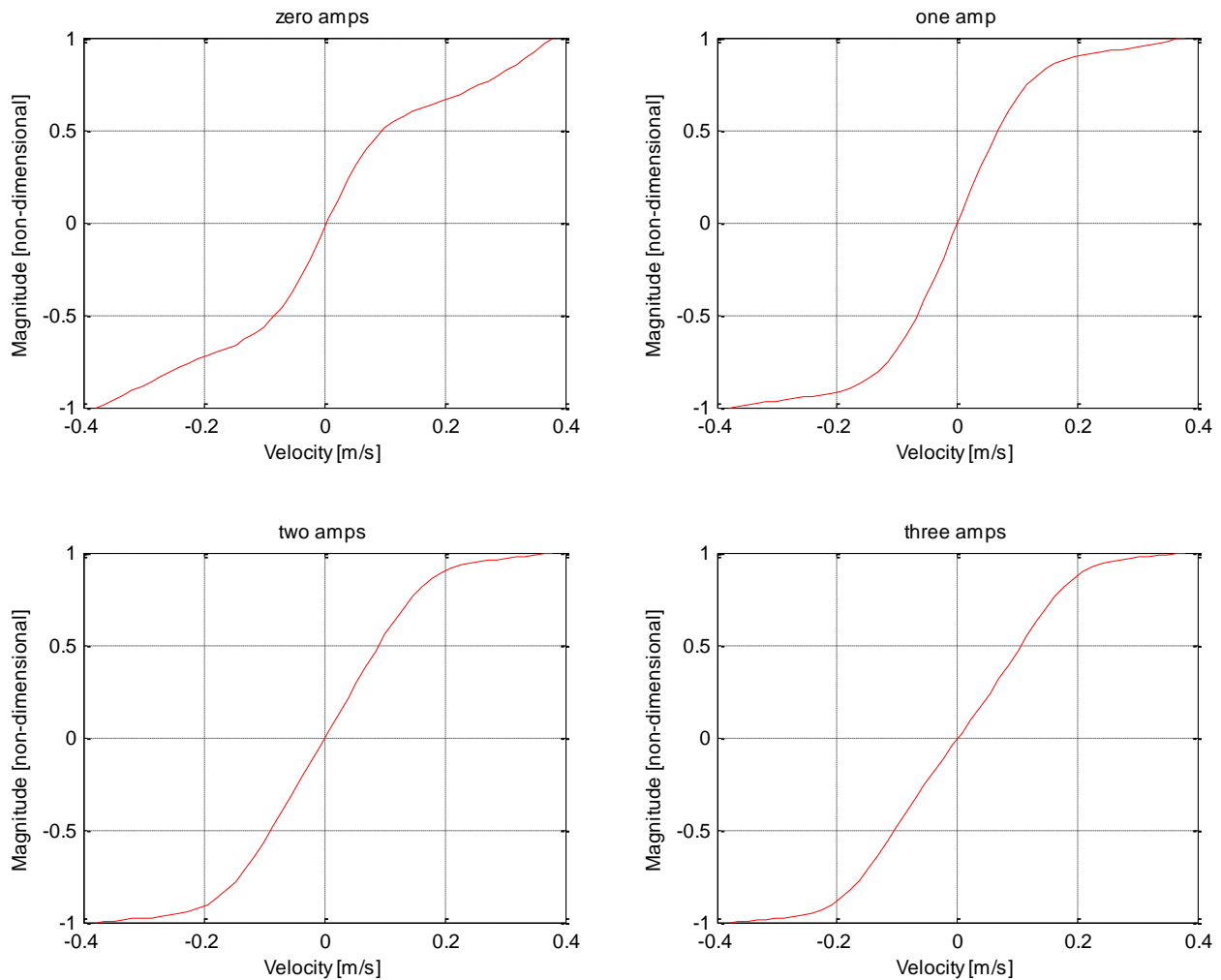


Figure 5.9. Normalized $g(v_{rel})$ at all four currents; they are independent of temperature

Looking at Figure 5.10 below, there are five lines, with four of them corresponding to an individual normalized $g(v_{rel})$ – one at each current. Observing the similarity between the “on” state, currents 1, 2, and 3 Amps, there is strong evidence that suggests the existence of a universal $g(v_{rel})$. The three “on” state curves were averaged and the result was the universal $g(v_{rel})$ seen as the red line. Due to the nature of the separable model, the $g(v_{rel})$ term is only dependent on the relative velocity across the damper, not the current or the temperature. This statement is satisfied through the averaging of the curves across the “on” states. Figure 5.10 below shows the universal $g(v_{rel})$ curve against the average $g(v_{rel})$ for each current. The term “universal” is used to describe this newly defined $g(v_{rel})$ because it is going to be the single $g(v_{rel})$ curve used at all operating temperatures and current values for this particular MR Damper, hence its “universal” nature.

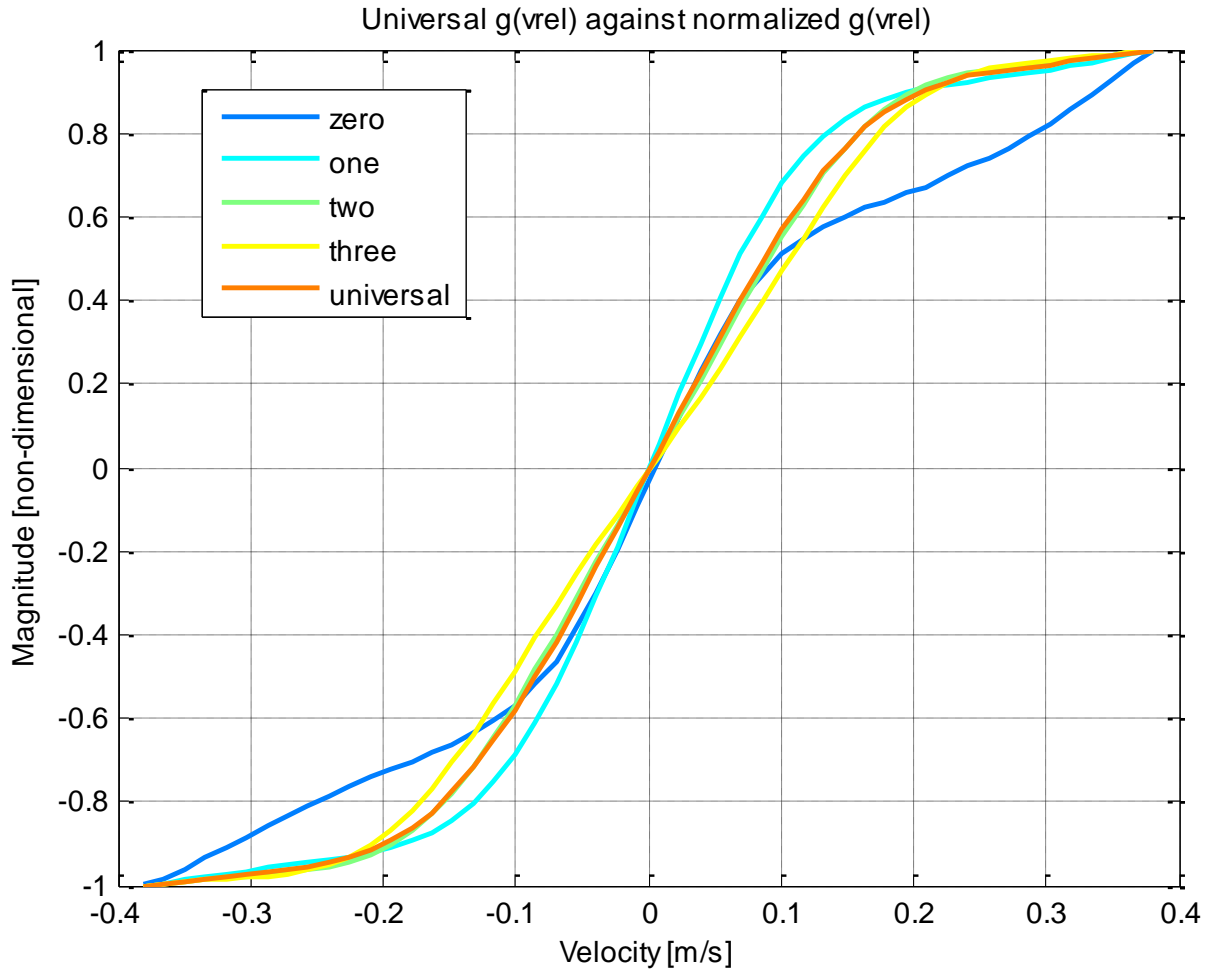


Figure 5.10. Four $g(v_{rel})$'s: one per current, as well as one universal $g(v_{rel})$

It can be seen that the universal $g(v_{rel})$ is biased towards the “on” state. This decision was motivated by the fact that the “on” state velocity dependence of the damper was much more closely related to each other than to the “off” state or zero current of the damper. Figure 5.11 below quantifies this relationship.

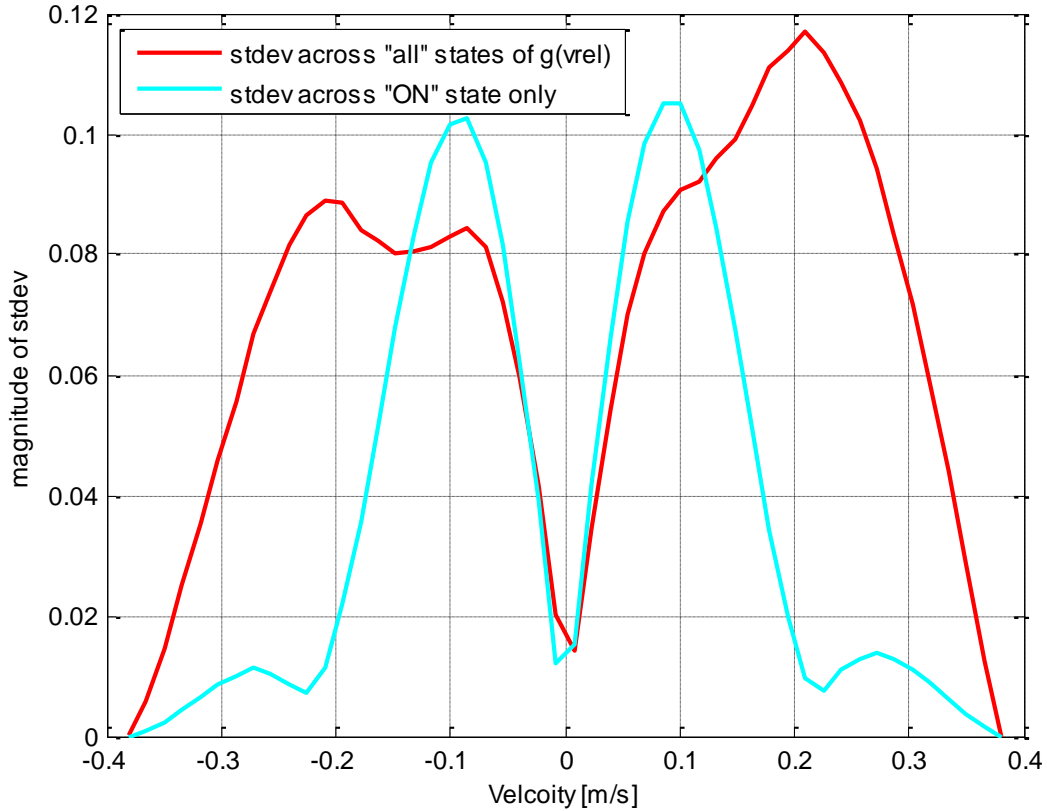


Figure 5.11. Standard deviation across "on" state $g(v_{rel})$ and "all" state $g(v_{rel})$

Figure 5.11 shows that the standard deviation between the “on” state $g(v_{rel})$ curves is a measure of the error in the universal function $g(v_{rel})$. This is compared to the standard deviation of $g(v_{rel})$ across “all” states (currents). Except for at low velocities, the “on” state values are much lower than the standard deviation across “all” states. This is because the “all” states curve included the $g(v_{rel})$ for the “off” state or zero Amp case. This large difference in damper behavior for the “on” and “all” states (or the difference between “on” and “off” states) will be observed again in other model components. Unfortunately, this result derived from experimental data prevents the use of a truly universal $g(v_{rel})$ function unless we are willing to accept the larger errors at zero current. This supports the decision to differentiate between “on” and “off” states due to their weak correlation.

5.4) Temperature Correction Function: $h(i,T)$

To capture the thermal influence on the original $F_{back}(i, v_{rel}, T)$, a correction factor, $h(T)$ had to be created. To generate this variable, the concepts of a target and a nominal value were required. The room temperature backbone curve for each current level, seen as the blue lines corresponding to 84°F in Figure 5.5 and Figure 5.6, was chosen as the nominal temperature, while the 40 backbone curves were chosen as the targets. The temperature function $h(T)$ was calculated to be the ratio between the backbone curve at a given target temperature versus the

nominal room temperature. Specifically, the number used for the ratio was the end point of each backbone curve. Both the top right end and the bottom left end of each curve were used to create two ratios for each sample. These two ratios were then averaged and that became the $h(T)$ for each curve. Fortunately, these two ratios were exactly the same due to the backbone curves being symmetric in the positive and negative directions. Figure 5.12 and Figure 5.13 below details all the values and progression of $h(T)$. Two figures are given to facilitate a more thorough understanding of this variable.

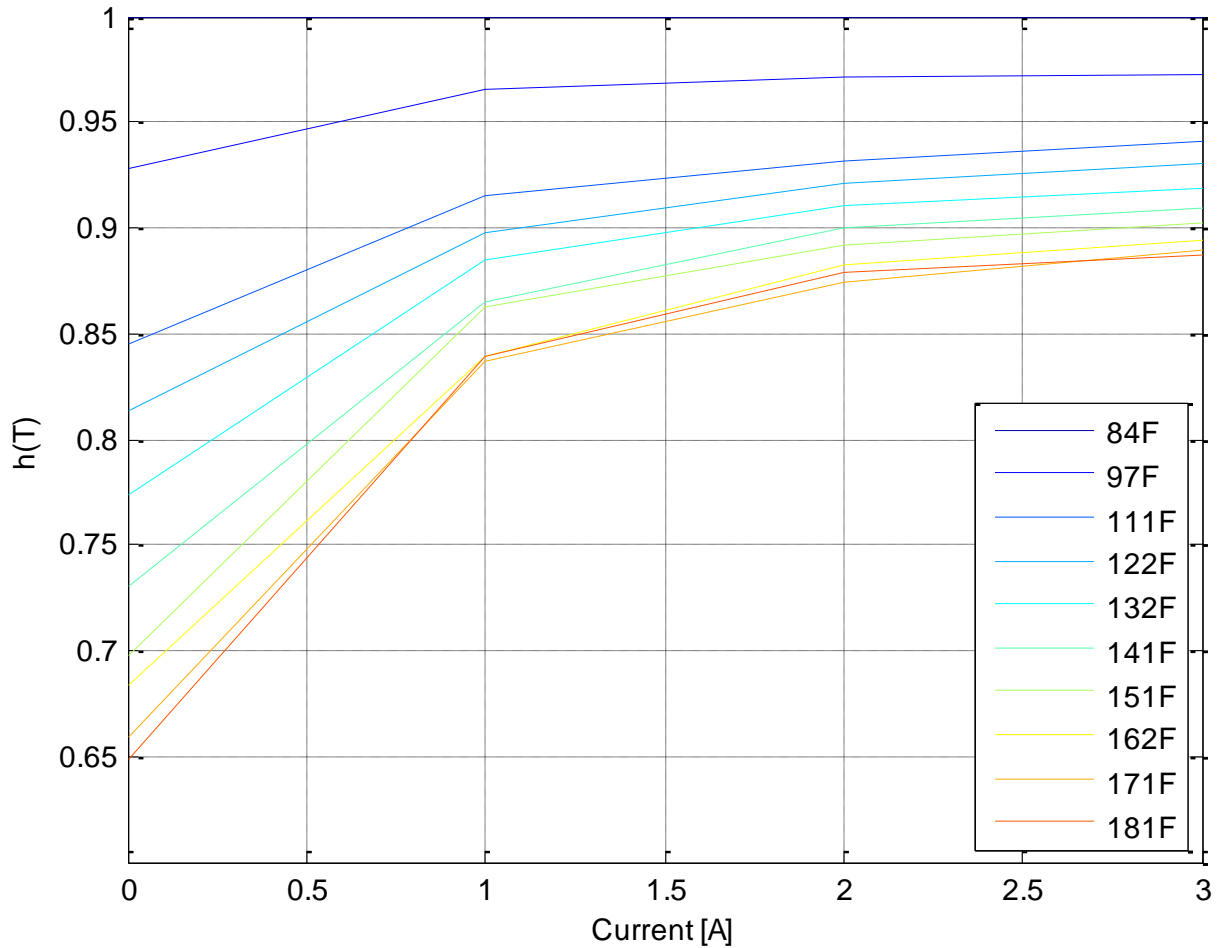


Figure 5.12. Progression of $h(T)$ across all temperatures and currents

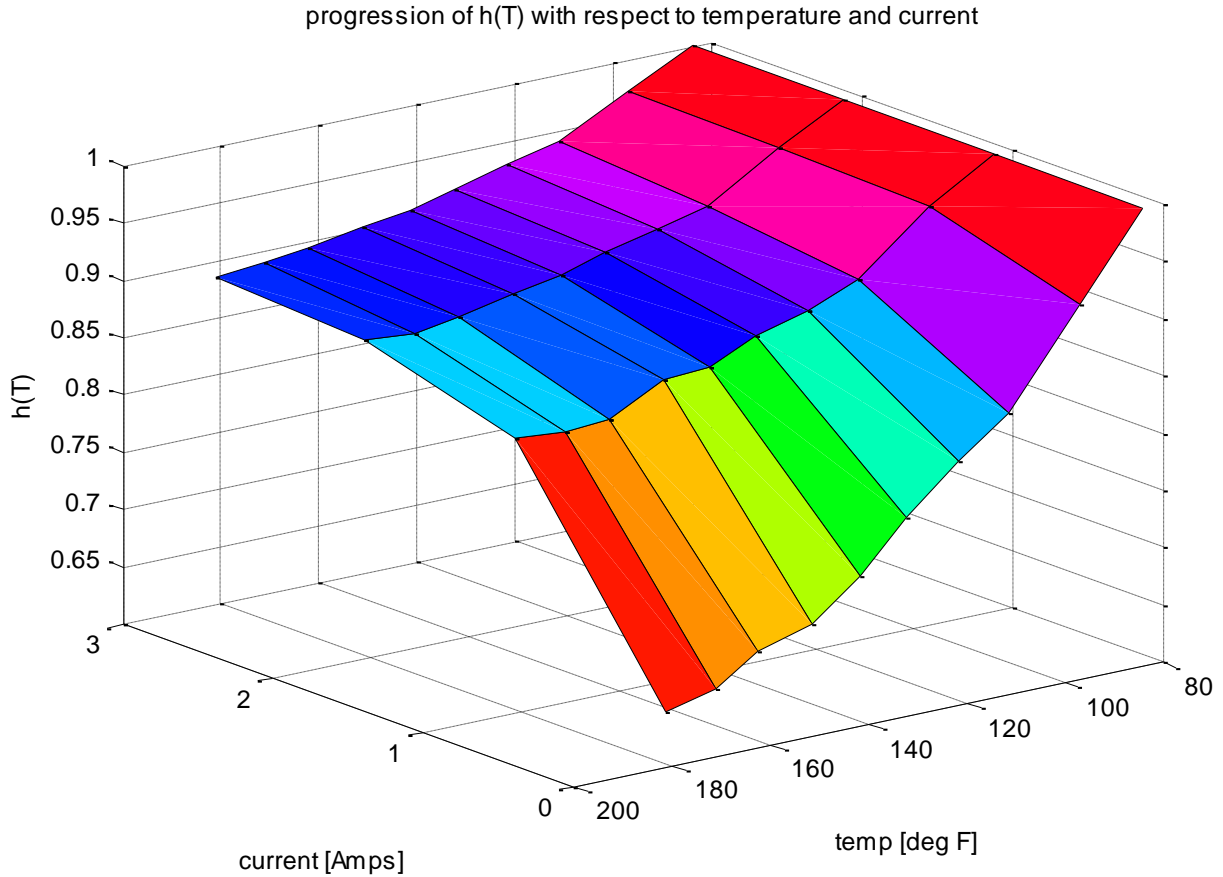


Figure 5.13. 3-D surface plot of the progression of $h(T)$

It can be seen in both figures above, that $h(T)$ has two distinct behaviors, one for the “on” state, and one for the “off” state. The values of $h(T)$ at one, two and three amps are much closer together for a given temperature when compared to the $h(T)$ values at zero amps. This is yet another example of the same dual natured behavior that was encountered during the determination of $g(v_{rel})$. It is also experimental confirmation that the function $h(T)$ will need to be current dependent. Because of this distinction, $h(T)$ will now be referred to as $h(i, T)$.

If the temperature correction factor $h(i, T)$ was independent of current, then it would be expected that all four values of $h(i, T)$ would be the same for a given temperature. This is clearly not the case; however, the values at one, two and three amps are reasonably close. This trend influences the development of a universal empirical formulation, just as it did for $g(v_{rel})$. In pursuit of this universal formulation, an average $h(i, T)$ was calculated for each temperature across 1, 2, and 3 amps. The zero amp case was omitted from the averaging and used as is because the MR Damper exhibits an unrelated behavior in the “off” state. Figure 5.14 below illustrates the average values of $h(i, T)$ at each temperature for the “on” state only (1, 2, and 3 Amps). The resulting correction factors do not deviate more than 13% from the nominal room temperature value over the range of temperatures tested in this study.

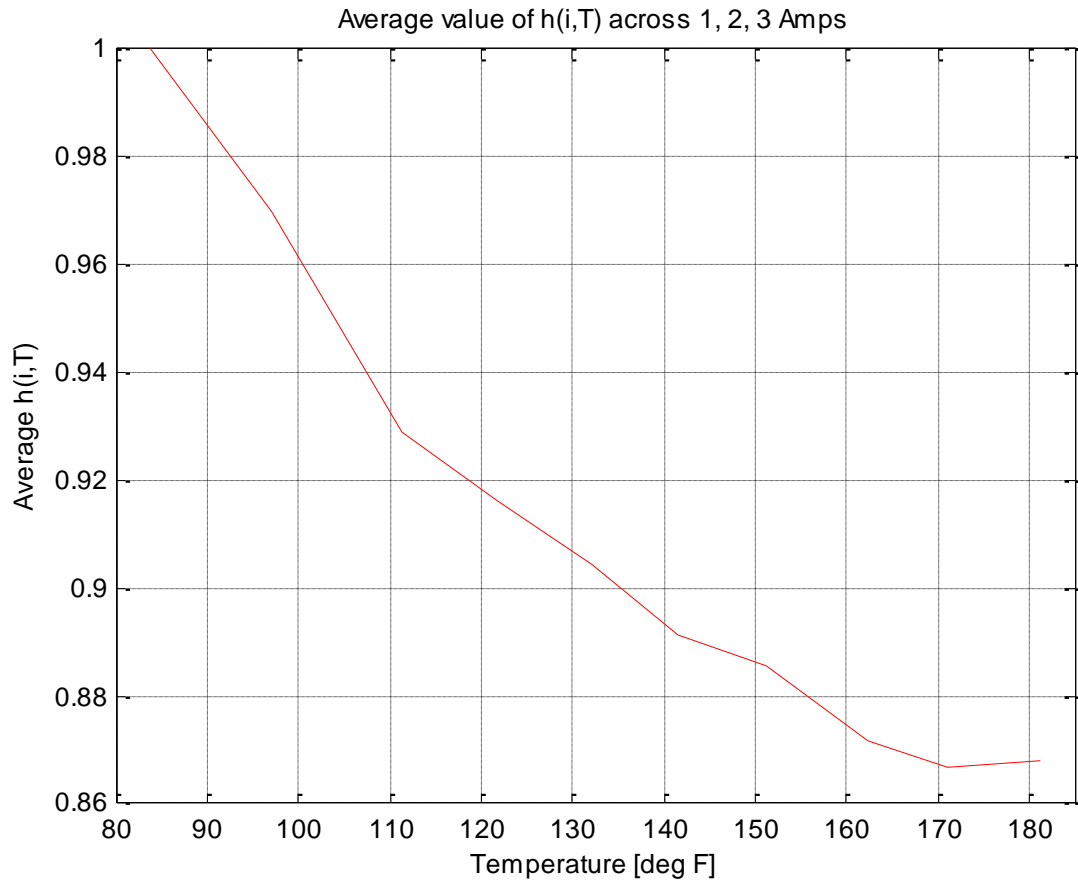


Figure 5.14. Average $h(i, T)$ across "on" state only

To account for the uncertainty in the averaged values of $h(i, T)$, Figure 5.15 below shows the standard deviation at all temperatures for the “on” state.

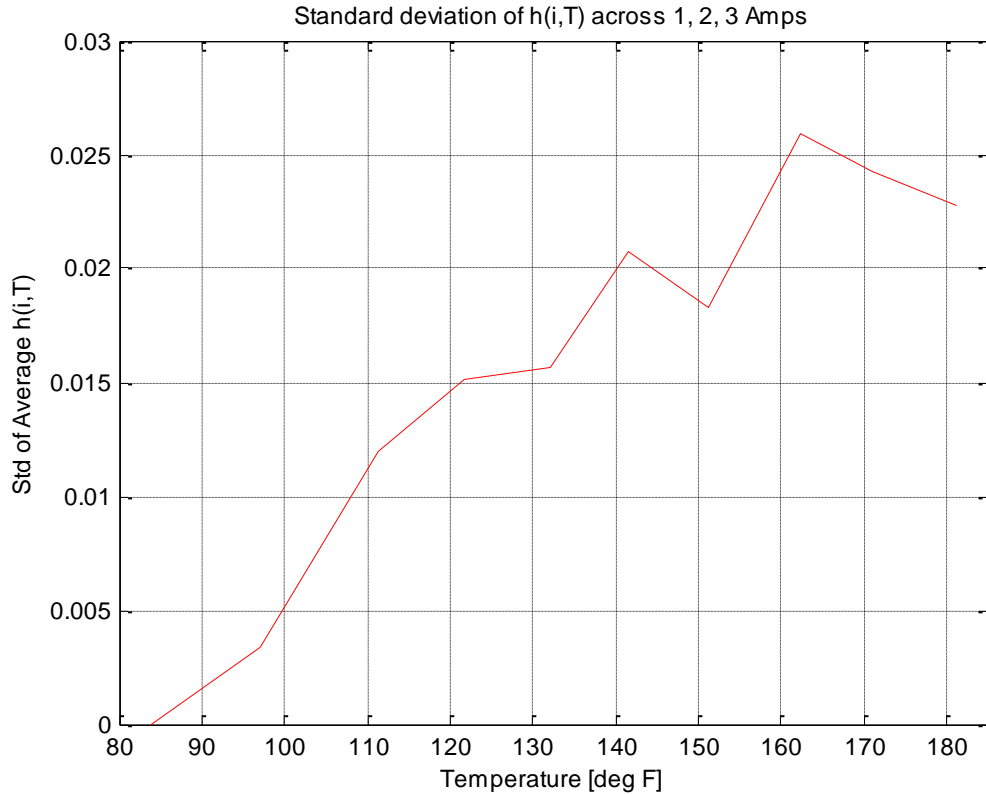


Figure 5.15. Standard deviation for average $h(i, T)$ across "on" state

The standard deviation is extremely low with a maximum deviation of only 2.5%, justifying a “universality” of $h(i, T)$ in the “on” state. This also bolsters confidence in the ability to use an averaged $h(i, T)$. To further validate the temperature correction variable, each backbone curve was divided by the finalized version of $h(i, T)$. The final $h(i, T)$ had two sets of values, an “on” state and the “off” state. The “on” state was the averaged $h(i, T)$ discussed above. The “off” state was the set of ratios shown in Figure 5.12 that was unique to the zero current. This final version of $h(i, T)$ now represented a highly specialized thermal correction factor. Using this $h(i, T)$, all of the new validation backbone curves should line up on top of the room temperature backbone curve for a given current. Figure 5.16 below shows that this is the case.

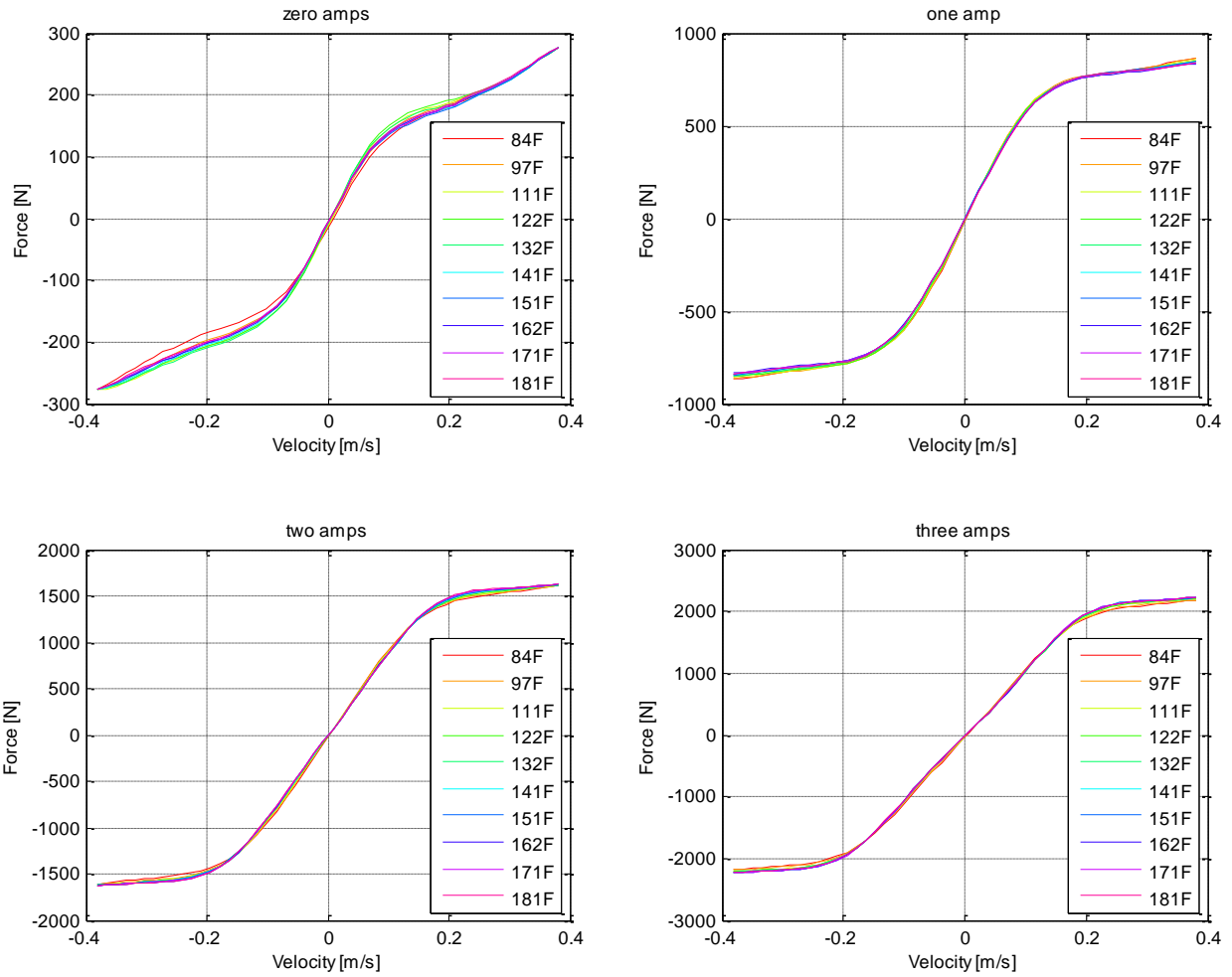


Figure 5.16. validation $h(i, T)$ for all temperatures and all currents

All of these validated backbone curves do line up in a tight group, however they are not perfectly identical. To quantify how closely they match the room temperature backbone curve, a Root Mean Squared Error (RMSE) was calculated for each current and is shown below in Figure 5.17.

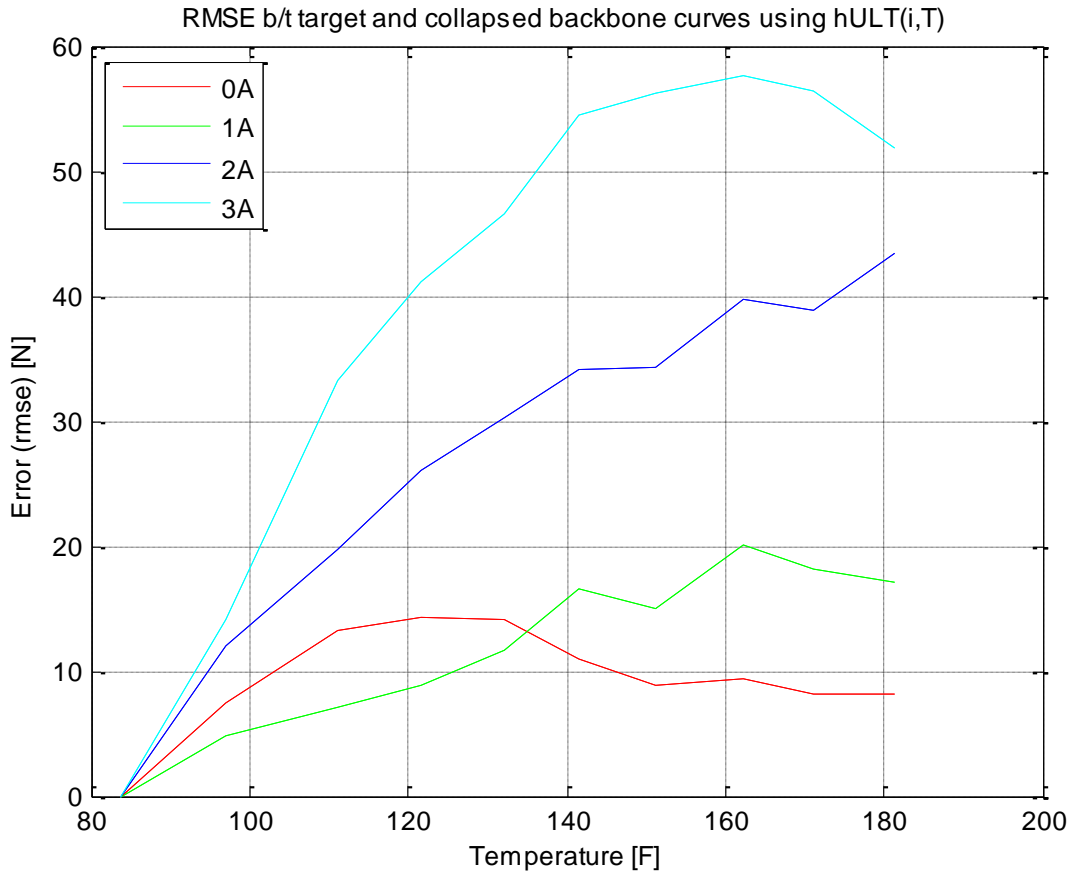


Figure 5.17. RMSE for $h(i, T)$ validation backbone curves

For the “on” state, the general trend is that the error increases with respect to current and temperature. For the “off” state, the error rises to about 15N and then plateaus to around 10N. These errors may seem large, however, Figure 5.18 below shows that they are relatively small compared to the force generated at those conditions.

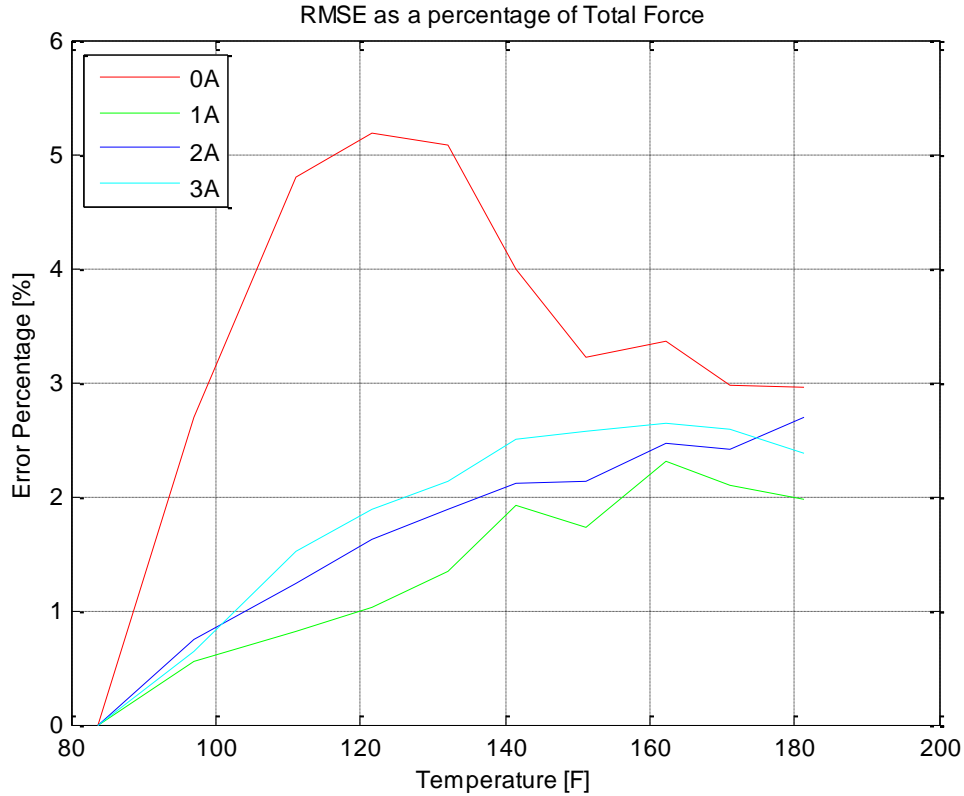


Figure 5.18. RMSE of $h(i, T)$ validation curves as a percentage of total damper force

The RMSE is at or below 3% relative to the total force generated by the damper for the “on” states, and just above 5% for the “off” state. Furthermore, there is a definite difference in performance with and without current. This validates $h(i, T)$ as an acceptable component to represent the temperature characteristics of an MR Damper in the separable model.

5.5) Current Dependent Function: $f(i)$

The current dependence $f(i)$ is the last component of the separable model. It has units of Newtons. It represents the scale factor that transforms $g(v_{rel})$ into the proper force range with respect to the current value at which the damper is operating.

Interestingly, the current dependent component $f(i)$ was already generated in the process of establishing the universal $g(v_{rel})$. The function $f(i)$ was the value used to normalize the collapsed and averaged backbone curve, down to a range of -1 to +1. More specifically, it was the maximum value of the absolute value in the entire collapsed and averaged backbone curve. Figure 5.19 below gives the result of that calculation using the experimental data collected on the MagneRide damper.

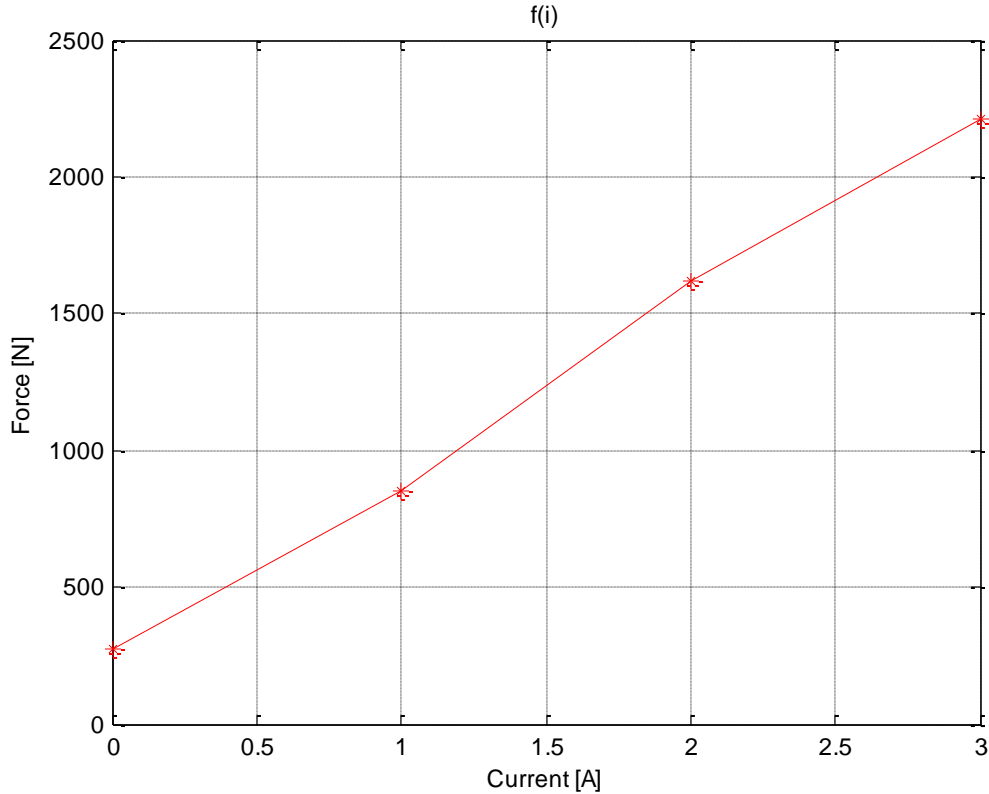


Figure 5.19. Current Dependent Function $f(i)$ is a scale factor with units of Newtons

The function $f(i)$ is simply a scaling factor for each respective current that carries the units of Force. $f(i)$ is neither temperature dependent nor velocity dependent. The temperature dependence was factored out through the scaling factors when the backbone curves were collapsed and averaged. The velocity dependence is completely captured in the universal $g(v_{rel})$ leaving $f(i)$ to purely be a function of current.

5.6) Complete Separable Function

The separable model represented by $F_{back}(i, v_{rel}, T)$ is now completely developed with all three of its components fully defined. The velocity function $g(v_{rel})$ captures the non-dimensional dependence of relative velocity across the shock, including both high speed and low speed damping characteristics. The thermal function $h(i, T)$ captures the non-dimensional temperature dependence of the MR Damper in a simple lookup table for both “on” and “off” states. The current function $f(i)$ fully captures the current dependence of the MagneRide shock and carries the dimensions for force. Together, this represents the non-hysteretic backbone force of the MagneRide damper. Equation 5.2 below defines the complete forward separable model.

$$F_{back}(v_{rel}, i, T) = f(i) \times g(v_{rel}) \times h(i, T) \quad 5.2$$

To verify the accuracy of the separable equation separately from the entire damper model, the forty backbone curves were recreated using the separable model only and compared to the original forty backbone curves extracted from the experimental data. The root mean squared error was taken for each of these forty comparisons and is plotted in Figure 5.20 as both dimensioned values of force and as a percentage of total force.

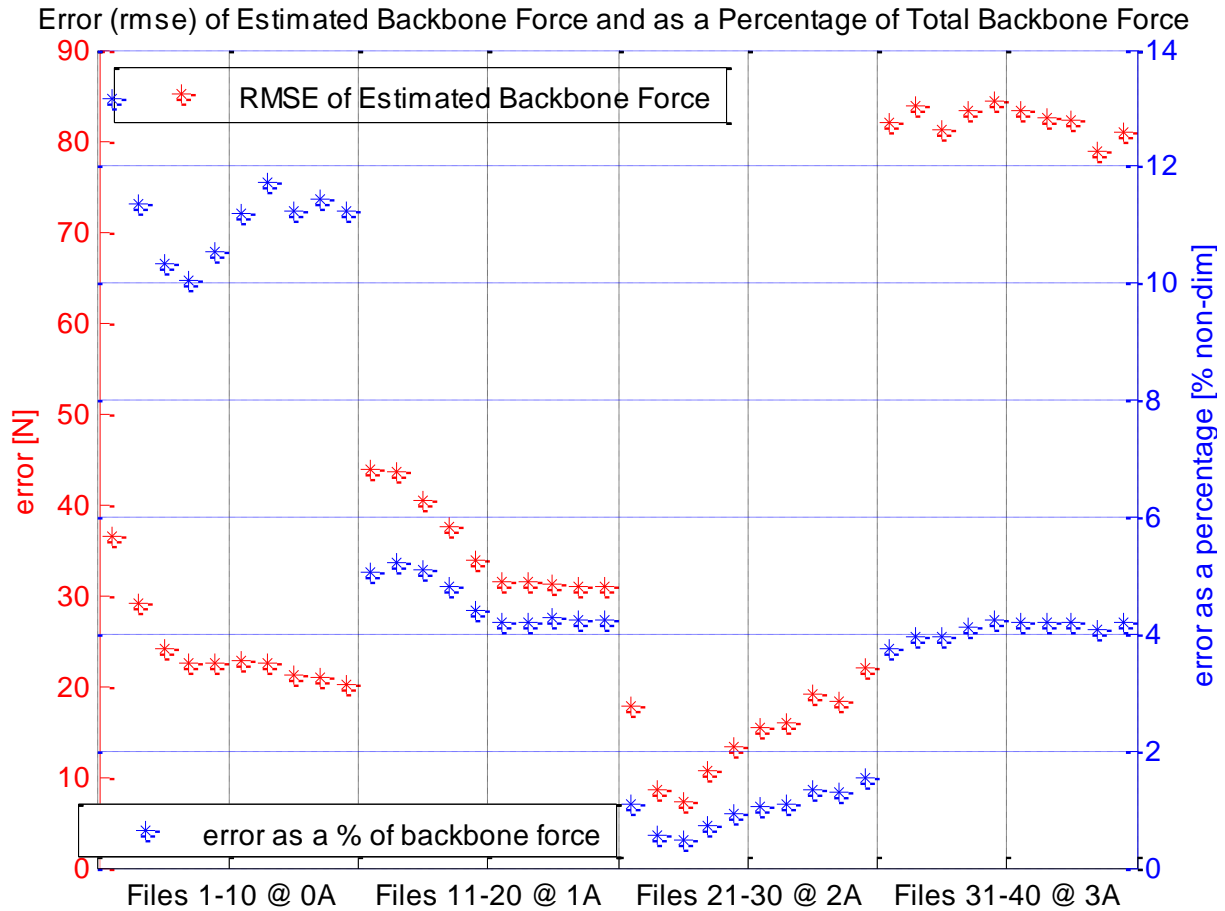


Figure 5.20. Estimated backbone force error in Newtons and as a percentage of total force

The red line in the upper subplot represents the RMSE, while the blue line represents the error as a percentage of the total backbone force for each respective sample. The x-axis of Figure 5.20 deserves explanation. Recall from the original experiment, there were forty runs over four different currents. The figure above is grouped by current, where the first ten files (or experimental runs) correspond to zero current. The next ten files, files eleven through twenty, correspond to the MagneRide damper operating at one amp. This ten group series continues until the three amp operating condition. Looking at the blue line, it is clear that the error is very low across the “on” state, never rising above 5%. Furthermore, the 2 amp group has the lowest error at around 1%. This is because the “universal” components were averages, and those averages were closest to the non-averaged values of 2 amps. Thus there is a bias towards the 2

amp case in this particular realization of the model. Nevertheless, the forward separable model accurately reproduces backbone forces for the “on” state. The “off” state had a greater percentage error ranging between 10% and 13%. This is not surprising given that the derivation of the universal $g(v_{rel})$ component neglected the “off” state. Considering this fact, the separable model returned high-quality results with expected behavioral trends.

6) **Characterization of the Hysteresis Model**

The goal of Hysteresis ID was to identify a linear dynamic system that when placed in series with the backbone function accurately captures the hysteretic behavior of the damper. An additional goal was to determine if the dynamic linear element was temperature dependent. To accomplish this, forty unique hysteresis filters were created, each corresponding to a specific experimental run. The linear dynamic hysteresis filters were implemented as Finite Impulse Response (FIR) filters. FIR filters are linear filters chosen for their unconditional stability. All of their poles lie at the origin and cannot move. Therefore, irrespective of the filter coefficients, the filter is guaranteed to be stable. This is very advantageous because it allows the use of well-known techniques for estimating the coefficients without the concern for stability.

6.1) **Process Structure**

An adaptive filter architecture was used to estimate the FIR filter coefficients[37]. The Least Mean Squared (LMS) update algorithm is a method based on a gradient descent approach [38, 39]. Figure 6.1 below shows the block diagram for this process.

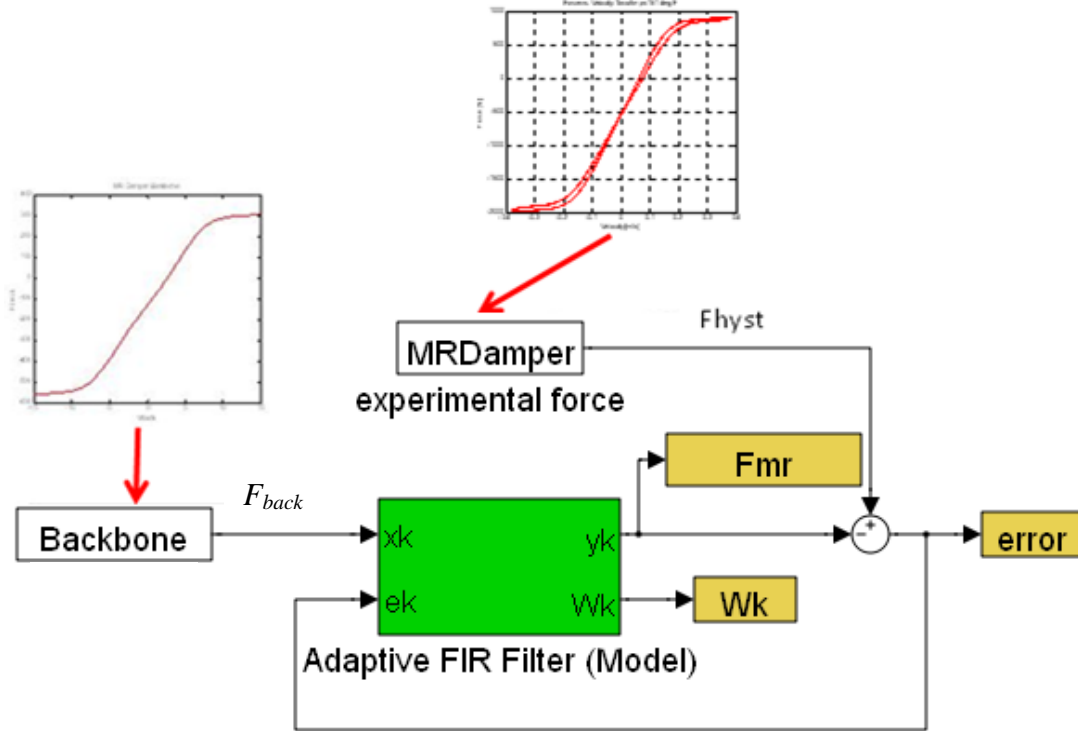


Figure 6.1. Block diagram of the gradient-descent adaptation process which was used to estimate the coefficients of the FIR filter

Here, the backbone force versus time is input to the Adaptive FIR filter block. The target signal was the actual experimental force vs. time data. W_k represents the coefficients of the FIR filter, and the error is the difference between F_{MR} , the force output of the adaptive filter, and F_{hyst} , the target experimental force. This error was used by the adaptation process to update the FIR filter coefficients.

6.2) Adaptation Process

The FIR filter for each current and temperature test case was estimated via an adaptive gradient descent process. Initially the filter weights started at a value of zero, and they changed over a series of iterations until they converged to a final set of values. These values were the coefficients (or weights) that defined the FIR filter. The governing equation that adjusted the filter weights for every iteration was the LMS algorithm seen below [38].

$$\mathbf{W}_{k+1} = \mathbf{W}_k + \mu \varepsilon_k \mathbf{X}_k \quad (6.1)$$

There are four components of the LMS algorithm that help determine the future value of the filter weights \mathbf{W}_{k+1} . These components are the current filter weight value given by \mathbf{W}_k , the error ε_k , the step size μ , and \mathbf{X}_k the backbone force input. The non-hysteretic backbone force \mathbf{X}_k was input through a tapped delay line into the adaptive filter.

$$\mathbf{X}_k = \begin{bmatrix} F_{back}(k) \\ F_{back}(k-1) \\ \vdots \\ \vdots \\ \vdots \end{bmatrix} \quad (6.2)$$

This backbone force was the same backbone force described earlier in Section 5.2. The target force was the experimentally measured dynamic test data $F_{MR}(v_{rel}, i, T)$. The step size μ is a tunable parameter that controls how quickly the algorithm can converge to the final solution on the quadratic performance surface. However, there is a caveat. If the step size is too large the filter weights may not be able to convergence to a low error solution. Conversely, the step size μ can be made smaller, however the number of iterations must increase to compensate, resulting in a slower convergence rate. After a great deal of trial and error tuning, a step size of $1e-9$ accompanied by 3000 iterations was chosen to produce a very reasonable estimate for the final filter design of 500 coefficients.

The reality of a finite step size is a property of the specific adaptation process chosen for the proposed model. Inherent with this architecture is the concept of misadjustment; the fact that a finite step size limits the minimum error achievable [38, 40]. Alternatively, an adaptive step size would be needed to reduce the minimum error limit related to misadjustment. Another assumption which impacts the minimum achievable error is the use of a linear dynamic filter in series with the nonlinear backbone shaping function $F_{back}(v_{rel}, i, T)$ to model the nonlinear dynamics. This assumption separates all of the nonlinear effects into the backbone term $F_{back}(v_{rel}, i, T)$, leaving all of the dynamic effects (i.e. hysteresis) to the linear FIR filter. It will be shown that for this research problem, the advantages of a fixed step size and a stable FIR filter outweigh the disadvantages, and that the two associated errors only had a minor affect on the final model performance.

In order to demonstrate that the FIR filter coefficient estimation process had converged, a mean squared error (MSE) was calculated for each filter to quantify the convergence of the filter weights as well as the minimization of the error. Figure 6.2 below shows that the filter weights had converged for each of the forty test cases because the MSE was no longer decreasing.

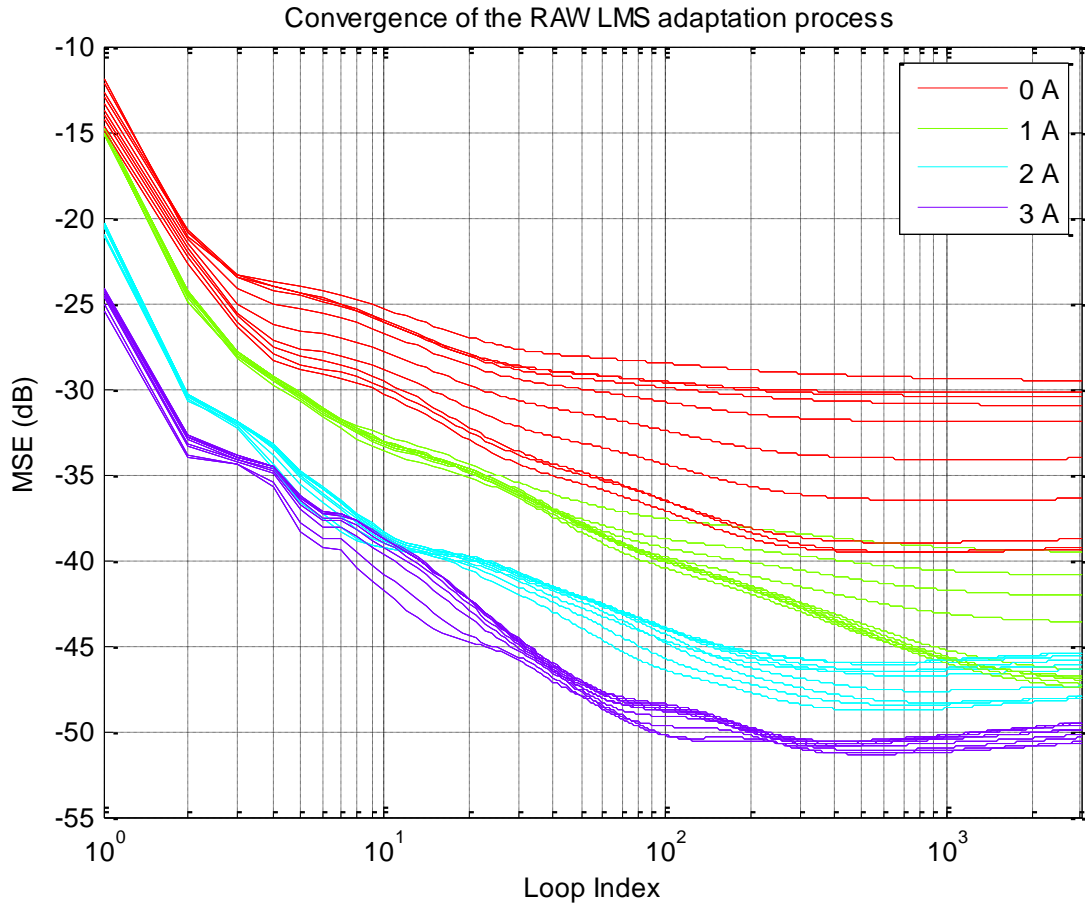


Figure 6.2. Convergence of the adaptive process to a final FIR filter for all 40 test files

The convergence of the filter weights and a significant reduction in the MSE ensured that a unique FIR filter had been created for each temperature at each current. The complex frequency response function (FRF) was calculated for each FIR filter in order to compare the individual frequency responses. Figure 6.3 below shows the frequency response for all forty FRF's. There are ten lines in each plot, corresponding to the ten different experiment temperatures. A legend of temperatures and corresponding colors was not included for this specific figure in order to maximize the visibility of frequency responses. However, the same standard temperature to color scheme from previous backbone plots was implemented in Figure 6.3. An example of this legend is the one found in Figure 5.16.

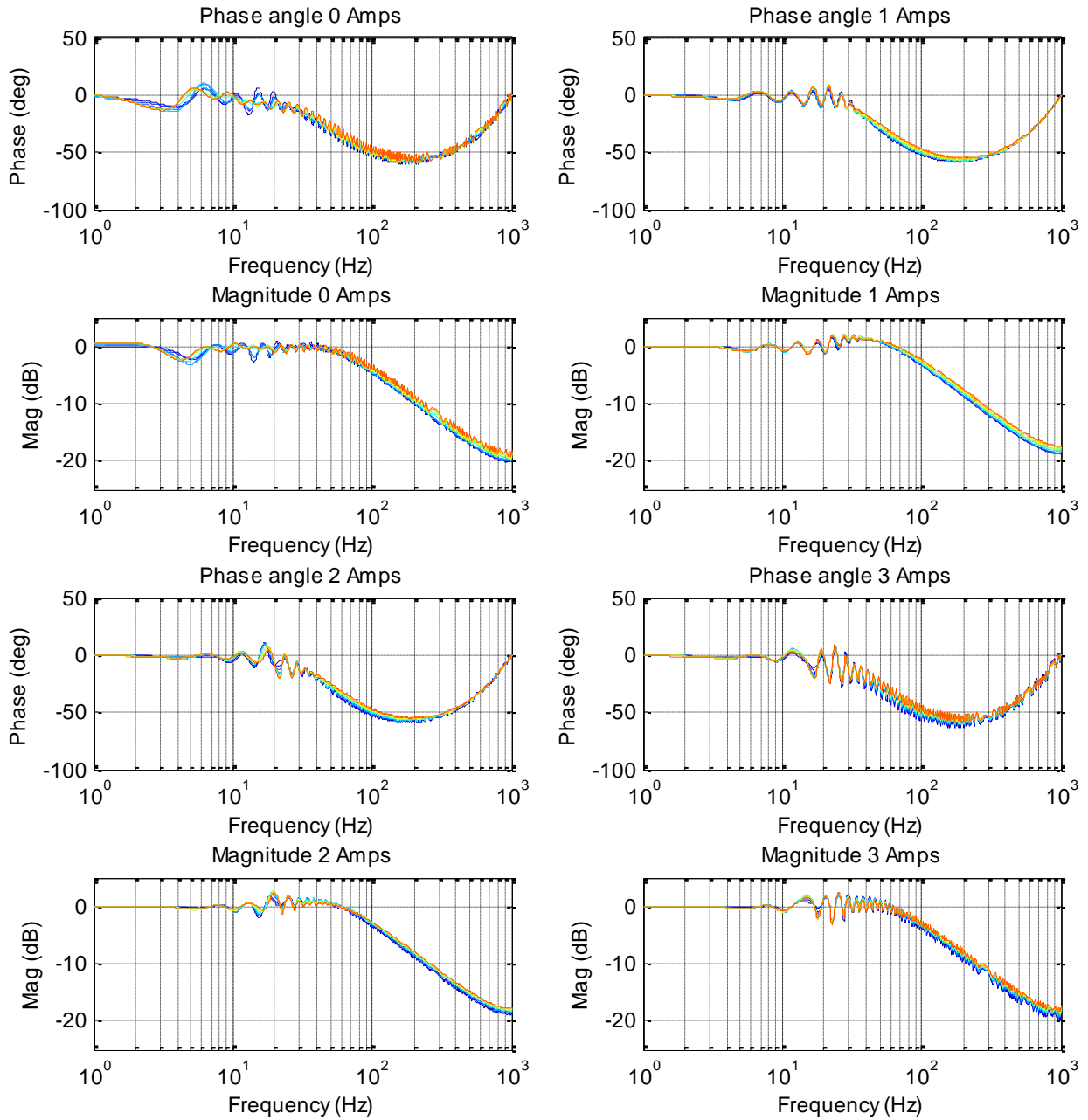


Figure 6.3. Frequency response for all forty FRF's grouped with their respective current
 An alternative way of looking at the frequency response is given in Figure 6.4 below.

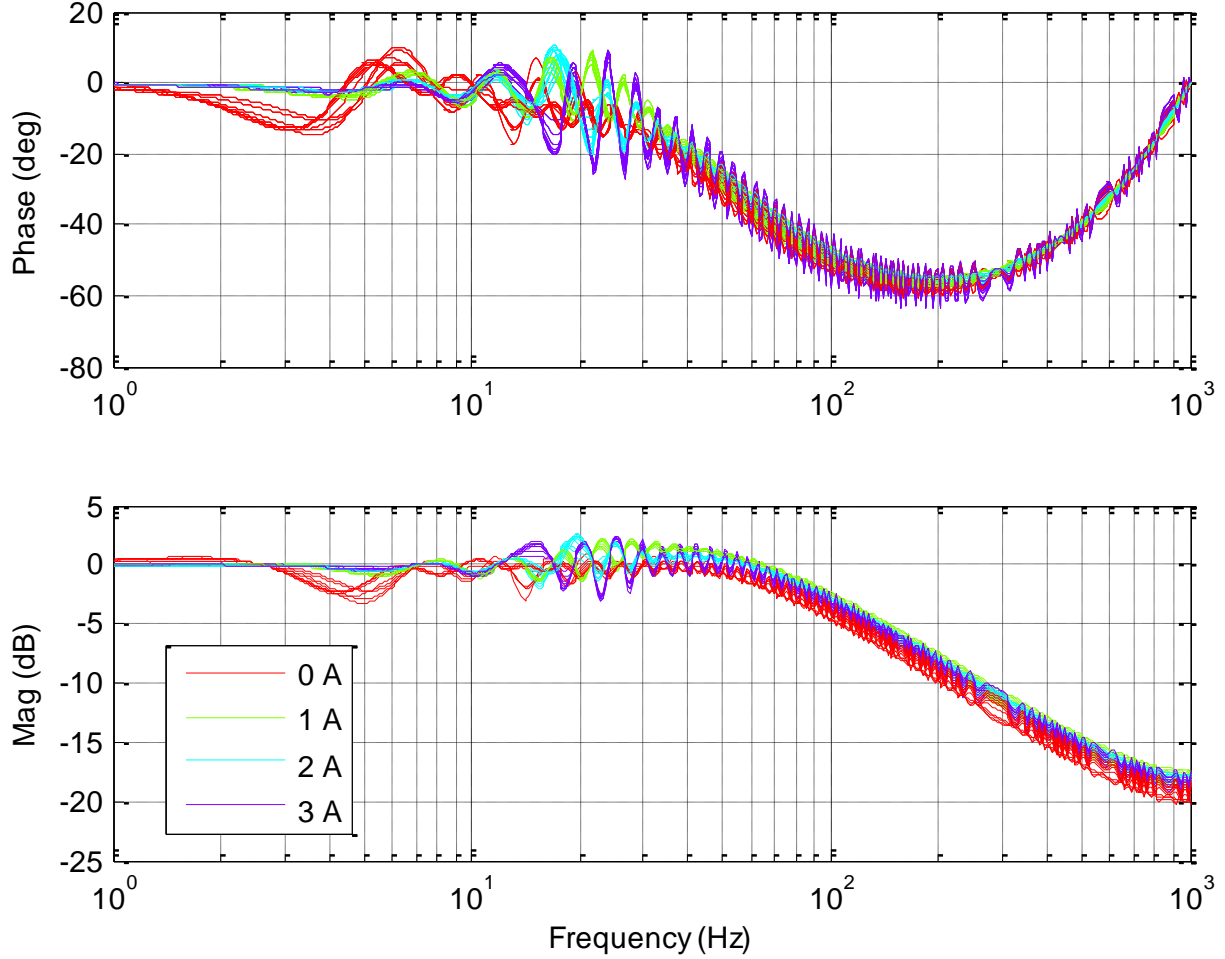


Figure 6.4. Frequency response of all forty Frequency Response Functions of the FIR filters

The filters are grouped by color according to their current. Remarkably, this graph shows that each filter has a very similar frequency response, independent of temperature and current. This result greatly simplifies the overall proposed model in that the hysteretic component can be universal, thus supporting the design objective of minimum complexity while improving the predictive capability. Building upon this observation, a universal hysteretic frequency response function was generated by taking the average of the imaginary and real components of all forty FRF's, and then recombining them using Equation 6.3 below.

$$FRF_{universal} = FRF_{real_{avg}} + j \times FRF_{imaginary_{avg}} \quad (6.3)$$

Using the universal (averaged) frequency response function, a low order IIR filter $H_{IIR Universal}$ was curve fit to the magnitude and phase response of $FRF_{universal}$. This approximated IIR filter is 3rd order while the FIR is 500th order. The transfer function of $H_{IIR Universal}$ is shown below in Equation 6.4.

$$H_{IIR\ Universal}(z) = \frac{0.2166z^2 - 0.4128z + 0.1964}{z^3 - 2.738z^2 - 0.7604} \quad (6.4)$$

For comparison to the results of the Reader model [1, 3], a simple 1st order low-pass filter was also fitted to $FRF_{universal}$.

$$H_{LPF}(s) = \frac{F_{MR}}{F_{static}} = \frac{a}{s + a} \quad (6.5)$$

These two filters were created to investigate the potential performance gains or losses associated with a simpler approximation to the universal FIR filter. Figure 6.5 below illustrates the frequency response of the three “averaged” filters.

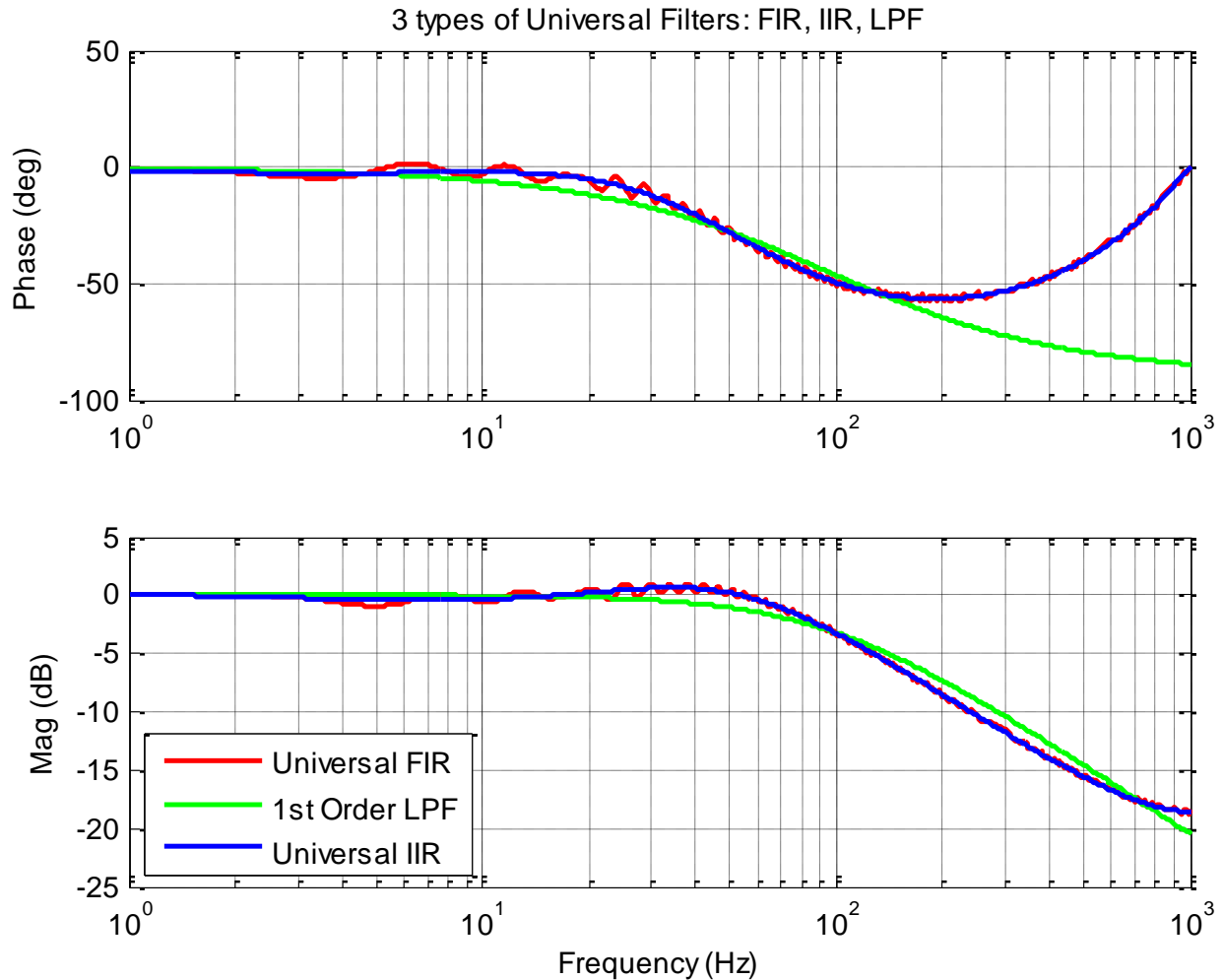


Figure 6.5. Frequency Response Functions of three universal filters: FIR, IIR, LPF

The red curve is the universal FRF of the FIR filters, the blue curve is the IIR fit, and the green curve is a 1st order low-pass filter approximation. The LPF does not match the FIR filter’s phase

back up to zero at high frequency; however, the positive results obtained by Reader [1, 3], suggests that this may not be an important feature. The IIR filter however is an excellent lower order approximation to the FIR.

7) Forward Model Validation

To validate the universal IIR hysteretic filter, the entire forward model was used, and as a result, validated as well. Figure 7.1 below shows the final forward MR Damper model.

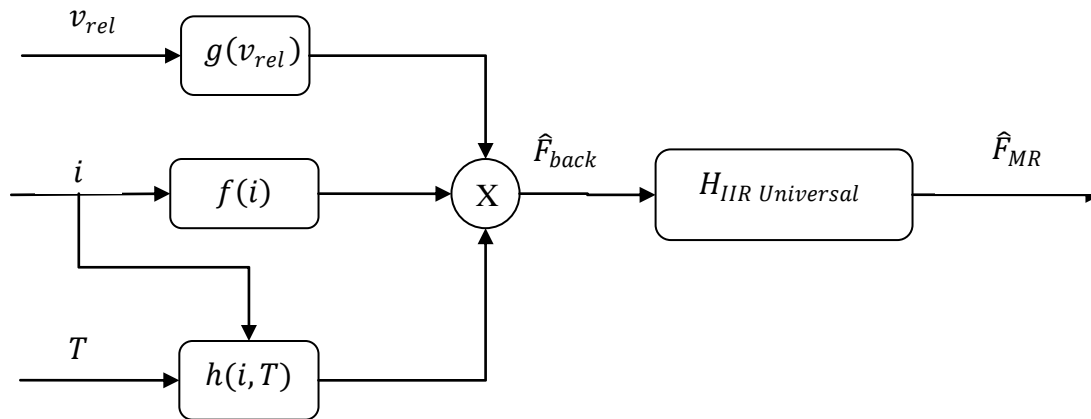


Figure 7.1. Forward Model: nonlinear backbone model elements multiplied on the left are fed through the universal hysteretic filter to generate a complete MR damper force

The three inputs to the separable model are velocity, temperature and current. These signals are passed through the appropriate functions where the terms are multiplied together to generate the backbone force output. This backbone force is passed into the Hysteresis filter. Three categories of filters were used for the validation study. The first category was the Universal IIR filter seen in Figure 7.1 above. The second type of hysteresis filter was a 1st order LPF approximation inspired by Reader’s work[3]. The third category was a matrix containing all forty unique FIR filters. These unique FIR filters represented the “best” hysteresis model because each was custom tailored for one of the original corresponding experimental test runs. This comparison gave the ability to quantify the effect all three categories of hysteresis filters on overall model performance. The model errors for each category of hysteresis filter are shown in Figure 7.2 and Figure 7.3 below

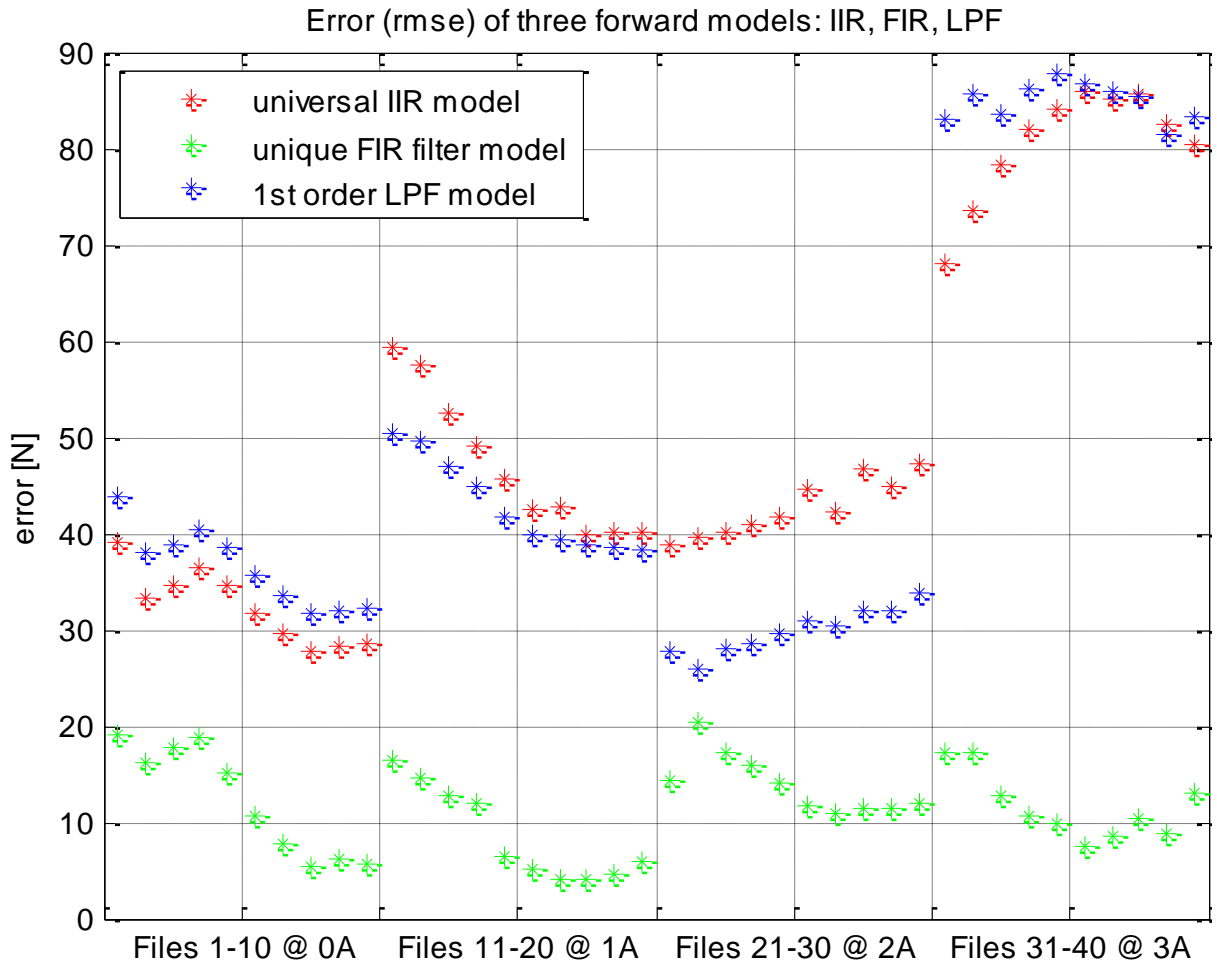


Figure 7.2. RMSE of universal IIR filter vs. the unique FIR filters

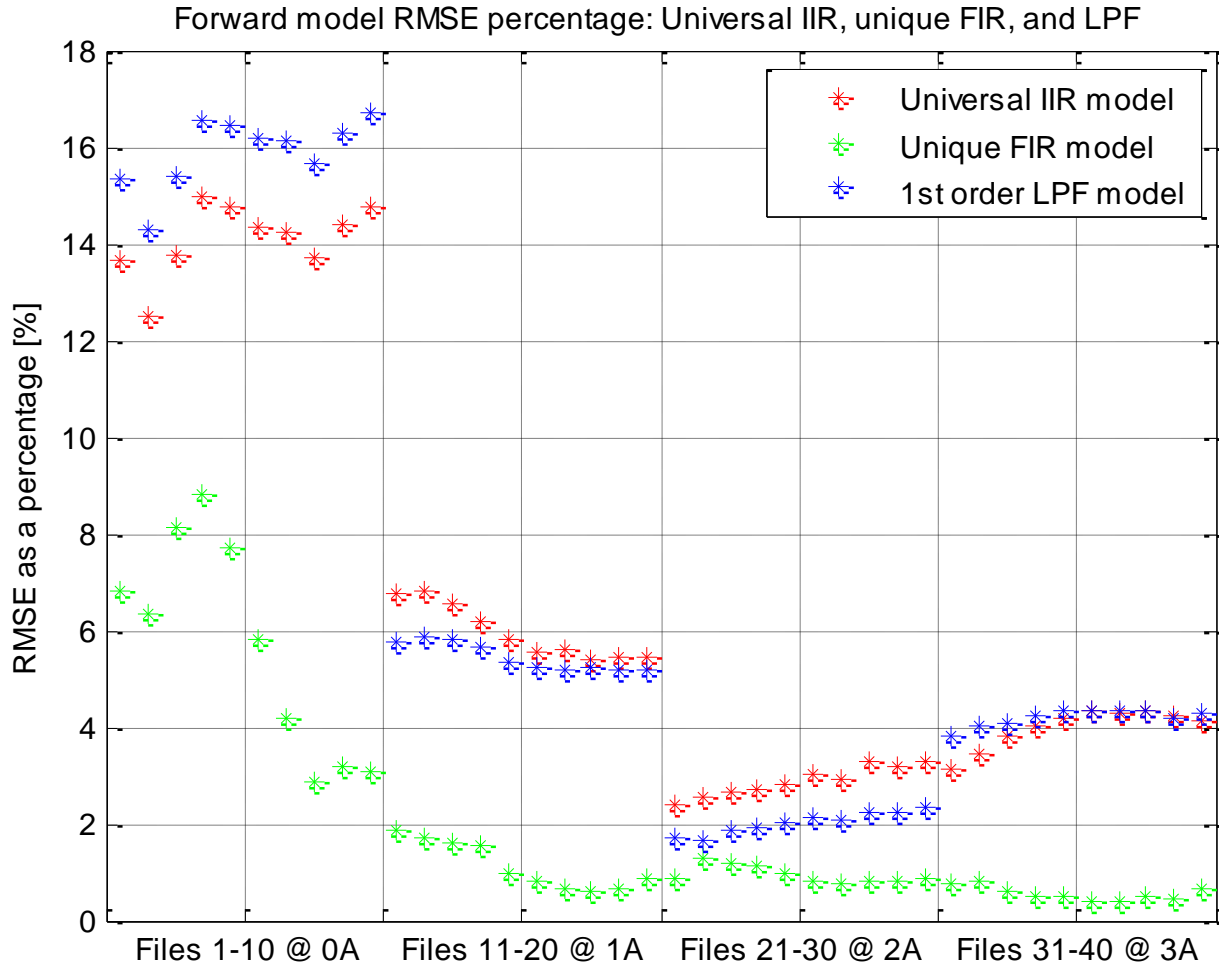


Figure 7.3. Error as a percentage of total force: universal IIR model vs. unique FIR model

For all three sets of data shown in Figure 7.2 and Figure 7.3 above, the error was calculated with respect to the experimental data signals recorded during the original experiment. Looking at both graphs, it is clear that the lowest error is achieved using the set of unique FIR hysteresis filters. However, the forward model employing the universal IIR filter also performed exceptionally well. For the “on” state, the error was between 2% and 7%, while the “off” state ranged between 12% and 15%. Not only is the universal IIR filter robust, it is low order and independent of temperature and current. Furthermore, this total model error confirms our hypothesis that a linear hysteretic filter cannot completely compensate for all the dynamics in a nonlinear system; however it can come very close for this particular damper. The low-pass filter did a good job of approximating the hysteresis as well. It performed minimally better than the IIR filter at one and two amps, while worse at the zero and three amp case. Whether it is better than the universal IIR is inconclusive from these graphs, however, for the proposed model, the universal IIR filter was the chosen filter for model implementation.

8) Inversion of the Forward Model

To implement the findings of the proposed model in a real-time controller, an inverse model has to be created that can take the desired control force and calculate the corresponding command current necessary for the MR Damper. An accurate determination of the command current signal allows the MR Damper to actually produce a force that better matches the desired force. Figure 8.1 below gives a block diagram of where this inverse model fits in relation to the rest of the suspension system based on a Skyhook control law. Please note that the inverse model can benefit several types of control laws of which is Skyhook is only an example and is used for illustration purposes only.

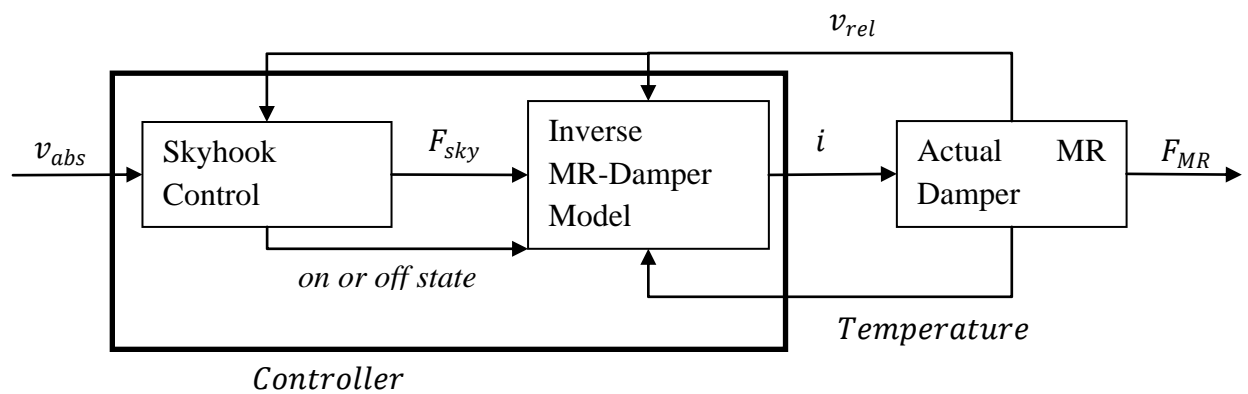


Figure 8.1. Example suspension control system employing an Inverse MR Damper model

The inverse model accounts for the nonlinearities and variations in the MR Damper's performance related to temperature, current, velocity, and hysteresis. The inverse model accepts the desired damper force from a control algorithm such as Skyhook, and generates an appropriate output current. This current enables the actual MR damper to produce a force that better matches F_{sky} for that specific velocity and temperature condition.

To create the inverse MR Damper model, the proposed forward model was essentially rearranged to function in reverse. However, before the details of this manipulation can be given, the fundamental design requirements of this inverse model need to be addressed. Figure 8.2 depicts the inverse model highlighted by a green dashed box, in series with the proposed forward model. The format of this block diagram is deliberate because it recognizes two principal regions: a non-hysteretic region marked in red and a dynamic region marked in blue. Looking at the non-hysteretic region, in order for the block labeled "*Inv Eqn 5.2*" to be the inverse of the block labeled "*Eqn 5.2*", the combination of the two should equal 1. This should also result in the two backbone forces, \hat{F}_{back} and F_{back} , being equal. If these criteria are satisfied, then the non-hysteretic portion of the block diagram is considered to have a true forward component and

inverse model component. Taking this same approach to the dynamic region marked in blue, the inverse and forward hysteresis filters, H_{IIR}^{-1} and H_{IIR} respectively, should be associated with the ability to generate dynamically rich force signals that are equal to each other, specifically, F_{des} and F_{MR} . A correctly designed inverse model will make the entire blue box equal to 1 if all of its elements are combined.

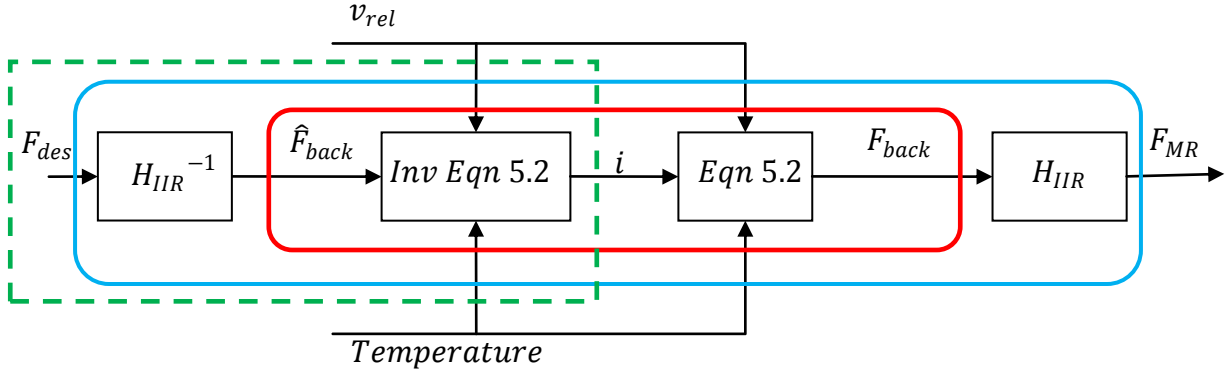


Figure 8.2. Inverse MR Damper model cascaded with forward model

Equation 8.1 below explicitly details the governing equation of the inverse model. The inputs are relative velocity, current (on or off state distinction only), temperature, and desired force. The output is the commanded current signal to the actual MR Damper, which is equivalent to the improved command signal output from the NLDIM.

$$i = f^{-1} \left(\left(\frac{1}{g(v_{rel}) \times h(i, T)} \right) \times H(z)_{IIR\ Universal}^{-1} [F_{des}] \right) \quad (8.1)$$

On the right-hand side of the equation, there is an overreaching function f^{-1} that is essentially the inverse of the $f(i)$ curve from the forward model. It is a look up table and is shown below in Figure 8.3.

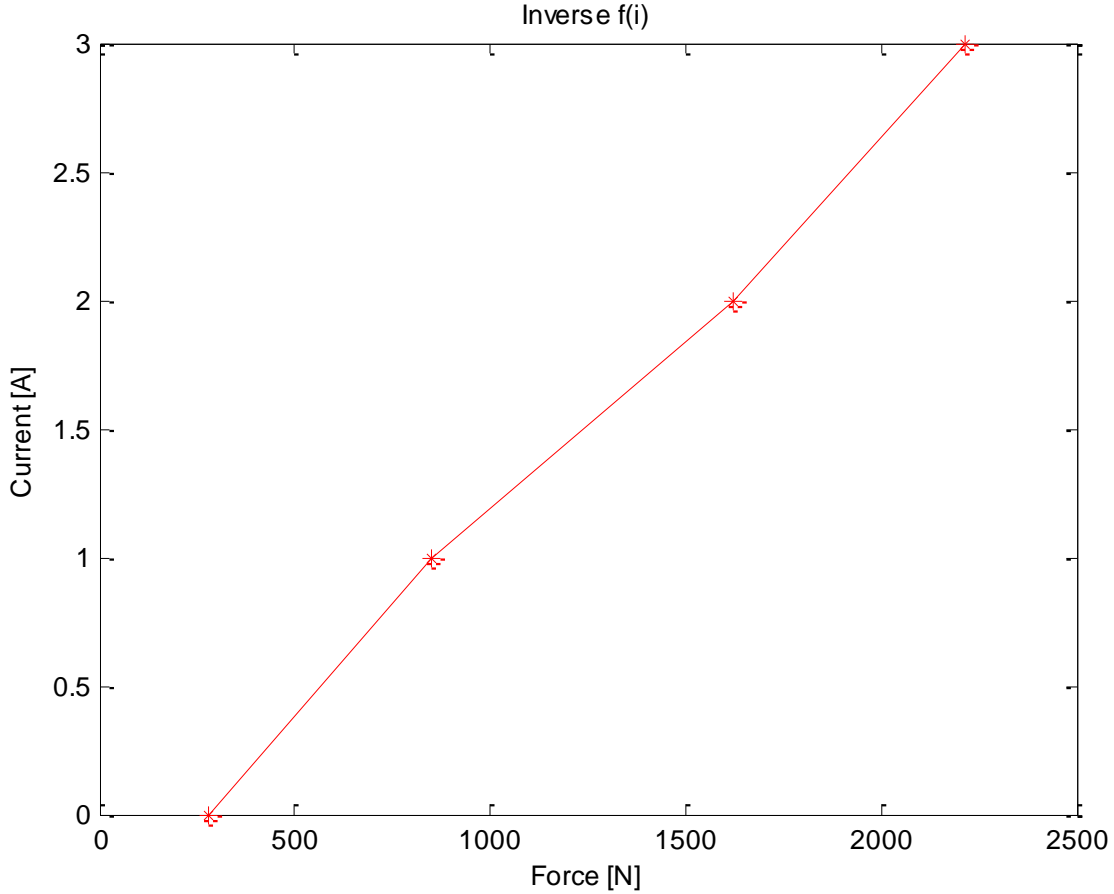


Figure 8.3. Inverse $f(i)$

The force is now in the x-axis, and the output current is the y-axis. The force does not start at zero force, recognizing the passive damper force at zero current. Furthermore, there is an asymptote at higher currents, representing the damper's ability to only recognize a maximal amount of force, irrespective of the associated current.

Specific to f^{-1} , is its ability to only processes non-dynamic input signals. This corresponds to an additional prerequisite of invertibility that requires $f(i)$ in the proposed forward model to be strictly monotonic. The inputs to f^{-1} successfully satisfy these conditions by being non-dimensional constants and non-hysteretic force signals. The quotient containing the velocity and temperature correction factors $\left(\frac{1}{g(v_{rel}) \times h(i, T)}\right)$ produces a single valued constant that serves as a scaling factor; there are no dynamics present. Furthermore, the determination of the velocity dependent term $g(v_{rel})$ and the temperature correction factor $h(i, T)$ are identical to the forward model. The only difference now is that they are a divisor because the equation represents an inverse model. The static force represented by $H(z)_{IIR\ Universal}^{-1} [F_{des}]$ removes the dynamics from the desired control force by using an inverse hysteresis filter $H(z)_{IIR\ Universal}^{-1}$. This

inverse hysteresis filter was a new development for the inverse MR Damper model. Its development is given in more detail in the following section.

8.1) **Generation of the Inverse Hysteresis Model: $Hyst_{IIR\ Universal}^{-1}$**

Following the development in Reader's work[3], the inverse hysteresis filter is nominally the dynamic inverse of the Universal 3rd order IIR filter discussed in Chapter 6. The final version of the forward model hysteresis filter had two zeros and 3 poles; with two of poles being one pair of complex conjugate poles. Strict inversion of this transfer function would result in a non-proper transfer function. As a starting point for inverting the hysteresis transfer function, only the complex pole pair and the two real zeros of the forward model were swapped. The original real pole remained a pole in the inverse. From there, loop shaping was performed to manually tune the filter frequencies and damping coefficients of the inverse filter until the combined system response was satisfactory. The combined response specifically refers to the resulting frequency response from the multiplication of the forward and inverse dynamic transfer functions. Equation 8.2 and 8.3 below gives the inverse hysteresis filter in continuous and discrete time formulations.

$$H(s)_{IIR\ Universal}^{-1} = \frac{7.5800s^2 + 42620000s + 9723000000}{s^3 + 11910s^2 + 37100000s + 9723000000} \quad (8.2)$$

$$H(z)_{IIR\ Universal}^{-1} = \frac{3.375z^3 - 2.455z^2 - 3.281z + 2.549}{z^3 - 0.4968z^2 - .2855z + 0.02928} \quad (8.3)$$

The discrete time formulation was generated using the Tustin method; this added a zero to the transfer function. Below, in Figure 8.4, the forward, inverse and combined hysteresis filter frequency responses are shown.

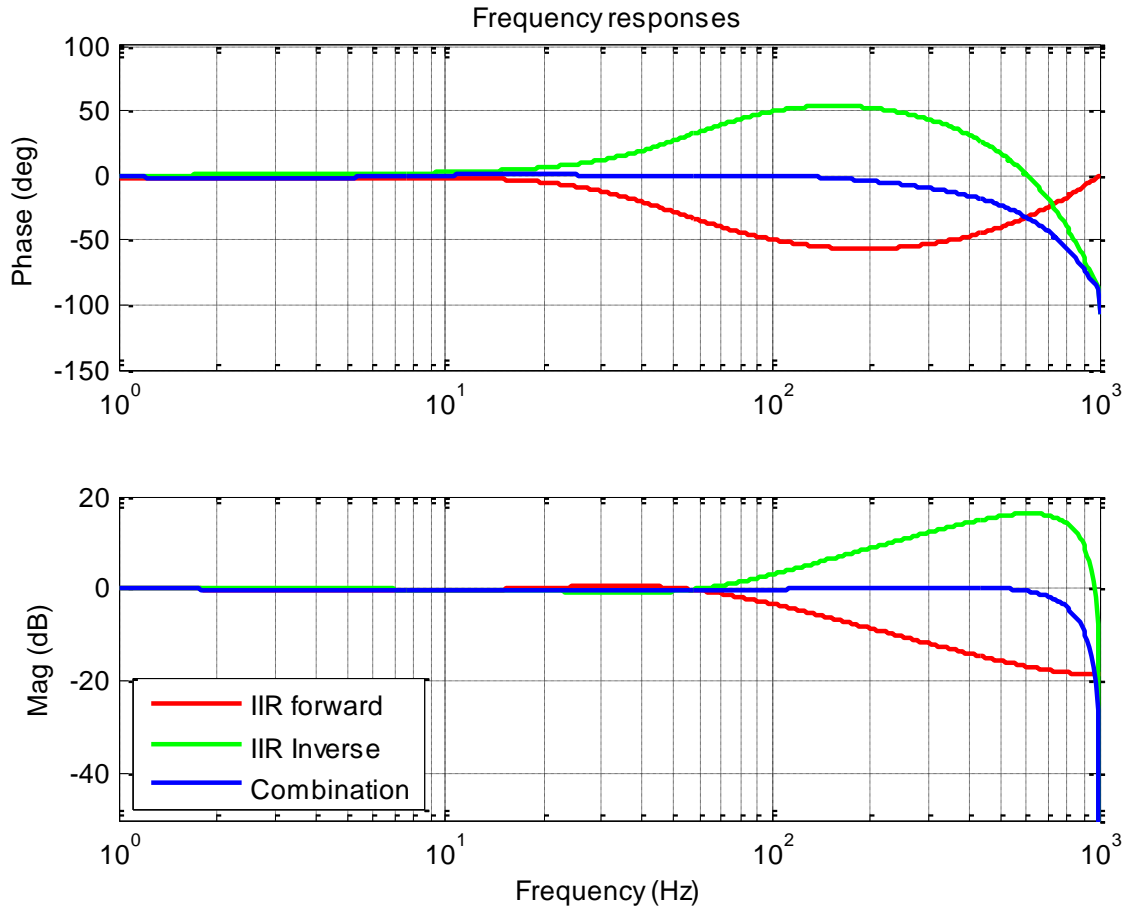


Figure 8.4. Forward, Inverse, and Combined hysteresis filter frequency responses

The target for the combined filter frequency response was to have minimal phase shift and minimum magnitude change over the target bandwidth. The primary bandwidth of interest was 0 to 20 Hz and the blue curve clearly meets this target performance criterion. For higher frequencies, the inverse filter (green line) was tuned to be as true of an inverse of the forward filter (red line) as possible because the Butterworth low pass filter detailed in Section 5.1 has a roll-off and not a finite cut-off at its break frequency. Interestingly, work by Emmons shows that most race dampers have diminished damping capabilities above 100Hz [41]. The spectrum from the MR Damper data in this work was not broad enough to validate anything outside the target bandwidth, however it can be speculated that the response at higher frequencies may not have as much significance relative to the lower frequencies. Lastly, nearing the nyquist frequency of 1000Hz, the inverse filter was tuned so that the magnitude is allowed to roll off, similar to a low-pass filter. Hence, the frequencies and damping coefficients of the inverse transfer function were adjusted accordingly until the combined frequency response looked satisfactory.

9) Verification Study through Simulation

9.1) Validation Overview

To validate the proposed model, two simulations were conducted. The first simulation was a verification that quantitatively measured if the proposed inverse model did indeed satisfy its intended purpose. This was to successfully generate a command current from a dynamically rich damper force signal. The second simulation studied the ability of the proposed forward model to estimate the force output from an industry standard Spencer model. This second validation measured the performance capability of the proposed model on a damper that was different from the MagneRide used in the original experiments.

9.2) MagneRide Verification

The first verification to test the accuracy of the inverse model was a simulation shown in Figure 9.1 below.

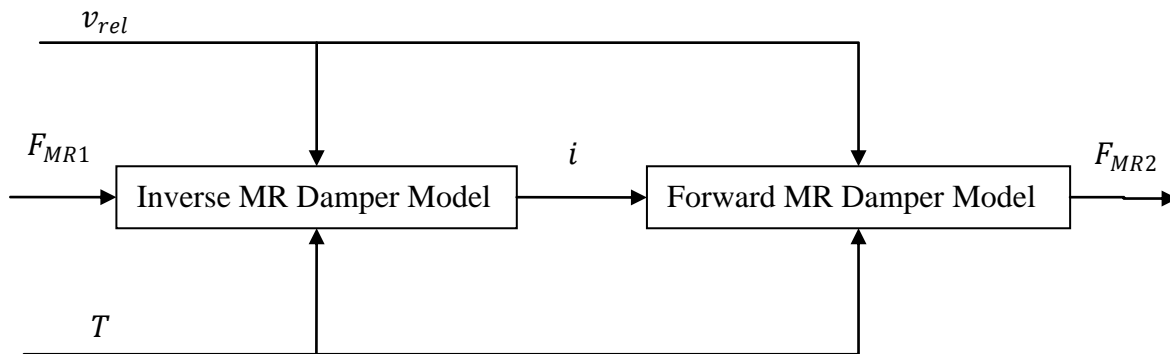


Figure 9.1. Simulation study for verifying the MagneRide inverse MR damper model

The layout is simply the proposed inverse model followed by the proposed forward model. It is identical to Figure 8.2 from the previous chapter. A sample file from the initial experiment on the MagneRide Damper that contained the dynamic force, velocity, and temperature, was chosen and fed into the inverse model. The inverse model used these inputs to generate a unique current which was fed into the forward model. The forward model then produced a hysteretic damper force. The goal was to have the output signal F_{MR2} to match the commanded input signal F_{MR1} . Figure 9.2, Figure 9.3 and Figure 9.4 below show the results of a sample taken at 3 Amps and 132°F.

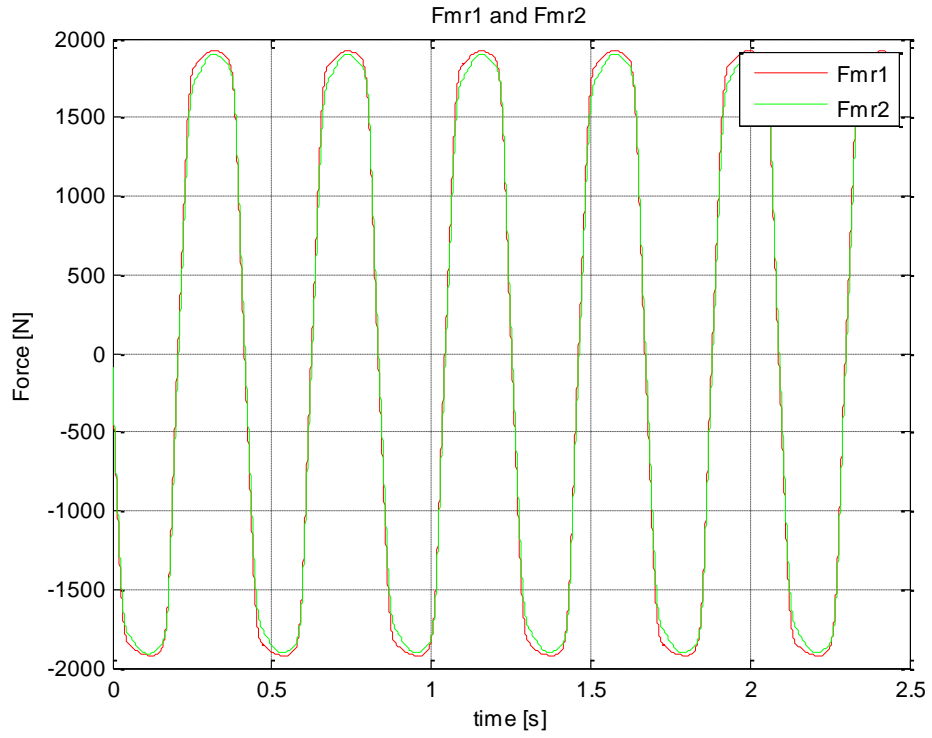


Figure 9.2. Force versus time signals for F_{MR1} and F_{MR2}

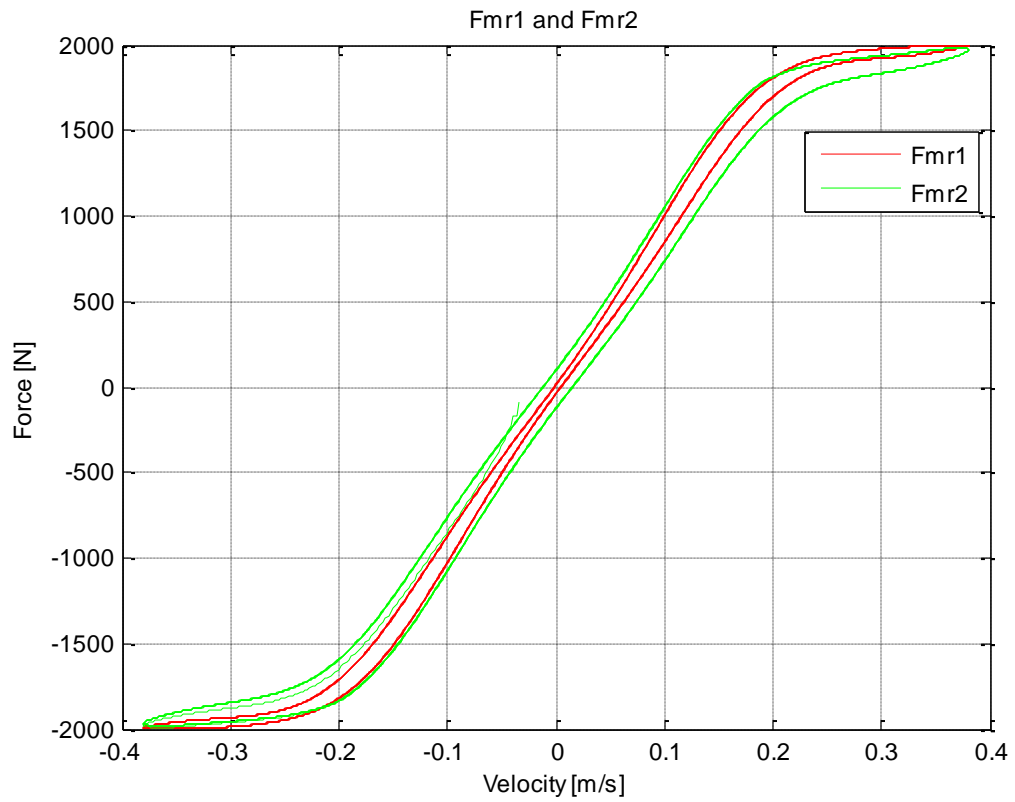


Figure 9.3. Force versus velocity for F_{MR1} and F_{MR2}

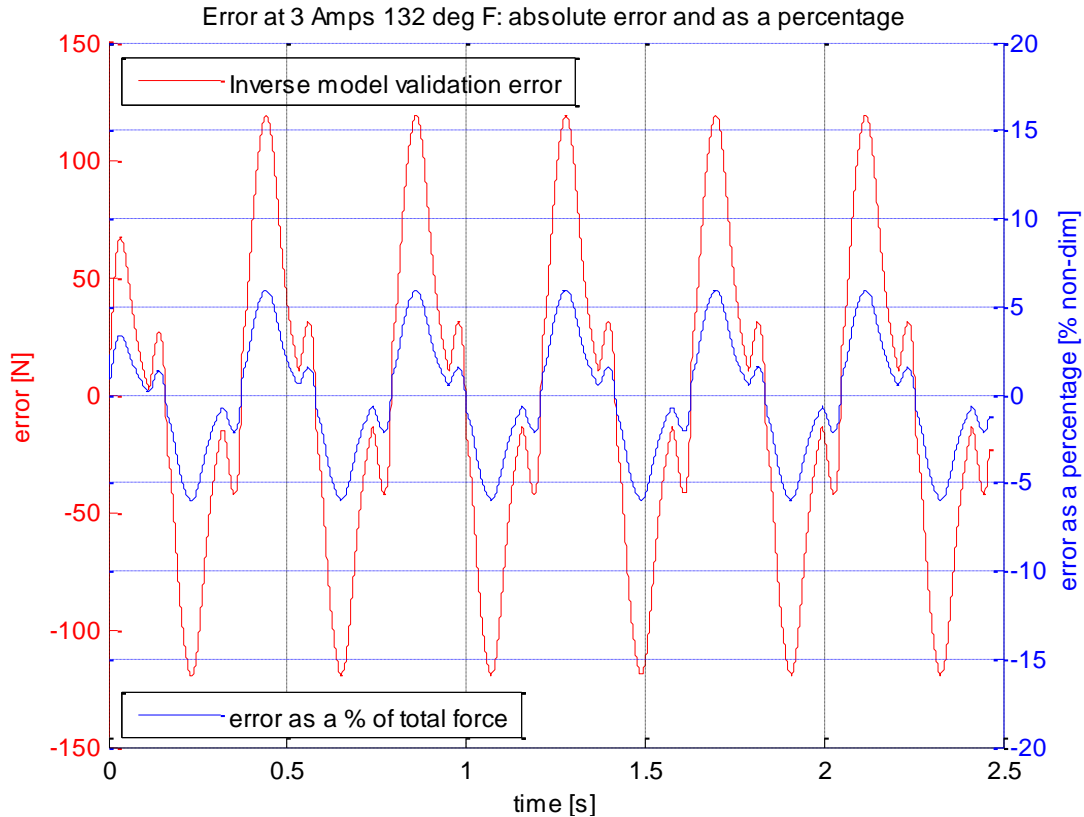


Figure 9.4. Inverse mirror image validation error for 3A 132^oF

In Figure 9.2 and Figure 9.3 the two signals F_{MR1} and F_{MR2} appear to match up reasonably well. Taking a closer look at the difference between the two time based force signals, Figure 9.4 gives the error between the two. There are two lines, the one in red is the raw error between F_{MR1} and F_{MR2} , while the blue curve represents the error as a percentage of the total force the MagneRide damper produced for that run. It can be seen that the overall error stays under 6%. This is an indication of good performance because the error is low, however, it is only one sample. To see the full error performance for this validation study, all forty experiments need to be considered.

In order to ensure that this validation was robust, the force from all forty of the original experimental runs were separately sent through the MagneRide verification as F_{MR1} . The resulting F_{MR2} was generated for each of the forty test cases, and the RMSE was calculated. The raw numerical RMSE is given below in Figure 9.5 as well as the RMSE as a percentage of the total force produced.

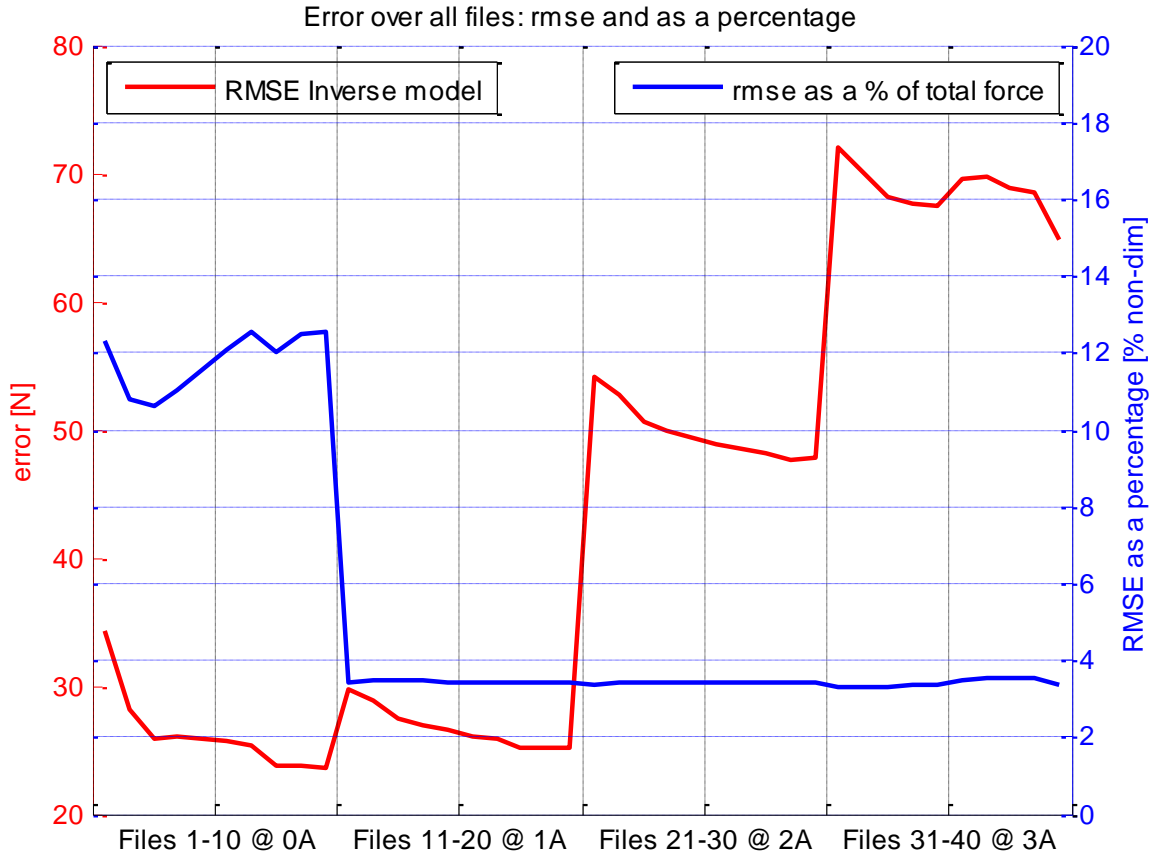


Figure 9.5. RMSE for inverse model cascaded with forward model validation simulation

Figure 9.5 shows that the inverse model is in fact robust. For the “on” state, the rmse as a percentage of total force produced by the damper tracked at a solid 3.5%, which is excellent. The “off” state was higher at around 12%. One of the reasons for this higher error is the bias of the $g(v_{rel})$ term towards the “on” state.

Another interesting performance observation is tracking the current command signal generated by the proposed inverse model. Below two figures are given, Figure 9.6 shows the error tracking for a single sample of 2 Amps at 141^oF, while Figure 9.7 shows the average current value per run for all forty samples.

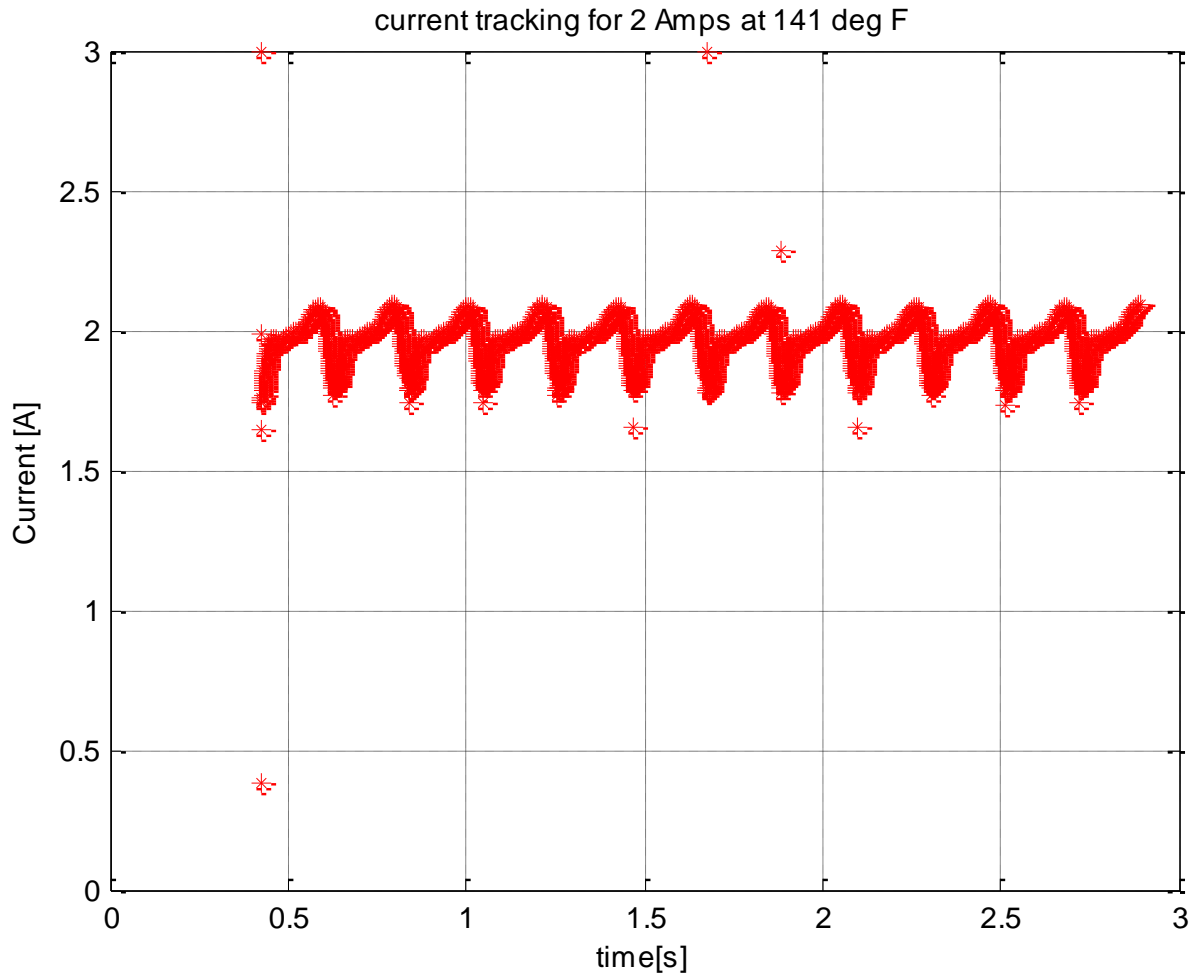


Figure 9.6. Current tracking for 2 Amps at 141 degrees F

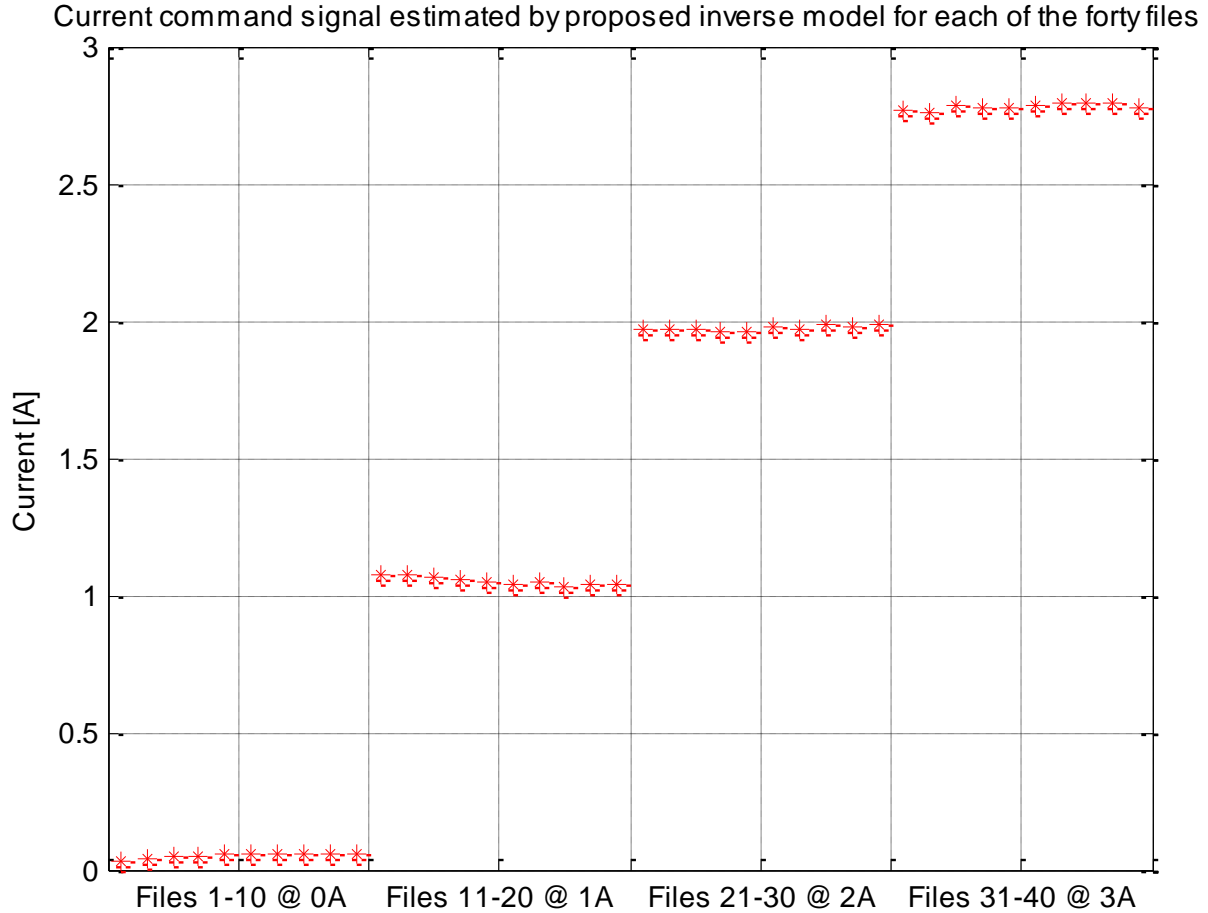


Figure 9.7. Tracking the current generated by the inverse model for all forty files

Figure 9.6 shows that the current tracks well for the 2 Amp sample, staying relatively close to the target of 2 amps. The small spikes in the time series occur when the $g(v_{rel})$ term approaches zero velocity in Equation 8.1, causing the denominator to become very small. However, the proposed model is built to compensate for this; evidence of this fact is low error values in Figure 9.4 and Figure 9.5. Figure 9.7 above shows that the inverse model did in fact successfully generate appropriate current signals that correspond to the actual test scenarios. There is a clear distinction between each grouping of currents at zero, one, two and three amps. This supports the ability of the proposed inverse model to accurately generate the proper current from the associated desired command force.

9.3) Spencer Validation

To further validate the proposed model, a Spencer model was used for comparison [7]. Clearly, the Spencer model parameterization is not associated with the MagneRide damper used in this study, so a series of simulation experiments were performed to characterize the Spencer model using the proposed empirical model. The force output from the Spencer damper model was treated as the target performance signal. This target signal was the force versus time signal that

the proposed model would be trying to accurately estimate. Equations 9.1 through 9.3 describe the Spencer model[7].

$$\dot{y} = \frac{1}{c_0 + c_1} [\alpha z + c_0 \dot{x} + k_0(x - y)] \quad (9.1)$$

$$\dot{z} = -\gamma|\dot{x} - \dot{y}|z|z|^{n-1} - \beta(\dot{x} - \dot{y})|z|^n + A(\dot{x} - \dot{y}) \quad (9.2)$$

$$F = c_1\dot{y} + k_1(x - x_0) \quad (9.3)$$

The coefficients of the model are parametric and are unique to the MR Damper modeled in Spencer's experiment [7]. For simplicity, that specific damper and associated coefficients were used. Additionally, this decision provided the opportunity for our model to be tested with an MR Damper that is different from what it was developed with.

To simulate the Spencer model, a simulation of the above equations was created in Simulink. Figure 9.8 below illustrates the simulation.

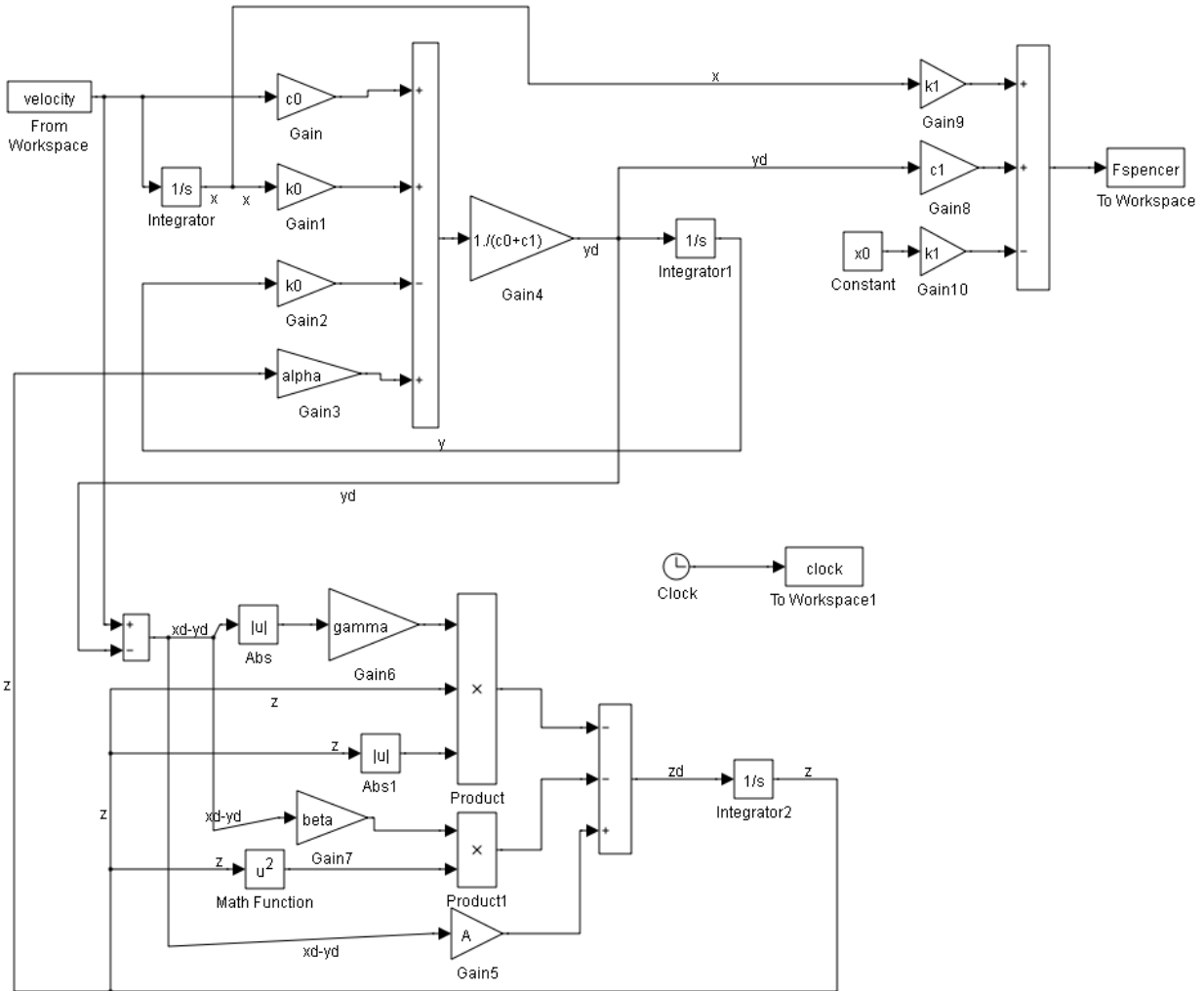


Figure 9.8. Simulink Illustration of Spencer Model

A Dormand-Prince ode-45 solver was used with a variable step size. The input to the simulation was the sinusoidal velocity signal described in Equation 9.4 below. This velocity was in units of centimeters per second, however, the way the Spencer model is formulated, a damper force in Newtons was produced[7].

$$velocity = 12\pi\cos(5\pi t) \quad (9.4)$$

The Spencer model simulation generated a dynamic force signal that corresponded to the velocity signal in Equation 9.4. This force and velocity pair, represented a simulated Spencer damper. Next, the proposed MR damper model was “fit” to this Spencer damper through the characterization process described in Chapters 5 and 6. Once the characterization was complete, the Spencer simulation force and proposed model force were compared for a given velocity and current. The resulting force generated by the proposed model is shown below along with the target Spencer force.

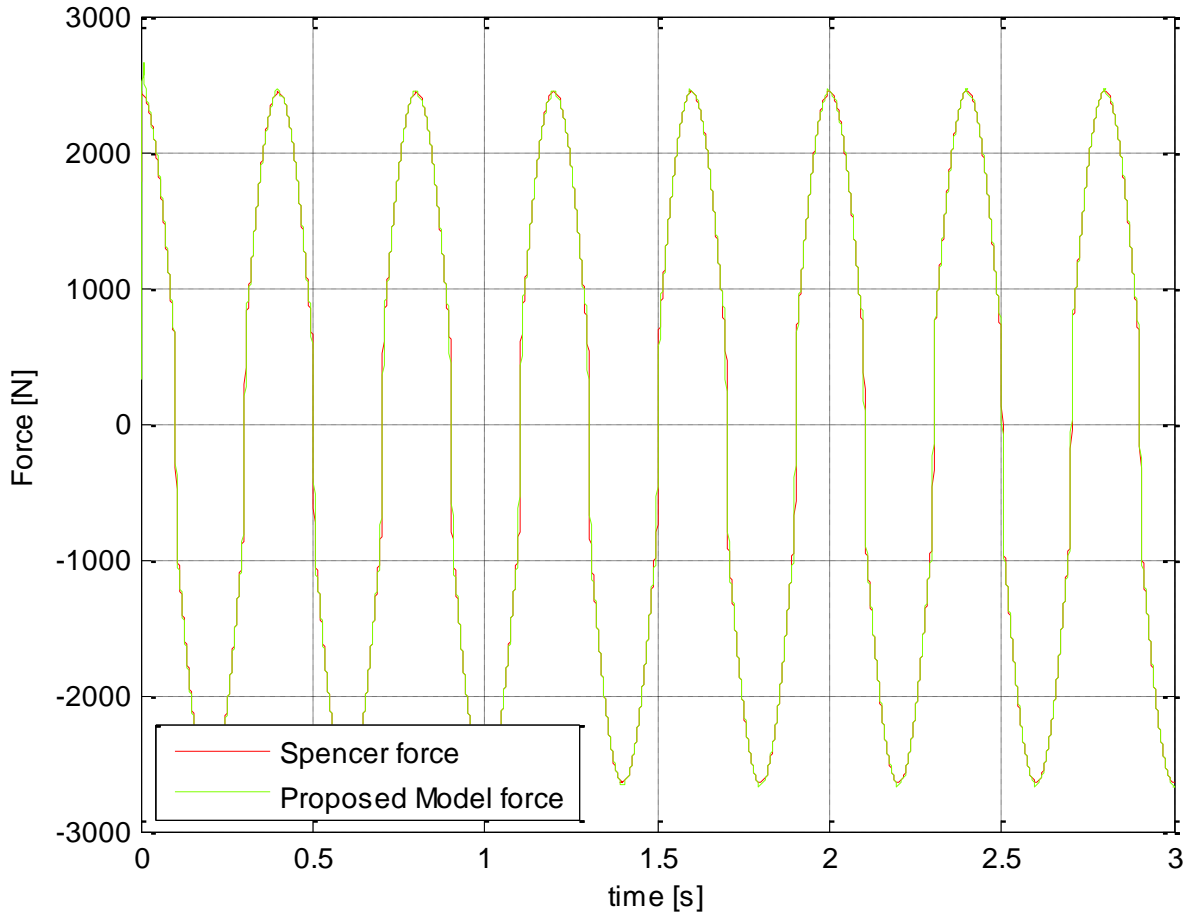


Figure 9.9. Force vs. Time for Spencer and Proposed Model

On initial inspection the two signals match up very well. There is little deviation between the two forces; they line up on top of each other. Figure 9.10 and Figure 9.11 take a closer look at the accuracy of the forward model in approximating the damper force from the Spencer model.

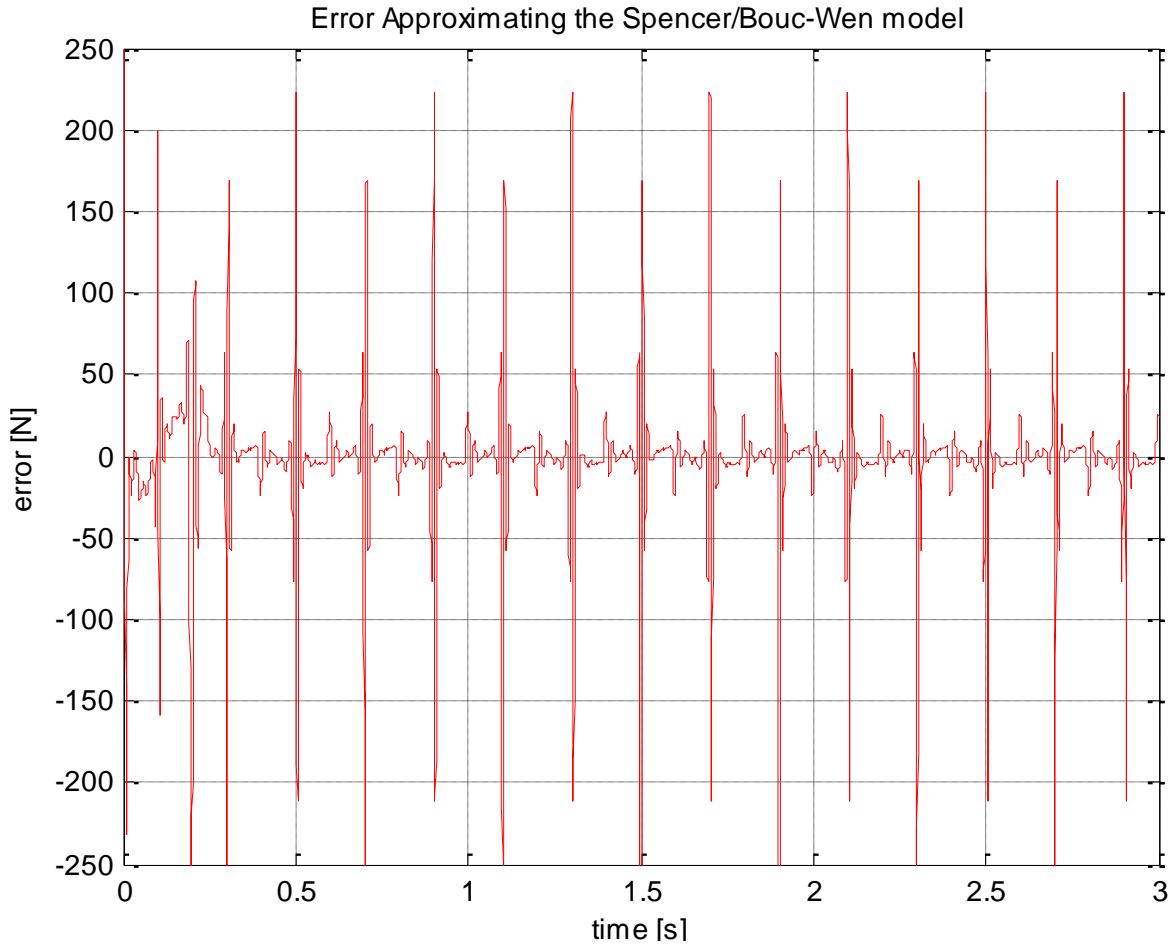


Figure 9.10. Error vs. time between Spencer force and model force

Upon initial inspection the error in Figure 9.10 seems to be very good for most of the time signal with some spikes occurring periodically. Viewing this error as a percentage of total force in Figure 9.11 shows that these spikes correspond to an error that is relatively low. These spikes peak within the two ranges of 6.2 and 8.2 for the positive values and -8 and -10 for the negative values. Conversely, the error values between spikes are exceptionally low, ranging between -1 to 1 percent.

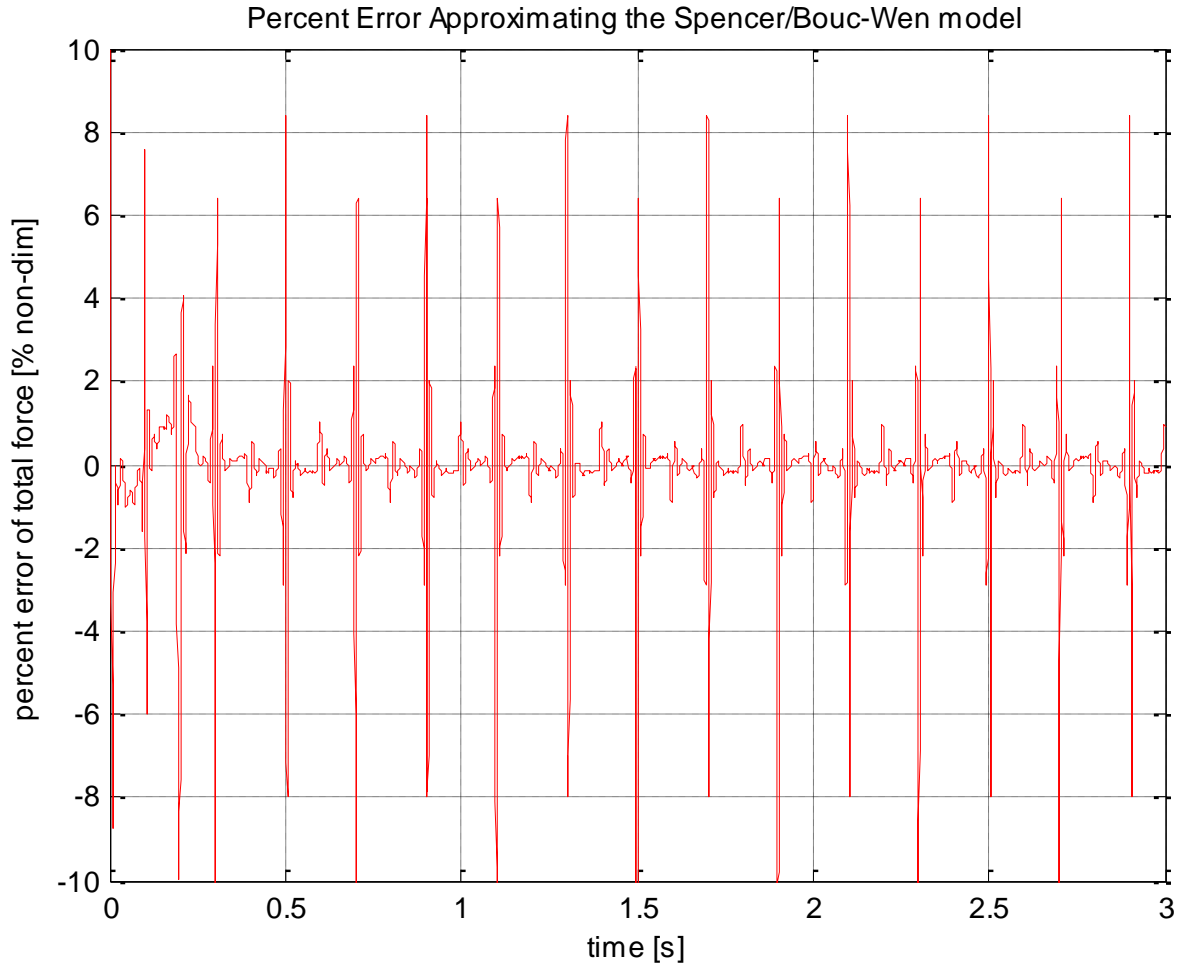


Figure 9.11. Error between the Spencer and proposed model as a percentage of total force

The reason behind the error spikes can be seen from a force versus velocity graph. Figure 9.12 shows that the Spencer model creates a force that has a greater change in the slope when approaching the region between high speed and low speed damping. When the force versus velocity curve is approaching the bi-linear transition region around ± 5 cm/s, there is an abrupt transition in the slope of the line. The behavior during this transition region is different for the Spencer model versus the proposed model. The Spencer is more abrupt and squared off, while the proposed model generates a more gradual transition. This behavioral difference in the transition region points to the fact that as the damper force approaches zero velocity, there is a growing error between the hysteretic Spencer force and the proposed model force. However, this is not concerning, because many dampers do exhibit a more rounded of behavior characteristic of the proposed model and similar to the previously used MagneRide damper. Also, the simulated Spencer damper is still just a model.

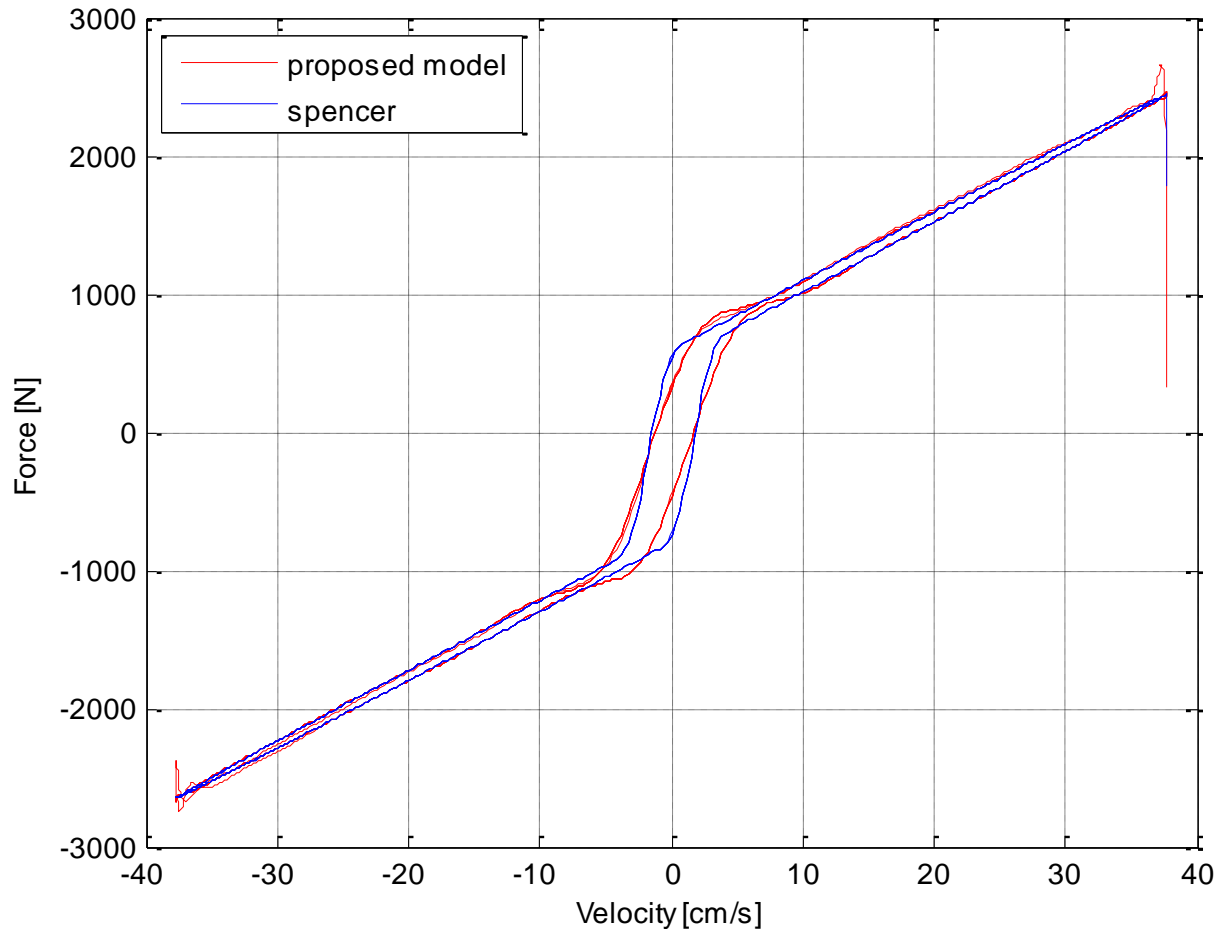


Figure 9.12. Force vs. Velocity characterization of damper in Spencer model: Spencer vs. proposed model force

Figure 9.13 is provided just to show that the FIR filter in our proposed model did in fact converge, and Figure 9.14 illustrates the frequency response of that FIR filter as well as its IIR approximation.

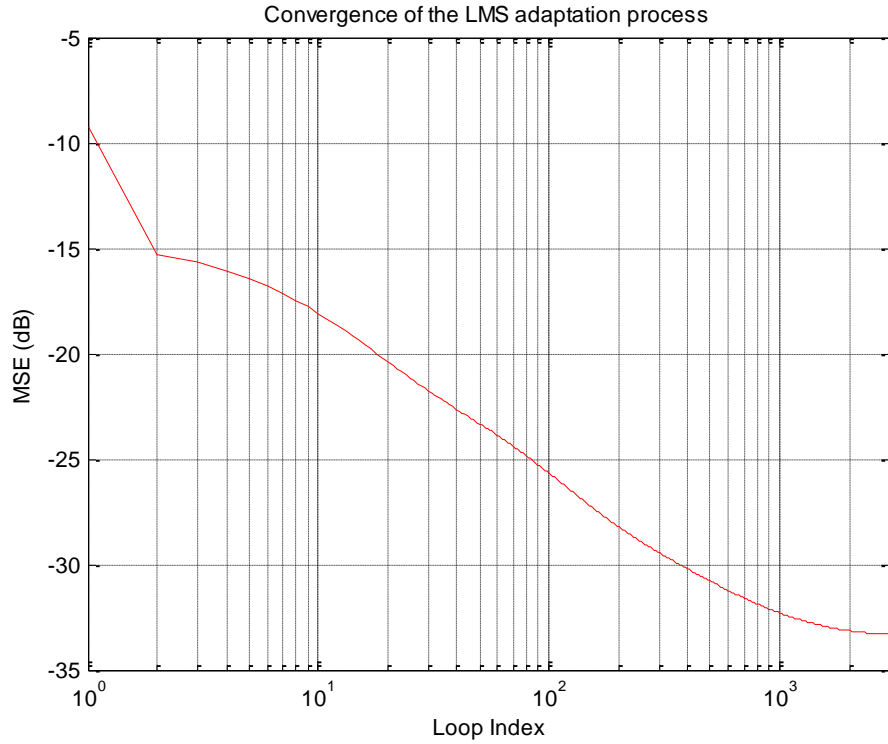


Figure 9.13. MSE and Convergence of FIR filter in Proposed model for Spencer validation

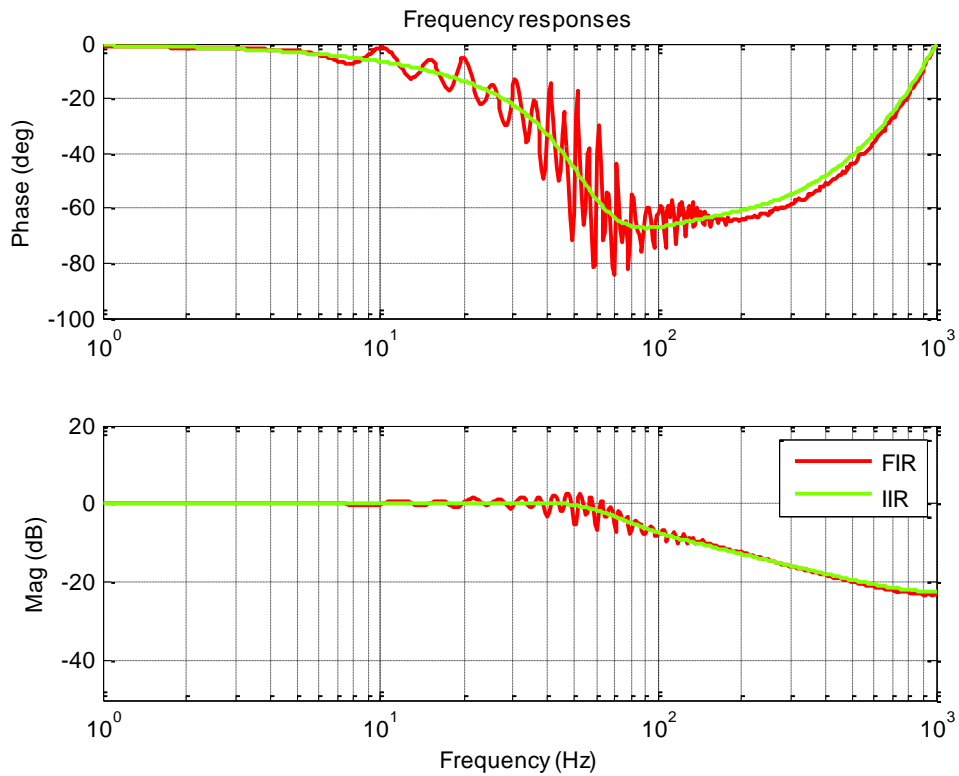


Figure 9.14. FIR and IIR filter approximation for Spencer validation

Our proposed model has the ability to accurately capture the behavior of an MR Damper described by the Spencer model. The advantage of our proposed model over the traditional Spencer model is that it can be inverted for real-time application. This ability coupled with its high fidelity performance strongly validates its design.

10) Conclusion

A high fidelity invertible temperature dependent MR Damper model for use in a real-time controller was developed and validated against experimental results as well an industry standard Spencer Model. The proposed model's development originated from Reader's model [3] and improved upon it by capturing the temperature dependence for a MR Damper. Its ability to successfully characterize a MR Damper with respect to current, temperature, and relative velocity allows it to improve upon the overall prediction error.

Unique to this research was the identification of an empirically based thermal function $h(i, T)$ that helped reduce the predicted force error. It explicitly isolated and compensated for the effects of temperature on the non-hysteric force production capabilities of a MR Damper. Additionally, the function was structured as a simple look up table of non-dimensional scaling factors, lending itself favorable for real-time implementation.

Analysis of the MR Damper dynamics extended the results of Reader's work [3] by establishing a new process for developing a low order inverse hysteresis filter. An adaptive process was used to tune a series of unconditionally stable FIR filters to characterize damper dynamics at different operating conditions. The characterizations of these dynamics were shown to be current and temperature independent, and so an averaged version was calculated. From this average, an easily invertible low order IIR filter was "fit" to the high-order FIR frequency response. This IIR filter accurately matched the global trends of the damper dynamics, but sacrificed the local ripples in the magnitude plot in order to achieve a lower order transfer function. Fortunately, this did not jeopardize the performance of the proposed model resulting in only a minimal increase in error. Additionally, this third order IIR filter resulted in lower computing costs and easier tuning capabilities. The inverse Hysteresis filter $H(z)_{IIR}^{-1} Universal$ was created by swapping two select poles and zeros to create a baseline transfer function. This was then manually tuned to not only fully capture the inverse dynamics of the damper, but have a frequency response that creates a low pass filter when combined with the non-inverted hysteretic filter.

The full inverse MR Damper model was successfully constructed and verified with experimental data from an MR Damper that spanned a wide range of temperatures and currents. The model produced a consistently low error of about 3.5% for one, two and three amps. For the zero amp operating condition, an interesting behavior emerged. The experimental data showed that the empirically based model began to break down as it approached the zero current. This indicates

the need for future research to investigate and understand how the proposed model should transition from 1 amp down to 0 amps.

The final verification of the proposed model involved the characterization and estimation of a Spencer based simulation damper. The forward model accomplished this very well and produced a low force error except when approaching zero velocity. This was neither good nor bad; rather, it illuminated a fundamental difference between the structure of the proposed forward model and the Spencer model when estimating the transition from high speed to low speed damping. The major advantage of the proposed model over the Spencer model is that it can be easily inverted.

The proposed model fully satisfied all of the design criteria set forth at the beginning of the document. It is capable of successfully generating an improved real-time command signal to be used in conjunction with any MR Damper control strategy to enhance system performance, reduce prediction error, and keep system costs to a minimum.

References

1. Reader, D., S.C. Southward, and M. Ahmadian. *Nonlinear MR model inversion for semi-active control enhancement*. in *Active and Passive Smart Structures and Integrated Systems 2009, March 9, 2009 - March 12, 2009*. 2009. San Diego, CA, United states: SPIE.
2. Wei, Z., C. Chee-Meng, and H. Geok-Soon. *Inverse dynamics control for series damper actuator based on MR fluid damper*. in *2005 IEEE/ASME International Conference on Advanced Intelligent Mechatronics, 24-28 July 2005*. 2005. Piscataway, NJ, USA: IEEE.
3. Reader, D.M., *Nonlinear MR Model Inversion for Semi-Active Control Enhancement with Open-Loop force Compensation*, in *Mechanical Engineering*. 2009, Virginia Polytechnic Institute and State University: Blacksburg. p. 75.
4. Duym, S. and K. Reybrouck, *Physical characterization of nonlinear shock absorber dynamics*. European Journal of Mechanical and Environmental Engineering, 1998. **43**(Compendex): p. 181-188.
5. Breese, D.G., F. Gordaninejad, and E.O. Ericksen, *Heat generation of magneto-rheological fluid dampers*. Proceedings of SPIE - The International Society for Optical Engineering, 2000. **3988**(Compendex): p. 450-456.
6. Wen, Y.K., *Method of Random Vibration of Hysteretic Systems*. Journal of Engineering Mechanics Division, ASCE, 1976. **102**(EM2): p. 249-263.
7. B. F. Spencer, J., S. J. Dyke, M.K. Sain and J. D. Carlson, *Phenomenological Model of a Magnetorheological Damper*. Journal of Engineering Mechanics, ASCE, 1997. **123**(3): p. 230-238.
8. Lion, A. and S. Loose, *A thermomechanically coupled model for automotive shock absorbers: Theory, experiments and vehicle simulations on test tracks*. Vehicle System Dynamics, 2002. **37**(Compendex): p. 241-261.
9. Alonso, M. and A. Comas, *Thermal model of a twin-tube cavitating shock absorber*. Proceedings of the Institution of Mechanical Engineers, Part D (Journal of Automobile Engineering), 2008. **222**(Copyright 2009, The Institution of Engineering and Technology): p. 1955-64.
10. Breese, D.G. and F. Gordaninejad, *Heating of magneto-rheological fluid dampers: A theoretical study*. Proceedings of SPIE - The International Society for Optical Engineering, 1999. **3671**(Compendex): p. 2-10.
11. Gordaninejad, F. and D.G. Breese, *Heating of magnetorheological fluid dampers*. Journal of Intelligent Material Systems and Structures, 1999. **10**(Copyright 2000, IEE): p. 634-45.
12. Snyder, R.A., G.M. Kamath, and N.M. Wereley. *Characterization and analysis of magnetorheological damper behavior due to sinusoidal loading*. in *Smart Structures and Materials 2000: Damping and Isolation, March 6, 2000 - March 8, 2000*. 2000. Newport Beach, CA, USA: Society of Photo-Optical Instrumentation Engineers.
13. Wilson, N.L., et al. *Performance robustness of a magnetorheological seat suspension to temperature variations using skyhook control*. in *Active and Passive Smart Structures and Integrated Systems 2009, 9 March 2009*. 2009. USA: SPIE - The International Society for Optical Engineering.

14. Batterbee, D. and N.D. Sims, *Temperature sensitive controller performance of MR dampers*. Journal of Intelligent Material Systems and Structures, 2009. **20**(Copyright 2009, The Institution of Engineering and Technology): p. 297-309.
15. Batterbee, D.C. and N.D. Sims. *Temperature sensitive stability of feedback controllers for MR dampers*. in *Active and Passive Smart Structures and Integrated Systems 2008, 10-13 March 2008*. 2008. USA: SPIE - The International Society for Optical Engineering.
16. Dixit, R.K. and G.D. Buckner, *Sliding mode observation and control for semiactive vehicle suspensions*. Vehicle System Dynamics, 2005. **43**(Copyright 2006, IEE): p. 83-105.
17. Biglarbegian, M., W. Melek, and F. Golnaraghi. *Intelligent control of vehicle semi-active suspension systems for improved ride comfort and road handling*. in *NAFIPS 2006 - 2006 Annual Meeting of the North American Fuzzy Information Processing Society, June 3, 2006 - June 6, 2006*. 2006. Montreal, QC, Canada: Institute of Electrical and Electronics Engineers Inc.
18. Bajkowski, J., et al., *A model for a magnetorheological damper*. Mathematical and Computer Modelling, 2008. **48**(Copyright 2008, The Institution of Engineering and Technology): p. 56-68.
19. Kordonsky, W.I., S.P. Gorodkin, and S.A. Demchuk, *Magnetorheological control of heat transfer*. International Journal of Heat and Mass Transfer, 1993. **36**(Copyright 1993, IEE): p. 2783-8.
20. Gang, J., M.K. Sain, and B.E. Spencer, Jr., *Nonlinear blackbox modeling of MR-dampers for civil structural control*. IEEE Transactions on Control Systems Technology, 2005. **13**(Copyright 2005, IEE): p. 345-55.
21. Mauricio Zapateiro, N.L. *Neural Network Modeling of a Magnetorheological Damper*. in *Frontiers in Artificial Intelligence and Applications*. 2007. Amsterdam, The Netherlands: IOS Press.
22. Zapateiro, M. and L. Ningsu, *Parametric and non parametric characterization of a shear mode magnetorheological damper*. Journal of Vibroengineering, 2007. **9**(Copyright 2008, The Institution of Engineering and Technology): p. 14-18.
23. Chih-Chen, C. and P. Roschke, *Neural network modeling of a magnetorheological damper*. Journal of Intelligent Material Systems and Structures, 1998. **9**(Copyright 1999, IEE): p. 755-64.
24. Boada, M.J.L., et al. *A new non-parametric model based on neural network for a MR damper*. in *2008 9th Biennial Conference on Engineering Systems Design and Analysis, July 7, 2008 - July 9, 2008*. 2009. Haifa, Israel: ASME.
25. Pin-Qi, X., *An inverse model of MR damper using optimal neural network and system identification*. Journal of Sound and Vibration, 2003. **266**(Copyright 2004, IEE): p. 1009-23.
26. Hudha, K., et al., *Non-parametric linearised data driven modelling and force tracking control of a magnetorheological damper*. International Journal of Vehicle Design, 2008. **46**(Copyright 2008, The Institution of Engineering and Technology): p. 250-69.
27. Li, R., et al. *Fuzzy intelligent control of automotive vibration via magneto-rheological damper*. in *2004 IEEE Conference on Cybernetics and Intelligent Systems, December 1, 2004 - December 3, 2004*. 2004. Singapore: Institute of Electrical and Electronics Engineers Inc.

28. Song, X., et al., *Parametric study of nonlinear adaptive control algorithm with magneto-rheological suspension systems*. Communications in Nonlinear Science and Numerical Simulation, 2007. **12**(4): p. 584-607.
29. Xubin, S., M. Ahmadian, and S.C. Southward, *Modeling magnetorheological dampers with application of nonparametric approach*. Journal of Intelligent Material Systems and Structures, 2005. **16**(Copyright 2005, IEE): p. 421-32.
30. Venhovens, P.J.T., *Development and implementation of adaptive semi-active suspension control*. Vehicle System Dynamics, 1994. **23**(Compendex): p. 211-235.
31. Karnopp, D., M.J. Crosby, and R.A. Harwood, *VIBRATION CONTROL USING SEMI-ACTIVE FORCE GENERATORS*. American Society of Mechanical Engineers (Paper), 1973(Compendex).
32. Ahmadian, M., S. Xubin, and S.C. Southward, *No-jerk skyhook control methods for semiactive suspensions*. Transactions of the ASME. Journal of Vibration and Acoustics, 2004. **126**(Copyright 2005, IEE): p. 580-4.
33. Liu, Y., et al. *Temperature dependent skyhook control of HMMWV suspension using a failsafe magneto-rheological damper*. in *Smart Structures and Materials 2003: Industrial and Commercial Applications of Smart Structures Technologies, March 4, 2003 - March 6, 2003*. 2003. San Diego, CA, United states: SPIE.
34. Jalili, N., *A comparative study and analysis of semi-active vibration-control systems*. Journal of Vibration and Acoustics, Transactions of the ASME, 2002. **124**(Compendex): p. 593-605.
35. Ramallo, J.C., H. Yoshioka, and B.F. Spencer Jr, *A two-step identification technique for semiactive control systems*. Structural Control and Health Monitoring, 2004. **11**(Compendex): p. 273-289.
36. Pan, S., et al., *Yield stress and temperature effect of magneto-rheological fluid*. Gongneng Cailiao/Journal of Functional Materials, 1997. **28**(Compendex): p. 264-267.
37. Richard O. Duda, P.E.H., David G. Stork, *Pattern Classification*. Second Edition ed. 2001, New York: John Wiley & Sons, Inc.
38. Bernard Widrow, S.D.S., *Adaptive Signal Processing*. Prentice-Hall Signal Processing Series, ed. A.V. Oppenheim. 1985, Englewood Cliffs, NJ: Prentice-Hall Inc.
39. Gene F. Franklin, J.D.P., Abbas Emami-Naeini, *Feedback Control of Dynamic Systems*. 2006, Upper Saddle River, NJ: Pearson Prentice Hall.
40. Jaggi, S. and A.B. Martinez, *Upper and lower bounds of the misadjustment in the LMS algorithm*. IEEE Transactions on Acoustics, Speech and Signal Processing, 1990. **38**(Copyright 1990, IEE): p. 164-6.
41. Emmons, S.G., *Characterizing a Racing Damper's Frequency Behavior with an Emphasis on High Frequency Inputs*, in *Mechanical Engineering*. 2005, Virginia Polytechnic Institute and State University.